DOTTORATO DI RICERCA IN

PHYSICS AND NANO SCIENCES

XXVI CICLO
Sede Amministrativa Università degli Studi di MODENA e REGGIO EMILIA

TESI PER IL CONSEGUIMENTO DEL TITOLO DI
DOTTORE DI RICERCA

A theoretical study of magnetic molecules and their interaction with magnetic substrates

---

Candidato:
SIMONE MAROCCHI

Supervisors:

Prof. Franca Manghi

Dr. Valerio Bellini

Contents

Chapter 1.

Introduction

Handling nanoscale objects and controlling their interaction with the surrounding world is one of the present challenges of fundamental research in nanoscience. Spin dependent effects and interactions play a very significant role in this field, the ability to control electron spin degrees of freedom at the nanoscale is crucial both from fundamental and technological points of view. Single molecule magnets are particularly promising in this context. Single molecule magnets are collections of mono-disperse small magnetic (or paramagnetic) particles that can be synthesized in high yield, with magnetic properties that upon proper functionalization can be tuned at a certain degree. Synthetic chemistry is now able to build almost at will supramolecular-organized systems, in the form of dimers, trimers etc.., as demonstrated by the work on low-spin Cr-based antiferromagnetic molecular rings [1, 2]. Deposition and eventually (self-)assembly of molecular spins on surfaces is another research line where both chemists and physicists have converged their efforts. The motivation is two-fold, (i) to address/tune the magnetic properties of the individual molecules, and (ii) to exploit the powerful capabilities of sophisticated experimental techniques such as Scanning Tunneling Spectroscopy [3, 4] and Microscopy and X-ray Magnetic Circular Dichroism [5–7], which require very clean samples and ultra-high-vacuum conditions. The main concerns are whether the molecules survive the evaporation procedure, and how their properties are modified by the interaction with the substrate. The experience maturated in the last years tells that if some molecules are not chemically stable, others, such as metal Phthalocyanines [7] and Porphyrines [8, 9], double-decker compounds [10], polymetallic cluster as Fe_4 [11], Mn_6 [12, 13] and Cr_7Ni [14] are robust enough to survive the evaporation/deposition. If a too large interaction with a surface is often detrimental, in some cases some sort of interaction, e.g. magnetic coupling, is sought to block the spins of paramagnetic molecules,

and to lead to magnetic ordering within a thin layer of deposited molecules. To give a comprehensive analysis of the scientific issues discussed above, theoretical characterization by means of atomistic first-principles techniques have been often supplied in conjunction with key experiments. The scope of this thesis is to test the capability of density-functional based methods to reproduce the properties of magnetic molecules in the gas phase, and to investigate the mechanisms through which magnetic coupling with magnetic substrates can be achieved. Regarding the first issue, we extended the work on antiferromagnetic rings, a class of magnetic molecules which has been studied extensively in the last year in Modena both from the theoretical [15, 16] and experimental [17, 18] point of view. The main goal was to give a DFT characterization of different molecular derivatives belonging to this family, i.e. single AFM rings, supramolecular ring dimers, trying to improve the results obtained previously, and obtaining novel results for a special class of supramolecular dimers, which has never been addressed before. In the other research line, the study of the magnetic coupling between a paramagnetic molecule (cobaltocene [19]) and a magnetic substrate is addressed: the substrate is composed by a graphene layer deposited on a ferromagnetic metal [20, 21], and the focus was on the role of graphene in mediating the spin communication between the two magnetic objects. Due to the different periodicity of the two classes of system under investigation, we had to employ different DFT methodologies, as discussed extensively in the next chapters. We give in the following a short survey, summarizing the main points that are discussed therein.

In the **second chapter** the basic concepts of the Density Functional Theory (DFT) are resumed. After a brief presentation of the many-electron problem, we introduce the Kohn-Sham (KS) equations which are used to solve it in a computationally efficient way. We also discuss the main approaches used in practical calculations to approximate the exchange and correlation potential, namely the local density approximation (LDA), the generalized-gradient approximation (GGA), the concept of hybrid functional together with its most common implementation, i.e. B3LYP.

In the **third chapter** the numerical codes used for our simulations, namely the Vienna Ab initio Simulation Package (VASP) [22] and the computational chemistry software NWChem [23] are presented. We introduce the different features of the two softwares, in particular the choice of the basis set needed to solve algebraically the KS equations, (i) as a sum of atomic centered functions localized in real space for NWChem and (ii) as a plane-waves expansion for VASP, and comment on the advantages and disadvantages in

the use of one ore the other code, in relation to the nature of the system investigated. The NWChem code has been used for the simulation of isolated AFM rings and dimers. We discuss the choice of the exchange and correlation functional, and give a detailed explanation of the constrained-DFT method [24, 25] used to achieve the desired magnetic configurations in the molecules. We then present the VASP code, introducing the concept of pseudopotential, and devoting some space on the description of the Projector Augmented Wave method (PAW) method [26]; this is our method of choice to obtain the results for the cobaltocene on graphene/ferromagnetic metal system. The effects of some important corrections on the calculated total energy of the systems like the inclusion of van der Waals dispersion interactions [27] and of on-site Coulomb interactions [28] are also discussed. At the end of the chapter a summary of the essential parameters that must be converged in the plane-waves calculations (e. g. energy cut-off and k-point grid) is presented accompanied by several tests. This tests lasted some months, and are an important achievement of the thesis, since no experience on the use of the VASP code existed in my research group.

The **fourth chapter** is devoted to the study of the magnetic coupling in the magnetic molecules belonging to the class of the antiferromagnetic rings, in particular *green*-Cr_7M rings (with M= Ni^{2+}, Mn^{2+}, Fe^{2+} and Cu^{2+}), the *purple*-Cr_7Ni ring and *purple*-Cr_7M/pyr/*green*-Cr_7M, supramolecular dimers (M, M' are divalent ions chosen among Ni^{2+}, Mn^{2+} and Zn^{2+}). After a general introduction on magnetic molecules we discuss the spin Hamiltonian used to describe their magnetic properties and the methodology employed to extract the exchange parameters in DFT calculations. The rest of the chapter is divided in two parts. In the first section the structures of the more representative molecules belonging to this class are discussed together with the main results obtained so far by DFT approaches. In the second part we present the results of our theoretical investigation. Until now the theoretical studies on this class of molecules had been performed after a "pruning" procedure of the atomic structures in order to save computational resources. The exchange parameters obtained using the pristine structure of *green*-Cr_7M rings are compared with the theoretical investigations of Bellini et al. [15] as well as inelastic neutron scattering [29] and other experimental measurements [30, 31]. We also present the same analysis of the pristine structure of *purple*-Cr_7Ni ring with a comparison of other theoretical calculation [15] and experimental findings obtained by means of temperature-dependent susceptibility analysis [18]. In the last section a comprehensive analysis of the magnetic couplings in *purple*-Cr_7M/pyr/*green*-Cr_7M, supramolecular dimers is given. Several combinations of the divalent ions M, M' on the two rings have been considered. Depending on

the choice of M and M', the magnetic coupling between two molecular spins could be tuned, and a comparison of the trend individuated by our calculations and the ones obtained by (unpublished) specific heat measurements is presented.

In the **fifth chapter** an investigation of the magnetic properties of cobaltocene ($CoCp_2$) adsorbed on a graphene layer deposited on several magnetic substrates is presented. A short summary on the main results obtained so far by experimental and theoretical approach in the characterization of the two components of the system, i. e. the $CoCp_2$ and graphene/metals, is given. The molecular and electronic structure of $CoCp_2$ predicted using the B3LYP functional given in Ref. [19] is presented and compared with our calculations. The two possible stackings of graphene/Ni(111) which have been identified as the most favored geometries by a combined high-resolution X-ray photoelectron spectroscopy (HR-XPS) and DFT calculations [20] are revisited, together with the one observed in graphene/Fe/Ni(111), by means of a combined DFT and electron-spectroscopic analysis [21]. After a brief discussion on some test calculations on the graphene/M/Ni(111) (M=Ni, Fe and Co) substrates, we compare our results for the different stackings with the ones obtained by previous literature. We also supply a systematic study of the possible adsorption sites of the $CoCp_2$ molecule on the graphene/Ni(111) is presented. After having discussed extensively how the structural factors, namely the structural conformation of the isolated molecules, the type of stacking that graphene attains on the metal substrates and the possible adsorption sites of the $CoCp_2$ molecule, can affect the magnetic coupling, we rationalize the mechanism behind the magnetic coupling. This is done discussing the spin-polarized LDOS, the charge-transfer at the molecule-substrate interface, and the cross sectional plots of the magnetization density. These calculations represent one of the first attempt to figure out, by DFT calculation, the role of graphene in mediating the magnetic coupling between a magnetic molecule and ferromagnetic substrate.

In the **sixth chapter** a short summary of the results of this thesis is given, and the conclusion are drawn.

Chapter 2.

Density Functional Theory

In the present thesis we have studied magnetic properties of molecules in vacuum and adsorbed on magnetic surface with an atomistic density-functional theory (DFT) approach. These properties are directly related to the description of the electronic states obtained as solutions of the so-called many-body problem. In this chapter we will briefly introduce the milestones of the DFT theory, the Hohenberg-Kohn theorems and the basic ideas to solve the electronic problem in the Kohn-Sham scheme. This method provides a practical and computationally efficient scheme of solving the Schrödinger equation of N-interacting electrons for the study of electronic states and (in its spin-polarized formulation) the magnetic properties of solids, atoms and molecules.

2.1. The Many Interacting Electrons system

The knowledge of the electronic states of the system represents the key to correctly describe the physics behind the magnetic phenomena in solids and determine the electronic quantities of interest (e.g. the spin value, the exchange coupling the spins, etc...). In the quantum-mechanics frame the evolution of electronic states is governed by the time-dependent Schrödinger equation that, for non-relativistic systems, can be written as:

$$i\hbar\frac{\partial}{\partial t}|\Psi>=\hat{H}|\Psi\rangle. \tag{2.1}$$

In solids and in a great variety of materials (in absence of any external field) $\hat{H}$ is given by the kinetic term and the Coulomb interaction of the electrons and nuclei provided that all

the other interaction can be neglected:

$$\hat{H} = \sum_i -\frac{\hbar^2\nabla_i^2}{2m_e} + \sum_I -\frac{\hbar^2\nabla_I^2}{2M_I} + \frac{1}{2}\sum_{i\neq j}\frac{e^2}{|\mathbf{r}_i - \mathbf{r}_j|} - \sum_{iI}\frac{Z_I e^2}{|\mathbf{r}_i - \mathbf{R}_I|} + \frac{1}{2}\sum_{I\neq J}\frac{Z_I Z_J e^2}{|\mathbf{R}_I - \mathbf{R}_J|} \quad (2.2)$$

where the indexes (i,j) run over electrons and (I,J) run over nuclei. For the majority of the applications it is possible to reduce the complexity of this equation decoupling the electronic and nuclei motion: this is called the *Born-Oppenheimer* (BO) approximation or adiabatic approximation.

2.1.1. Born-Oppenheimer approximation

The Born-Oppenheimer approximation [32] is based on the observation that the nuclei have masses 3 or more orders of magnitude larger than the electrons ($M_N \gg m_e$). This implies that their motion is slow compared to the faster electron dynamics and takes place on a different time-scale. Therefore, while solving the electronic problem, nuclear position $\mathbf{R_I}$ can be considered fixed and can be described as constant parameters. In this way the electronic problem is decoupled from the nuclear one reducing the degrees of freedom to the electronic variables only: a system of identical, indistinguishable particles. The new electronic Hamiltonian in the BO approximation is given by:

$$\hat{H}_{BO} = \sum_i -\frac{\hbar^2\nabla_i^2}{2m_e} + \frac{1}{2}\sum_{i\neq j}\frac{e^2}{|\mathbf{r}_i - \mathbf{r}_j|} - \sum_{iI}\frac{Z_I e^2}{|\mathbf{r}_i - \mathbf{R}_I|}. \quad (2.3)$$

The first and second term are universal and independent of the system (they are respectively the kinetic energy and Coulomb interaction between the electrons), while the last one is characteristic of the studied system and contains the interaction between the electrons and the nuclei. Nevertheless, at this step the Schrödinger equation is still too complex to be solved. From now onwards we will refer to Eq. (2.3) as the Hamiltonian describing the many-body problem of Eq. (2.1), avoiding the specification of the BO label ($\hat{H} \equiv \hat{H}_{BO}$).

2.1.2. Approaches to the Problem

A diagonalization of the Schrödinger Eq. (2.1) would lead to a solution of the problem obtaining the energy eigenvalues and the wave functions $|\Psi\rangle$ of the system. Nevertheless,

in the previous equations the wave function is contemporary functions of $3N$ variables $|\Psi(\mathbf{r}_1, ..., \mathbf{r}_N)\rangle$ that are all interconnected due to the electron-electron interaction term of Eq. (2.3). As a consequence the Schrödinger equation growths exponentially in complexity increasing N and the problem, that is not exactly solvable already for $N > 2$, cannot be handled even numerically when one deals with materials constituted of several tens or hundreds of atoms and other paths should be explored to solve the Schrödinger equation of the system.

Several approaches exists that try to find an approximate solution of the full many-body problem: the configuration interaction and the quantum Monte-Carlo approach for example aim to describe the full many-body wave function. Nevertheless such solutions would contain informations about every single electron of the system, and such a level of detail would be hard to manage and interpret. Instead, usually one looks for the expectation values or macroscopic quantities that do not involve directly the knowledge of the exact solution of Eq. (2.1). With this consideration one can think to simplify the problem and its Hamiltonian, reducing the number of variables of the system to the ones of interest. This is in analogy with the thermodynamic case where one describes the whole system in terms of macroscopic averages, regardless of the real microscopic configuration. Between the variety of approaches that have been proposed in literature, Density Functional Theory and its time-dependent (TD) version, i.e. TDDFT, represent the prominent examples of this many-body problem simplification for treating respectively equilibrium ground-state observables or their dynamical evolution. Other possible approaches are the Many-Body Perturbation Theory and the dynamical mean-field theory, but we will discuss no further these latter methods.

2.2. The Density Functional Theory Approach

Density Functional Theory allows to overcome the above mentioned difficulties with the advantage of being formally exact and numerically efficient for the study of the geometry and ground-state electronic properties of a great variety of materials. Thanks to this, accurate results are obtained for systems of different nature going from molecules and nanostructures, to proteins or biological matter up to solids, surfaces or interfaces.

The strength of this approach stands behind the idea of describing the entire system through the electronic density distribution, a much simpler variable with only 3 degrees of freedom with respect to the full many-body wave function. This key quantity is independent of the size of the system and therefore allows to treat structures with hundreds of atoms without increasing the amount of data to be stored in simulations as it happens in other methods based on the full many-body wave function. A possible solution of the DFT problem is then represented by the Kohn-Sham scheme. This clever approach exploits the possibility of mapping the many-body system into an easier independent-particles problem with a one-to-one correspondence that gives the same expectation value for the observables of the real ground-state system. Hence each property that depends on the ground-state configuration can be obtained solving this new simplified problem.

In this section I briefly introduce DFT and the Kohn-Sham scheme that underlies all our ground-state calculations.

2.2.1. Hohenberg-Kohn Theorems

Target of DFT is the solution of a system of N electrons in its ground-state configuration, which experiment the presence of an external, one-particle local potential v_{ext} not evolving in time. In the Born-Oppenheimer approximation this external potential is represented by the interaction with the nuclei of Eq. (2.3) that are fixed. For this stationary system Eq. (2.1) reduces to the corresponding time-independent Schrödinger equation:

$$\hat{H}|\Psi\rangle = \epsilon|\Psi\rangle \tag{2.4}$$

where $|\Psi\rangle$ represents a many-body wave function and ϵ the corresponding eigenvalue. The ground-state of the system is then identified by the particular state $|0\rangle$ of energy ϵ_0. The Hamiltonian of the N-electron system can be expressed as:

$$\hat{H} = \hat{T} + \hat{U} + \hat{V}_{ext} \quad \text{where} \quad V_{ext} = \int d\mathbf{r}\ v_{ext}(\mathbf{r}) n(\mathbf{r}) \tag{2.5}$$

with T and U respectively the kinetic and the electron-electron interaction energies and V_{ext} the interaction energy with the external potential:

$$\begin{aligned} \hat{T} &= \sum_i -\frac{\hbar^2 \nabla_i^2}{2m_e} \qquad \hat{U} = \frac{1}{2}\sum_{i\neq j} \frac{e^2}{|\mathbf{r}_i - \mathbf{r}_j|} \\ \hat{V}_{ext} &= -\sum_{iI} \frac{Z_I e^2}{|\mathbf{r}_i - \mathbf{R}_I|} = \int d\mathbf{r}\ v_{ext}(\mathbf{r}) n(\mathbf{r}) \end{aligned} \tag{2.6}$$

As T and U have the same expression for all physical system, V_{ext} determines uniquely the particular system of interest. Said in other words, the Hamiltonian operator $\hat{H}$ is determined completely by the external potential V_{ext} acting on the N-electron system, and so are the wave functions, energies and all the other properties that descend from its knowledge, i.e. the electron density of the system in a state $|\Psi>$:

$$n(\mathbf{r}) = N\langle \Psi(\mathbf{r}_1, ..., \mathbf{r}_N) | \delta(\mathbf{r} - \mathbf{r_1}) | \Psi(\mathbf{r}_1, ..., \mathbf{r}_N) \rangle \tag{2.7}$$

and in particular the density $n_0(\mathbf{r})$ of the ground-state when $|\Psi\rangle = |0\rangle$. The first Hohenberg and Kohn theorem states that also the inverse assumption is valid:

Theorem 2.1 *(Hohenberg and Kohn I, 1964, Ref [33]). The ground-state density $n(\mathbf{r})$ of a system of interacting electrons subject to an external potential $v_{ext}(\mathbf{r})$ uniquely determines this potential and hence the entire physical system.*

That implies that for non-degenerate systems the Hamiltonian $H_{v_0} = T[n] + U[n] + V_0[n]$ (corresponding to the system with $v_{ext} = v_0$), its expectation value (the electronic total energy) $E_{v_0}[n] = \langle 0, [n] | H_{v_0} | 0, [n] \rangle$, and any observable become unique functionals of the electron density n. This one-to-one relation holds also for the many-body wave function $|\Psi\rangle = |\Psi[n]\rangle$.

Consequently the solution of the Schrödinger equation (2.4) is now functional of n, a 3-variables quantity which is much easier to handle with respect to the complete wave function. The possibility of finding the ground-state density that corresponds to the external potential v_0 is guaranteed by virtue of the Rayleigh-Ritz principle through the second important theorem.

Theorem 2.2 *(Hohenberg and Kohn II, 1964, Ref [33]). The energy functional* $E_{v_0}[n]$ *is minimized by the ground-state density* n_0 *that corresponds to the external potential* v_0*:* $E_{v_0}[n] \geq E_{v_0}[n_0]$.

Such variational principle is equivalent to the one that holds for the ground-state wave function $|\Psi_0\rangle$. Solution of $\hat{H}|0\rangle = \epsilon|0\rangle$ is then transformed to a minimization problem of $E_{v_0}[n]$ with respect to the variation of $n(\mathbf{r})$[1], a trivial task if the energy functionals $T[n]$, $U[n]$, $V_0[n]$ were known. We should point out that the complexity of the problem is now moved into the possibility of inverting the relation between $\hat{H}$ and n (that is the determination of these functionals) or finding reasonable and suitable approximations for them. The most successful approach is the one presented by Kohn-Sham in 1965, that will be described in the following section. Originally, other approximations have been proposed e.g. by Thomas and Fermi in 1927 and can be found in literature [34–36]. The principle idea of the KS method was to look at the Thomas-fermi model as an approximation of an exact theory.

2.2.2. Kohn-Sham Equations

A possibility to determine the energy functional is to refer to the one of a known simple system adapting it to the real problem. This is basically the Kohn-Sham (KS) approach, that starts from the

Definition 2.3 *(Kohn-Sham system, 1965, Ref [37]). Any system of interacting particles in the external potential* v_0 *can be mapped to a system of fictitious, non-interacting Kohn-Sham particles in the effective, local potential* v_S *such that both have the same ground-state density* n_0*:* $H = T + U + V_0 \overset{n_0}{\longleftrightarrow} H_S = T_S + V_S$.

Where $V_S[n] = \int d\mathbf{r}\ v_S(\mathbf{r})n(\mathbf{r})$ is a local, single-particle potential. As a consequence the Hohenberg and Kohn theorems (Ths. 2.1 and 2.2) hold also for the KS system and show that it is possible to access the real ground-state density n_0 (and all the other quantities that derive from it through theorem 2.1), via the minimization of the KS energy functional $E^{KS}[n] = T_S[n] + V_S[n]$. $T_S[n]$ is the kinetic energy for a system of N independent particles while V_S corresponds to the energy of the effective potential v_S determined as the one that makes the KS ground-state density reproduce the real system ground-state density

[1] Under the constraint of the total electron number N being fixed, that is obtained via the Lagrange multipliers method, where the parameter can be identified with the chemical potential.

n_0. Given v_S the Schrödinger equation for H_S reduces into a system of single-particle non-interacting Schrödinger equations:[2]

$$\left[-\frac{\nabla_\lambda^2}{2} + \int d\mathbf{r}\ v_S(\mathbf{r})n(\mathbf{r})\right] |\psi_\lambda^{KS}\rangle = \epsilon_\lambda^{KS}|\psi_\lambda^{KS}\rangle, \tag{2.8}$$

where λ labels the state. The system can be easily solved through a diagonalization, determining the single-particle wave functions $|\psi_\lambda^{KS}\rangle$ and the energy eigenvalues ϵ_λ^{KS} of the KS problem i.e., the ground state solution of both the KS and the real systems:

$$n(\mathbf{r}) = \sum_{\lambda=1}^{N} |\psi_\lambda^{KS}|^2. \tag{2.9}$$

In this way the kinetic energy functional of a system of non-interacting particles is known and given by:

$$T_S[n] = \sum_{\lambda=1}^{N} \langle\psi_\lambda^{KS}| \left(-\frac{\nabla^2}{2}\right) |\psi_\lambda^{KS}\rangle \tag{2.10}$$

a much easier form with respect to the one of the real system. In order to obtain an expression for the effective potential $v_S[n]$ we can rewrite the energy functional of the interacting system $E_{v_0}[n]$ adding and subtracting $T_S[n]$ plus an Hartree energy term $V_H[n]$:[3]

$$E_{v_0}[n] = T_S[n] + V_H[n] + V_0[n] + V_{XC}[n], \tag{2.11}$$

where:

$$V_H[n] = \frac{1}{2}\iint d\mathbf{r}d\mathbf{r}'\ n(\mathbf{r})v_H(\mathbf{r},\mathbf{r}')n(\mathbf{r}), \tag{2.12}$$

$$V_{XC}[n] = T + U - V_H - T_S. \tag{2.13}$$

$v_H = \int d\mathbf{r}'\ \frac{n(\mathbf{r}')}{|\mathbf{r}-\mathbf{r}'|}$ is the functional derivative of V_H with respect to the density, while V_{XC} denotes the *exchange-correlation* energy that includes the part of the energy functional that is not explicitly known (named Stupidity energy by Feynmann [38]). Until $T_S + V_H$ is rather close to $T + U$ of the real system V_{XC} is small and can be approximated in a rough way obtaining a good description of the system. The energy functional of both systems,

[2] In the following I will adopt atomic units ($e = m_e = \hbar = 1$) to simplify the notation.
[3] $V_H[n]$ represents the classical electrostatic energy of interaction between the electrons.

the interacting and the auxiliary one, takes its minimum at the same density n_0. As a consequence of the second theorem of Hohenberg and Kohn (Th. 2.2) one can apply the variational principle to both functionals (under the constraint of n being V-representable[4]) obtaining the following relation:

$$v_S(\mathbf{r}, [n_0]) = v_0(\mathbf{r}) + v_H(\mathbf{r}, [n_0]) + v_{XC}(\mathbf{r}, [n_0]) \tag{2.14}$$

$$v_{XC}(\mathbf{r}, [n_0]) = \frac{\delta V_{XC}}{\delta n(\mathbf{r})}|_{n_0}. \tag{2.15}$$

It is possible to demonstrate that v_{XC} is the local exchange correlation energy per particle, that is the electrostatic interaction energy of a particle with its DFT exchange-correlation hole n_{XC}[5] and should fulfill the sum rule:

$$\int d\mathbf{r}' \; n_{XC}(\mathbf{r}, \mathbf{r}'; n) = -1. \tag{2.16}$$

Eqs. (2.8) and (2.14) represent the KS equations that satisfy definition 2.3. The single-particle potential v_S now depends on the density and this set of equation has to be solved in a self-consistent procedure. Starting from a guess density $\tilde{n}$ it is possible to determine v_H and v_{XC} (i.e., v_S), and to calculate the new wave functions and density solving the single-particle Schrödinger equations (2.8). This process can be iterated until the differences between the densities at different steps vanishes or/and the energy converges to its minimum value. This is guaranteed by the second theorem of Hohenberg and Kohn (Th. 2.2).

The energy of the interacting system E_{tot} is recovered through the total energy E_{tot}^{KS} of the non interacting one being:

$$\begin{aligned} E_{tot}^{KS} =& \sum_{\lambda=1}^{N} \epsilon_\lambda^{KS} = T_S[n] + V_S[n] \\ =& T_S + \int d\mathbf{r} \; v_0(\mathbf{r}) n(\mathbf{r}) + \iint d\mathbf{r} d\mathbf{r}' \; n(\mathbf{r}) v_H(\mathbf{r}, \mathbf{r}') n(\mathbf{r}) \\ &+ \int d\mathbf{r} \; v_{XC}(\mathbf{r}) n(\mathbf{r})|_{n=n_0} \end{aligned} \tag{2.17}$$

[4] That is, to belong to the ensemble of physical potentials that have a non-degenerate ground-state. This is a not trivial constraint to be imposed while varying the density.

[5] $v_{XC}(\mathbf{r}, [n]) = \int d\mathbf{r}' \; \frac{1}{2} \frac{n_{XC}(\mathbf{r}, \mathbf{r}'; n)}{|\mathbf{r}' - \mathbf{r}|}$.

that substituted in Eq. (2.11) gives:

$$E_{tot}^{el} = E_{tot}^{KS} - \frac{1}{2}\int d\mathbf{r}\ v_H(\mathbf{r})n(\mathbf{r}) + V_{XC}[n] - \int d\mathbf{r}\ v_{XC}(\mathbf{r})n(\mathbf{r}). \tag{2.18}$$

In order to have the total energy of the entire system one should add the term due to the Coulomb nuclei interaction.

From the knowledge of the total energy one can obtain several informations, for instance on the structure of the system under interest. As stated before, the ground state problem is solved for given nuclei positions, i.e. they enter only as parameters/constants in the electronic problem due to the BO approximation. For simple cases, i.e. the determination of the bond length of a bi-atomic molecule, or the lattice parameter in a solid crystal, one can simply minimize the total energy of the system with respect to one or few parameters. In more complex cases, with many degrees of freedom, one can extract the forces acting on each atoms from the variation of the total energy as a function of the atomic coordinates, by means of the Hellmann-Feynman theorem [39, 40]. Structural optimization could then be performed by minimizing the forces.

When precise experimental data exist, in particular for the simulation of isolated magnetic molecules (as in Chapter 4), structural optimization could be avoided. Otherwise, when the structure is unclear or we are dealing with a rather complex system, as the adsorption of molecules on surfaces (see Chapter 5), the characterization of the system in its structurally optimized geometry is of fundamental importance. Here the inclusion of dispersion forces in the energy functional will be mandatory for the correct description of the molecule-substrate distance, as we will see in more detail in the next chapter.

During the years the first formulation of the HK theorems (Ths. 2.1 and 2.2) and the KS scheme have been improved reducing the theoretical constraints i.e. adding the possibility to apply KS-DFT to spin-polarized materials, in order to study their magnetic properties. In this formulation the charge density n and the magnetization density m are defined as

$$n(\mathbf{r}) = n^+(\mathbf{r}) + n^-(\mathbf{r}), \tag{2.19}$$

$$m(\mathbf{r}) = n^+(\mathbf{r}) - n^-(\mathbf{r}) \tag{2.20}$$

and all the functionals described before becomes dependent on these two new quantities, instead on the charge density only. This is the approach that will be considered in this

thesis, since we will delve mainly with magnetic materials (molecules and substrates). We refer to the book of Dreizler for more details on the spin-polarized formulation of DFT [41].

Before concluding this section we note that the KS eigenvalues ϵ_λ^{KS} have, unfortunately, no direct physical meaning, because the KS orbitals $|\psi_\lambda^{KS}\rangle$ do not describe the one-electron wave function of the real system, but instead they only have the property to sum up to the correct total electron density $n(\mathbf{r})$. A second important point is that the theory up to now is exact for the ground state, while all the complications of the many-body problem is moved on the choice of the exchange and correlation functional $V_{XC}[n]$, and the next section will be devoted to discuss this issue.

2.2.3. Exchange and Correlation potential

All the previous equations have been formally exact, and the only approximation adopted is the Born-Oppenheimer one. But, in order treat real system we have to supply an approximate form of the exchange-correlation functional V_{XC}. [6] The majority of the calculations today are performed in the *local-density approximation* (LDA) introduced by Kohn and Sham in 1965 [37]. Similar to the Thomas-Fermi approximation, the system is *locally* considered as an interacting homogeneous electron gas: the density around a certain spatial point $\mathbf{r}$ is uniform and the $v_{XC}[n]$ functional reduces to a mere function ϵ_{XC}^{hom} of $n(\mathbf{r})$:

$$V_{XC}[n] = \int d\mathbf{r}\; v_{XC}(\mathbf{r},[n])n(\mathbf{r}) \longrightarrow V_{XC}^{LDA}[n] = \int d\mathbf{r}\; \epsilon_{XC}^{hom}(n(\mathbf{r})) \tag{2.21}$$

where

$$\epsilon_{XC}^{hom} = \epsilon_X^{hom} + \epsilon_C^{hom}, \quad \text{with} \quad \epsilon_X^{hom} = -\frac{3}{4}\left(\frac{3}{\pi}\right)^{1/3} n^{1/3}(\mathbf{r}). \tag{2.22}$$

In this particular approximation $\epsilon_{XC}^{hom}(n)$ has an analytical solution for the exchange part (Eq. (2.22)) while reliable parametrizations exist of the correlation function derived from quantum Monte-Carlo simulations of the homogeneous electron gas [42, 43]. At first glance, Equation 2.21 seems to provide good results just for slowly (in space) varying densities. Yet, it turned out that LDA supplies generally a good description of the ground-state properties of a variety of inhomogeneous physical systems, from solids to nanostructures and

[6] Note here that the most crude approximation, i.e. neglecting this term, leads to the Hartree equation, where no correlation effects whatsoever between the electrons are considered.

even molecules where the density significantly deviates from the homogeneous assumption. Typically the lattice parameters, the bond lengths and the ground state energies are in excellent agreement with the experimental results within few percents for covalent, metallic and ionic bonds. Instead, it is found that the same approximation works much worse for weak bonding situations as is the case for Hydrogen bonds or Van der Waals interactions.

The LDA energy functional does not cancel exactly the self-energy interaction of the Hartree term resulting in a wrong asymptotic behavior of the XC potential in finite systems.[7] There have been many attempts to go beyond the LDA, aiming to describe in a more accurate way the *exchange-correlation* functional. Examples are the *generalized-gradient approximation* (GGA) where the non-local corrections are introduced treating v_{XC} as function of both the density and its gradient. In this case v_{XC} can describe also fast variations of the density, whereas in LDA are approximated as negligible. Some very famous GGA functional are the PBE [44] (which is the one used in this work to study molecular spins adsorbed on magnetic surfaces, in Chapter 5) and the BLYP [45, 46]. Other more elaborated approaches are the ones of the *optimized effective potential* (OPM) [47] method or the *exact-exchange* (EXX) where the exchange part of V_{XC} is exactly treated [48]. These functionals were born to reproduce the main quantities in condensed matter physics, but tend to give a poor description of many molecular properties. To better describe molecular systems, new approximations to the exchange-correlation energy functional were created, i.e. the *hybrid functionals*, where part of the exact exchange as derived from Hartree-Fock is incorporated, together with XC from other sources (e.g. empirical or ab initio GW calculations) and some parameters/factors are defined in order to establish the reciprocal weights of these components. One of the most commonly used version is B3LYP [49], which stands for Becke, 3-parameter, Lee-Yang-Parr. Overall the use of *hybrid functionals* improves the description of atomization energies, bond lengths and vibration frequencies, as compared to what obtained in LDA or GGA [50] calculations. In the next chapter 3, when the numerical codes employed in our calculations are described and where further detail on the theoretical methods is given, we will spend some more time in discussing the importance of adopting beyond-LDA(GGA) functionals in order to correctly describe the electronic and magnetic properties of molecular systems, and their interaction with magnetic substrates.

[7] It presents an exponential decay whereas it should behave as $\frac{1}{|\mathbf{r}|}$.

Chapter 3.

Numerical Codes and Computational Details

3.1. The choice of the basis set

The analytical resolution of the Kohn-Sham equations (Section 2.8) and the corresponding knowledge of the single-particle wave functions $|\psi_\lambda^{KS}\rangle$ is a very difficult task, and requires the introduction of refined numerical methods. In the practical implementation, the unknown functions $|\psi_\lambda^{KS}\rangle$ defined in Equation 2.8 are expanded as a sum of known functions belonging to the so-called *basis set*. This approach, referred as the Hartree-Fock-Roothan method [51], was originally used in the resolution of the Hartree-Fock equations, and later implemented to solve the Kohn-Sham equations. Nowadays this method, implemented in the DFT framework in many electronic structure codes.

DFT implementations can be divided in three main groups depending if the basis set is described by (i) atomic centered functions localized in real space, where Gaussian-type orbitals (GTO) are mostly used, by (ii) delocalized functions as plane waves, or by (iii) both atomic and delocalized functions (hybrid basis set), depending on the coordinate $\mathbf{r}$ in space where the wave function is calculated. Depending on the periodicity of the system under interest, i.e. isolated molecules (0-dimensional) *cf.* surfaces or bulks (two/three-dimensional), the basis-set is chosen conveniently from one of the above group. The investigation of isolated molecules and of molecules adsorbed on surfaces will be tackled employing codes whose basis set belong to the groups i) and ii) above, respectively. For the magnetic characterization of a typical non-periodic system like the antiferromagnetic rings

and ring-dimers, that will be discussed in Chapter 4, the DFT module + localized gaussian basis set implemented in the NWChem package [23] was the preferred choice, while for the description of a periodic system with Bloch - von Karman boundary conditions like a molecule on a substrate, addressed in Chapter 5, we employed the VASP [22] package which implements a plain wave basis set + pseudopotentials approach. Among the many possible local-orbital-based packages, the NWChem code was chosen because it comprises the possibility to perform constrained-DFT, which of great help in the characterization of low-spin broken symmetry solutions. Instead, the VASP code has been selected for the study of a magnetic molecule on a (ferromagnetic) metallic substrate, because it employs Projected Augmented Wave (PAW) pseudopotentials, and it allows to perform calculations with accuracy similar to the one offered by all-electron methods in a computationally very efficient way.

In the following sections, a general description of the theoretical approaches employed in the two sets of calculation will be given; we will also describe convergence tests performed for the VASP code, in order to set 'standards' that have been later followed to obtain the results discussed in Chapter 5.

3.2. NWChem

This section intends to give a small basic overview on the theoretical approach adopted in the DFT module of the NWChem software. After a brief description on the construction of a common Gaussian basis set, the choices about the basis set and the functional will be motivated. At last, a step-by-step description of the practical calculations used to achieve the desired magnetic configuration within the constrained-DFT method [24, 25] is given.

3.2.1. Gaussian basis sets

One advantage of localized basis functions with respect to plane waves, is their linear scaling with the number of atoms. This allows for the simulation of isolated systems of large size, without the need to account for 'empty vacuum space' between the replicas. One of the main drawback is, instead, the lack of a systematic parameter to increase for checking the asymptotic completeness of the basis, i.e. an analogue to the energy/wave vector cutoff

that determines univocally the number of functions in a plane-waves basis set. In fact, the usual methodology is to add basis functions *ad hoc* that reproduces physical quantities of interest. Among the localized basis functions, the so-called Gaussian-type (GTO) and Slater-type (STO) orbitals are used at most. With respect to STOs, GTOs have wrong asymptotics in the infinity (fall down to fast) and wrong behavior near the nucleus but they presents some crucial advantages, (i) their integrals can be calculated analytically and (ii) a linear combination of few basis functions can reproduce the node structure of one-electron wavefunction. Hence the GTO are the preferred choice in most of the electronic structure programs based on localized basis functions, as NWChem. A GTO can be expressed by the following general formula:

$$\chi(\zeta, l, m, n \mid r, \theta, \phi) = N r^{(2n-2-l)} e^{\zeta r^2} Y_{lm}(\theta, \phi) \tag{3.1}$$

in this equation N is the normalization constant, ζ is the exponent, r, θ and ϕ are the polar coordinates, Y represents the spherical harmonics while n, l and m are the typical quantum numbers. The basis set with the smallest quantity of GTO are called minimal basis; for instance, in an STO-3G basis set, only 3 gaussian-type orbitals are fitted to reproduce each atomic orbitals, e.g. in the H and He case, three GTOs are used to reproduce the $1s$ orbital). A more refined basis set is represented by increasing the numbers of functions (each of which is expanded over a certain number of GTOs) associated to each orbital, and the corresponding basis set is called for instance, double-zeta (DZ), triple-zeta (TZ) etc... . After a certain atomic number, the multiplication of the functions used to describe the core electrons is quite useless because they are almost unperturbed by the chemical environment, but it is very important for the valence functions that are sensibly affected from the chemical variations. It is therefore quite common to use minimal sets, multiplying only the numbers of the valence functions, and the corresponding basis set are named VDZ, VTZ, etc..., where 'V' stand for 'valence'. Moreover it is possible to include different basis set functions depending on the element, i.e. VDZ for light atoms, e.g. H, O, F, etc.. , and VTZ for heavier transition metal atoms; this versatility is essential in our case, since the correct account of the asymmetric deformation of the partially-filled d orbitals of transition metal atoms induced by the field of the coordinating ligand-atoms is of critical importance in order to reproduce the proper physics of the magnetic molecule.

Among the various basis sets available, the Ahlrichs valence triple-ζ (VTZ) basis set for the transition metal ions and Ahlrichs valence double-ζ (VDZ) basis set for the rest of the elements were used in our calculation. Several works in the literature can be found where this choice of the basis set has demonstrated to give sufficiently accurate results for the description of exchange interactions in transition metal clusters [52].

3.2.2. Hybrid functional B3LYP for molecules

The choice of the exchange and correlation functional is of fundamental importance to simulate properly the electronic and magnetic properties of magnetic molecules. Either one uses standard LDA or GGA functionals, and corrects the missing electronic correlation by adding Hubbard on-site correlation terms in the potentials of the d orbitals, as described in Section 3.3.4, or one can utilize an hybrid functional, as anticipated in the previous chapter. One of the mostly employed hybrid functional is the B3LYP [49], which stands for Becke, 3-parameter, Lee-Yang-Parr. This functional is a linear combination of the Hartree-Fock exact exchange functional E_x^{HF} and the exchange and correlation functional provided by the LDA and GGA methods, and has the following expression:

$$E_{xc}^{B3LYP} = E_{xc}^{LDA} + a_0(E_x^{HF} - E_x^{LDA}) + a_x(E_x^{GGA} - E_x^{LDA}) + a_c(E_c^{GGA} - E_c^{LDA}) \quad (3.2)$$

where $a_0 = 0.20$, $a_x = 0.72$ and $a_c = 0.81$, E_x^{GGA} and E_c^{GGA} are the Becke 88 exchange functional [45] and the correlation functional of Lee, Yang and Parr [46] while E_c^{LDA} is the VWN local-density approximation to the correlation functional [53]. The B3LYP supply improved atomization energies, bond lengths and vibration frequencies as compared to LDA or GGA [50], and has provided results comparable to the ones obtained by the GGA+U method in the case of transition metal oxides [54]. Moreover, it has been already broadly employed in the simulation of the magnetic properties of organometallic compounds [15, 52, 55]. In hybrid functionals there is no parameter, analogue to the U in LDA/GGA+U method, that has to be chosen; the parametrization is instead done already at the level of the formulation of the functional (a_0, a_x and a_c above) and for all the atoms altogether. This has a certain'advantage' when, as it is our case, one deals with heterometallic systems; in fact, different Us should be considered in principle for different

transition metal elements, i.e. correlation effects have different weight along the transition metal series, and depending on the filling of the *d* orbitals. Because of all the above features, the B3LYP functional has been used throughout our investigation on magnetic molecules in the gas-phase.

3.2.3. Constrained DFT

The C-DFT method implemented by van Voorhis et al. [24, 25] is a versatile tool which allows to impose a particular charge or magnetization value on specific atoms or even entire molecular fragments during the self-consistent resolution of the Kohn-Sham equations, in order to obtain the chosen "constrained" state. In practice, the constraint is imposed adding a Lagrange multiplier at the standard DFT equations. To associate a certain charge or spin to one or more atoms, the Becke, Mulliken, and Löwdin population schemes can be used, and we used in our calculations the latter, which is also the default scheme in the NWChem code.

The broken-symmetry (BS) magnetic configurations in the molecular rings and dimers investigated in this thesis were obtained with the assistance of the following methodology. Although multiple constraints can be defined simultaneously, the computational time increases considerably if more than one constraint is imposed at the same footing, since for each constraints an additional self-consistent internal cycle is performed to converge the required Lagrange parameter. Moreover with more simultaneous constraints, convergence problems towards the electronic energy minimum often arise. Because of this, we never used more than two simultaneously; although there is no general rule, it is generally more efficient to use one at a time, and then use the resulting orbitals for a next step calculation with a different constraint, more than using two of them from the beginning. The majority of the magnetic moments is basically localized close to the nuclei of the metal ions; very small spin polarization is observed on the organic fragments, e.g. some tenth of Bohr magnetron at most. Accordingly, spin moments were constrained only on one or more metal ions but not on their coordinating ligands. Unfortunately, when the C-DFT is applied on molecules with a significant number of magnetic centers (in our cases, at most 16), converge problems can emerge during the self-consistent cycle, despite the observations above. Often, the imposed magnetic moments get lost on some atoms or the calculation do not simply find a energy minimum, and self-consistency is not achieved even within hundreds of electronic

iterations. This problem is especially critical when one starts a calculation from scratch with a large basis set as the Ahlrichs valence triple-ζ (VTZ). After many tests, we ended up with a practical scheme that allowed us to converge within few steps to the desired BS state. Our calculations start by employing a minimum basis (STO-3G) and imposing a ferromagnetic state for all the metal ions in the system. Due to the inaccuracy of this minimal basis set, we often attain on the metal ions wrong (in value) spin solutions, but this is not of much importance as long as the correct sign of the spin is captured. The wave-function obtained by this first calculation is used as initial guess, flipping only the spin moments on small groups of metals (all or a subgroup of the ones that must have their spin reversed). This flipping step is reiterated (usually two steps are necessary) until the desired spin sign distribution is achieved. We can then read in the STO-3G orbitals converged from the previous calculations, and project them onto a larger basis; experience says that it is more safe to project them onto a double-zeta basis first (VDZ) and finally project from the double-zeta onto the desired large basis set, with triple-zeta precision, i.e. VTZ.

3.3. VASP

In our investigation on the adsorption of the $CoCp_2$ on graphene/Ni(111) several tools of the VASP code were employed. This code works with plane-waves basis in form of pseudopotentials. In order to give a general idea on the functioning of the VASP, the theory behind the plane-waves expansion is presented briefly with particular emphasis on the concept of pseudopotentials. The effects of some important corrections represented by the Van der Waals dispersion interactions [27] and the on-site Coulomb interactions [28] are also considered in order to reproduce correctly the physical properties of our system. In the end of this Section some of the most important internal parameters that must be converged (e.g. energy cutoff and k-point Grid) are introduced, and converge tests discussed in detail.

3.3.1. Plane-Waves basis set and supercell technique

When one deals wit a crystal lattice or, in general, a periodic system, equations and wave functions are significantly simplified by means of Bloch's theorem, and plane-waves become

the natural basis set to represent the solution of the KS equations:

$$|\psi_\lambda^{KS}(\mathbf{r})\rangle = |\psi_{n\mathbf{k}}(\mathbf{r})\rangle = \psi_{n\mathbf{k}}(\mathbf{r}) = u_{n\mathbf{k}}(\mathbf{r})\, e^{i\mathbf{k}\cdot\mathbf{r}} = \sum_{\mathbf{G}} c_{\mathbf{G}}(n\mathbf{k}) e^{i\mathbf{G}\cdot\mathbf{r}}\, e^{i\mathbf{k}\cdot\mathbf{r}}, \tag{3.3}$$

where λ can be identified by the band index and wave-vector $n, \mathbf{k}$. $\mathbf{k}$ is a continuous variable[1] belonging to the 1^{st} Brillouin Zone that identifies the reduced momentum of the state and $\mathbf{G}$ are the discrete reciprocal lattice vectors. The Schrödinger equation in this basis is represented by a secular equation where the new variables are the coefficients $c_{\mathbf{G}}(n\mathbf{k})$; the corresponding Hamiltonian is obtained applying $\langle e^{i\mathbf{G}'\cdot\mathbf{r}}|$ to the KS equation where $|\psi_\lambda^{KS}(\mathbf{r})\rangle$ is replaced by its Bloch's expansion (Eq. (3.3)). That is:

$$\sum_{\mathbf{G}} \hat{H}_{\mathbf{G}\mathbf{G}'}(\mathbf{k}) c_{\mathbf{G}}(n\mathbf{k}) = \epsilon_{c_{\mathbf{G}}(n\mathbf{k})} c_{\mathbf{G}}(n\mathbf{k}) \tag{3.4}$$

$$\begin{aligned} \hat{H}_{\mathbf{G}\mathbf{G}'}(\mathbf{k}) =& \frac{1}{2}|\mathbf{k}+\mathbf{G}|^2 \delta_{\mathbf{G},\mathbf{G}'} + V_{ext}(\mathbf{k}+\mathbf{G}, \mathbf{k}+\mathbf{G}') + \\ & V_H(\mathbf{G}-\mathbf{G}') + V_{XC}(\mathbf{G}-\mathbf{G}'). \end{aligned} \tag{3.5}$$

Similarly to the real space, the reciprocal coordinates determined by $\mathbf{k}$ and $\mathbf{G}$, should be finite and discrete for practical implementation. This is achieved by (i) considering the plane-waves up to a certain threshold value of $\mathbf{G}$ and (ii) using a finite grid of representative k-points for the k sum/integration over the 1st Brillouin zone. This basis demonstrates to be very efficient and shows several advantages:

- plane-waves are a complete set of orthogonalized functions where the quality of the sampling can be easily improved increasing the number of considered waves (energy/wave vector cutoff).
- Its definition is independent on the system but only depends on the simulation cell, and does not require a knowledge of the atomic orbitals involved or the atomic positions.
- The equations are considerably simplified in the reciprocal space, in particular the differential terms as the kinetic energy or the Hartree potential (evaluated from the Poisson equation) reduce to simple products.

[1] This is the case of Bloch's states where periodic boundary conditions are applied resulting in an infinite dimension material, whereas for real systems $\mathbf{k}$ is discrete and becomes continuous only in the thermodynamic limit.

- Passing through direct and Fourier space with plane-waves is also computationally efficient thanks to the Fast Fourier Transform (FFT) algorithm.

Because of these advantages it is usually convenient to treat with the same basis also systems with less than three-dimensional periodicity i.e., surfaces and nanowires, or bulk solids with point defects (that lack of the correct lattice symmetry) or superlattices. For confined systems this can be done by inserting vacuum space into the non-periodic dimension and imposing periodic *Born-von Karman* boundary conditions at all the edges of the simulation cell. The quantity of vacuum used to decouple the system in its confined direction must be checked carefully, in order to avoid fictitious interaction between the system's replicas. This method takes the name of *supercell technique*, and it is largely exploited with success even for the simulation of small confined systems as molecules, where the states are strongly localized and there is a complete lack of periodicity.

3.3.2. Pseudopotential

Up to now we have considered all the electrons involved in the many-body problem. However, only *valence* electrons participate to chemical bonds and interactions among the atoms in a material. Valence electrons are the responsible of its structural and electronic properties hence should be accurately described, while *core* electrons are confined in a region close to the atomic nucleus, and their direct involvement as a variable of the many-body problem can be neglected. As stated above, core wave functions and density n_c are almost independent on the chemical environment and can be assumed to be equal to their atomic configuration (*frozen-core approximation*). They can be thus obtained from an all-electron calculation for the single atoms, and subsequently included together with their effects in the nuclei potential they surround, forming a fixed *frozen-ion*. Within the frozen-core approximation, the DFT calculation should then take into account only valence electrons and density n_v. Nevertheless the procedure demonstrates complex because core electrons are fermions indistinguishable from the valence ones with which they interact. Consequently one should still imposes constraints on valence wave functions to be orthogonal to the core states. In addition the XC functional $V_{XC}[n_c + n_v]$ is nonlinear and it becomes not trivial to separate the two contributions $V_{XC}[n_c] + V_{XC}[n_v]$ without introducing further approximations. This condition is fulfilled when the two densities n_c and n_v are spatially separated so that their overlap is zero and XC energy vanishes. If this happens for some of the deeper (more

energetic) core electron which form a close shell with very small overlap with valence shells, is is not in general true for shallow core electron which are not far in energy (some tens of eV) from the valence energy window.

The *frozen-core approximation* allows also to solve further problems related to the plane waves basis set. Indeed the ion Coulomb interaction presents a singularity at the nucleus, that is not completely removed by the screening effect of the core electrons. As a consequence their wave functions rapidly oscillate and the same is induced by orthogonality on the valence states in the core region. An accurate description of the latter would then require high-frequency plane waves with large cut-off energy. But, the observation of what is effectively important to describe the properties of the materials shows that chemical bounds are largely independent on the behavior of valence wave functions inside the core region. The simple idea that derives from this consideration is to replace the real KS eigenfunctions with other *pseudo*-functions that have the same chemical properties and shape outside a certain core region, while being smoother and node-free inside it. This would make the KS algorithm numerically simpler and faster, requiring a smaller number of basis plane waves. The purpose can be obtained redefining the ion-potential (given by the nucleus and the core electrons from an all-electron calculation), with a *pseudopotential* that removes completely the core orbitals from the simulation; the strong oscillations within a cut-off radius are, in this way, eliminated and so it is the Coulomb singularity. In order to be employed, pseudo-potentials are required to obey to some constraints/requirements:

- the preservation of the KS energies,
- the conservation of the KS wave functions outside a sphere of cut-off radius r_c, together with their logarithmic derivative (the scattering properties) at the surface of the sphere,
- the conservation of the total density inside the sphere,[2]
- the pseudopotential $\hat{V}_{ext}^{ps}$ must be a spherically symmetric hermitian linear operator.

In this way, one can fit the remaining parameters to soften the valence wave function inside a core region of radius r_c. These pseudopotentials are then substituted directly into the external potential in the KS equation.

In the first attempts (in the 1960's), screened pseudo-potentials where empirically designed to fit experiments. Nowadays it exists a variety of *ab initio* pseudopotentials

[2]This is required only for the so-called norm-conserving pseudopotential.

satisfying additional requirements as norm conservation, portability [3] and the inclusion of nonlocal terms in order to correctly reproduce the different phase shift and scattering properties for each angular momentum components of the wave function [56]. Among the various schemes proposed in literature, the Troullier-Martin type [57] are quite common. In the following, we discuss another possible route, which has become of much use in the latter years, to solve efficiently, and with high accuracy, the KS equations.

Projector Augmented Wave method

The numerical calculations performed on the periodic systems investigated in this thesis were done using an extension of the pseudopotential technique known as the projector augmented wave method (PAW) [26], implemented in the VASP code [22,58] in combination with the Perdew-Burke-Ernzerhof (PBE) exchange correlation functional [44] described previously in Section 2.2.3).

In the PAW approach the single-particle wave function $|\psi_\lambda^{KS}\rangle$ is related to his pseudo version $|\tilde{\psi}_\lambda^{KS}\rangle$ by the linear transformation $\mathcal{T}$:

$$|\psi_\lambda^{KS}\rangle = \mathcal{T}|\tilde{\psi}_\lambda^{KS}\rangle \tag{3.6}$$

$|\psi_\lambda^{KS}\rangle$ and $|\tilde{\psi}_\lambda^{KS}\rangle$ differ only in the region near the atom centers where the all-electrons function has rapid oscillations while the pseudo function has a smooth trend.

We can express $\mathcal{T}$ in the intuitive form

$$\mathcal{T} = 1 + \sum_R \hat{\mathcal{T}}_R \tag{3.7}$$

where $\hat{\mathcal{T}}_R$ is non-zero only within some spherical region enclosing the atom R. Around each atom the pseudo wave function $|\psi_\lambda^{KS}\rangle$ is expanded in pseudo partial waves basis $\tilde{\phi}_i$

[3] That means that it can be used with equal success independently on the valency and the electronic configuration in which the element is found.

(solutions of Schrödinger equation for the isolated atoms are a good choice). In this new basis we define also the effect of the linear transformation for a particular atom R-th as:

$$\hat{\mathcal{T}}_R|\tilde{\phi}_i^R\rangle = (|\phi_i^R\rangle - |\tilde{\phi}_i^R\rangle) \tag{3.8}$$

The total pseudo function can be expanded in pseudo partial waves:

$$|\tilde{\psi}_\lambda^{KS}\rangle = \sum_R \sum_i c_i^R |\tilde{\phi}_i^R\rangle \tag{3.9}$$

Because the operator $\mathcal{T}$ is linear, the coefficients c_i^R can be written as an inner product with a set of so-called projector functions, $|\tilde{p}_i^R\rangle$ defined as duals of the auxiliary functions (e. g. $\langle\tilde{p}_i^R|\tilde{\phi}_j^{R'}\rangle = \delta_{ij}\delta_{RR'}$), so each coefficient c_i^R can be written as :

$$c_i^R = \langle\tilde{p}_i^R|\tilde{\psi}_\lambda^{KS}\rangle \tag{3.10}$$

This coefficients could be considered as the analogues to the augmentation coefficients in the Linearized Augmented Plane Wave (LAPW) technique [59] that instead are found by matching in value and derivative the augmented waves inside muffin-tin spheres and plane waves outside them on the surface of the muffin-tin spheres themselves. Actually it could be demonstrated that the LAPW method could be derived, as a special case of the PAW method [26].

At last is shown the final form of the Equation 3.6:

$$|\psi_\lambda^{KS}\rangle = |\tilde{\psi}_\lambda^{KS}\rangle + \sum_{i,R}(|\phi_i^R\rangle - |\tilde{\phi}_i^R\rangle)\langle\tilde{p}_i^R|\tilde{\psi}_\lambda^{KS}\rangle \tag{3.11}$$

The decomposition shown in Equation 3.11 separates the different types of waves, the one smooth everywhere and the one which contains rapid oscillations, so that they are

treated individually. Once uniquely defined how the on-site PAW transformation works, a large number of data for each chemical element can be pre-calculated, saving a big amount of time during the real calculations. We refer to the original work by Blöchl [26] for a detailed description of the PAW method. It is important to state here that the results obtained by this method are as accurate as the ones supplied by all-electrons methods, but being in the same time much more efficient from the computational point of view. Because of this, the PAW method has been used with success in many theoretical characterizations of magnetic substrates [8, 9, 60, 61].

3.3.3. van der Waals interactions

The van der Waals' (vdW) forces represents the sum of the forces, between molecules/nanostructures, due to electrostatic interaction between permanent or induced dipoles. Albeit these forces are relatively weak compared to the ones responsible for covalent or ionic bonds, they play a fundamental role in countless situations and, in particular, in surface science. The weakest of them, the London dispersion force (LDF), arises from quantum-induced instantaneous polarization multipoles, and it is of crucial importance to accurately describe the molecule-surface system investigated in this thesis. Indeed, when the graphene is adsorbed on the Ni(111) surface, the attractive force which bind the two layers is mainly due to the vdWs/LDFs. Unfortunately, the typical DFT functionals fail to reproduce the long-range attractive part of the dispersive interaction; it this is true for LDA, which has a tendency of overestimate such interaction, it is more dramatic for GGA, that on the other hand, miss almost completely to account for them, resulting in non-binding behavior in many cases. Currently there are two different approaches to add dispersion forces in standard DFT calculations. The first one, introduced by Grimme in 2006 [27], named DFT-D2 simply adds semi-empirical potential terms in the Hamiltonian, via a simple pair-wise force field (it scales then with the number of atoms in the cell). In this approximation, the dispersion energy is defined as

$$E_{disp} = -\frac{s_6}{2}\sum_{i=1}^{N}\sum_{j=1}^{N}\frac{C_6^{ij}}{|\mathbf{r}_{ij}|^6}f(|\mathbf{r}_{ij}|) \tag{3.12}$$

where the summations are over all atoms N, s_6 is a global scaling factor, $\mathbf{r}_{ij}$ is the actual distance between the atoms ij, $\mathbf{R}_0^{ij}$ is the sum of the nominal vdW radii of the two atoms i and j, C_6^{ij} denotes the dispersion coefficient for the atom pair ij. The term $f(|\mathbf{r}_{ij}|)$ is a damping function necessary to minimize the dispersion contribution within typical bonding distances.

$$f(|\mathbf{r}_{ij}|) = \frac{1}{1 + e^{-d(|\mathbf{r}_{ij}|/\mathbf{R}_0^{ij} - 1)}} \tag{3.13}$$

The second approach uses a non-local exchange-correlation energy functional called generally vdW-DF [62] and it scales with the number of Fast Fourier Transform grid points (i.e. the size of the simulation cell), while it's almost independent on the number of the atoms. The relative increase in the computational cost is therefore high for isolated molecules in large cells, but small for solids described by smaller repetition cells. Using the vdW-DF ab-initio method for graphene/Ni(111) an equilibrium distance between graphene and the topmost Ni layer greater than 3.5 Å is found for all the calculated stacking, in disagreement with the LEED experimental data [63]. In the case of the DFT-D2 the estimate of the binding energy is less reliable, however the typical errors never exceed 20 %; more importantly, on average, the distances obtained with this method for small aromatic systems underestimate only by about 5 % the experimental values [27]. In light of the fact that, in our calculations, it was essential to get the right equilibrium distances as reliable as possible, the semi-empirical potential DFT-D2 was preferred over the DFT-DF method. By using this potential, we were able to reproduce with great accuracy the experimental distance of 2.1 Å between graphene and a Ni(111) substrate. Figure 3.1 displays the potential energy surface of the graphene-Ni(111) interaction, calculated for a small p (1 × 1) hexagonal supercell (6 atoms, 2 C and 4 Ni), as a function of the graphene-Ni distance, with and without DFT-D2 corrections. Two different set of k-points are used in order to identify the grid-mesh necessary to achieve reliable results. The plots confirms that the GGA functional fails to reproduce the correct minimum in absence of the dispersion correction. According to the nature of the semi-empirical correction we used, few k-points are sufficient to reproduce the correct potential curve.

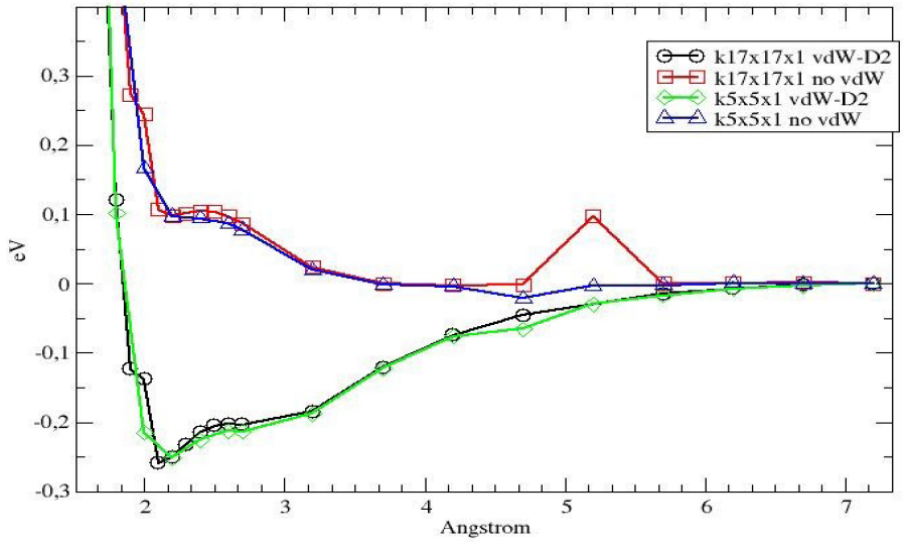

Figure 3.1.: Potential energy surface for the graphene/Ni(111) without and with vdW interaction, as implemented in the DFT-D2 method

3.3.4. GGA+U method

As described previously in several occasions, the DFT fails to describe with accuracy some materials with ions containing partly filled valence d or f shells. The origin of this failure is associated to an inadequate description of the strong Coulomb repulsion between the electrons localized on the metal ions. The application of an effective Hubbard U on transition metals oxides solves these problem, giving enhanced electron energy loss spectra and values of the lattice constant, cohesive energy and elastic moduli. Although the results presented in Chapter 5, are all obtained with standard GGA functionals, we have performed tests employing the +U approach, in order to check the validity of our results. Among the different flavors of GGA+U implemented in VASP, we have chosen to use the *rotationally invariant* version given by Dudaderv et al. [28]. The energy, in this case, takes the following form:

$$E_{GGA+U} = E_{GGA} + \frac{(U-J)}{2} \sum_{\sigma} \left[\left(\sum_{m_1} n^{\sigma}_{m_1,m_1} \right) - \left(\sum_{m_1,m_2} \hat{n}^{\sigma}_{m_1,m_2} \hat{n}^{\sigma}_{m_2,m_1} \right) \right] \tag{3.14}$$

in this approach the parameters U and J do not enter separately, but only the difference $(U - J)$ is meaningful. We imposed static correlation effects on the d electron of Co in $CoCp_2$ (values of U-J=2 and 4 eV has been tested). While the value of the spin moment associated to the Co atom does not change appreciably, the magnetic coupling for $CoCp_2$ on graphene/Ni(111) changed from -9.7 to -10.5 meV , while for the case of graphene/Fe/Ni(111) substrate it was modified to even a smaller extent. We conclude therefore that the employed GGA exchange correlation potential describes the magnetic properties of the investigated systems with sufficient accuracy.

3.3.5. Test calculations

Plane-wave energy cut-off

As anticipated in Eq. 3.5, the kinetic energy in reciprocal space assumes the simple form:

$$-\frac{\nabla^2}{2} \rightarrow \frac{(\mathbf{k}+\mathbf{G})^2}{2}. \tag{3.15}$$

It is therefore natural to define a cut-off energy E_{cut} to truncate the infinite expansion over the $\mathbf{G}$ vectors as:

$$\frac{(\mathbf{k}+\mathbf{G})^2}{2} < E_{cut}. \tag{3.16}$$

This approximation is possible since the coefficients $c_{\mathbf{G}}(\mathbf{k}n)$ of Eq. (3.3) vanish exponentially when increasing the associated kinetic energy. As a consequence the first terms are typically the most important. Nevertheless the approximation can be systematically improved including higher spatial-frequency contributions by increasing the cut-off energy. (although for very large cut-offs over-completeness of the basis set is reached, and the results deteriorate). E_{cut} is obviously dependent on the system of interest (type of elements) and it reveals to be dependent on the physical quantity that one intend to study. Indeed, convergence of ground-state total energies are very slow, but forces (used in atomic relaxations and lattice parameters optimization), as well as charge and spin density associated to the atoms, converge much more quickly with respect to E_{cut}. Moreover variations of the total energy related to the different atomic configuration and density are always greater than the systematic error that is associated to the basis truncation. Since we map the problem

into a discrete $\mathbf{G}$ grid, increasing the sphere radius E_{cut} of Eq. (3.16) or varying the grid (e.g. modifying the lattice parameter) will change of a discrete amount the number of plane waves. This sudden change can affect the other quantities as the total energy, introducing discontinuities. The problem is usually avoided defining smearing and damping functions on $u_{n\mathbf{k}}(\mathbf{G})$ close to $|\mathbf{G}|$ cut-off. For the magnetic systems investigated in Chapter 5, the physical quantity of interest was the magnetic coupling constant between the molecule and the magnetic substrates, so the E_{cut} were chosen so that this property was converged up to a desired precision. An energy cut-off of 400 eV was selected, which is also the value suggested by default, considering the type of pseudo-potentials (PAW) used in the calculations. With the aim of double-check the exchange parameters obtained with VASP, the same calculations were carried out also with an ab initio software based on plane waves called Quantum Espresso (QE). This open-source code is one of the most widely used in condensed matter calculations. QE employs PAW pseudopotentials and therefore it was necessary to converge the calculations over the energy cut-off. The test results together with the computational details will be discussed in Appendix B.

k-point Grid

The evaluation of the quantities of interest $n(\mathbf{r})$ from the Bloch's states $|\psi_{n\mathbf{k}}(\mathbf{r})\rangle$, requires to perform an integration over the vectors $\mathbf{k}$ that belong to the 1^{st} Brillouin Zone (BZ) ($\Omega_{0\mathbf{k}}$):

$$n(\mathbf{r}) = \sum_{n} \frac{1}{\Omega_{0\mathbf{k}}} \int_{\Omega_{0\mathbf{k}}} d\mathbf{k}\ |\psi_{n\mathbf{k}}(\mathbf{r})| f(\epsilon_{n\mathbf{k}}) \tag{3.17}$$

where $f(\epsilon_{n\mathbf{k}})$ represents the occupation number of the band n at point $\mathbf{k}$. Wave functions are usually slowly varying in $\mathbf{k}$ and can be considered constant for two $\mathbf{k}$ points that are close together. This makes the sampling of the Brillouin Zone by a discrete set of $\mathbf{k}$ points a good approximation to the integral. As for plane waves, the resulting error can be systematically reduced increasing the density of the $\mathbf{k}$-point grid. The KS equations for a crystal (Eq. 3.4) should be solved for each sampling point $\mathbf{k}$. In order to reduce the computational effort there have been several attempts to construct representative mesh with the fewest number of points. Among these, Monkhorst-Pack [64] grids demonstrated particularly efficient: they are regular grids invariant under the point symmetries of the system. The calculation can then be restricted to points belonging to the Irreducible Brillouin Zone Ω_0^{IRR} that are symmetrically inequivalent, while the other contribute only to the weight factor $w_{\mathbf{k}}$ of the

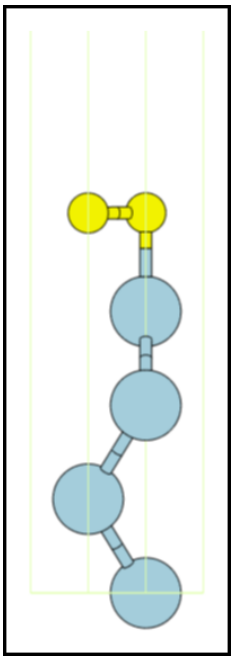

Figure 3.2.: The minimal cell for the graphene/Ni(111). The C and Ni atoms are colored yellow and cyan, respectively

former in the summation:

$$n(\mathbf{r}) = \sum_{n} \sum_{\Omega_0^{IRR}} w_{\mathbf{k}} |\psi_{n\mathbf{k}}(\mathbf{r})| f(\epsilon_{n\mathbf{k}}) \tag{3.18}$$

The number of **k**-points is consequently decreased and optimized. We started our investigations using a minimal hexagonal cell to simulate the graphene/Ni(111) interface (6 atoms) (see Figure 3.2).

Although shifting the origin of the grid off the Γ point, and inducing the **k**-points to sit off symmetry directions might improve in some cases the convergence [65], in the case of an hexagonal cell it is preferred the use of a Γ-centered (not-shifted) grid, which keeps the symmetry of the cell, since it converges significantly faster with respect to standard (shifted) Monkhorst-Pack grids. Our primitive (1 × 1) cell converged nicely with a (17 × 17 × 1) **k**-point grid; here we looked at the values of charge and spin densities on the atoms, and the values of the forces acting on the atoms (for a non relaxed structure). In the case of the molecule-substrate system, the quantity of interest we need to converge is the exchange interaction between the spin of the molecule and the magnetization of the substrate (see Chapter 5). For k-point convergence, it is not important only the amount of

k-points and the type of the grid (e.g. Monkhorst-Pack), but also other two parameters becomes important, i.e. the smearing method and the amplitude of the smearing parameter σ. The smearing determines how the partial occupancies are set for each orbital in the calculation so they greatly affect the electronic structure of the system including, as we will see, its magnetic properties. Obviously if for a small cell composed by few atoms (primitive cell described above), there is no particular problem in reaching convergence of the **k**-points grid, for whatsoever choice of the smearing method. In case of a large calculation (our molecule-substrate system contains a molecule composed of 21 atoms, and a substrate composed of 150 atoms, for a total of 171 atoms) because the computational demand is high, it is very important to keep the number of **k**-points as small as possible, and this could critically depend on the type of smearing adopted.

The three main smearing methods implemented in VASP and tested for our systems were :

- Linear tetrahedron method (LTM): this method is based on a linear interpolation of the function integrated on tetrahedrons in the 1^{st} BZ, it is the fastest and gives a very accurate description of the total energy in insulators and semiconductors as well as bulk metals.
- Gaussian Smearing Method (Gauss): it approximates the step function by a Gaussian like function, it leads to reasonable results in most cases and is suggested for supercell with a few K-points in combination with a small σ, typically 0.05 (this will be our method of choice).
- Methfessel-Paxton (MP-N) scheme: it expands the step function in a complete set of orthogonal functions of order N and is the most tunable and gives very accurate description of the total energy in metals.

Since we had to perform systematic calculations on this large system, we tested carefully how the various smearing method perform in the calculation of the magnetic coupling of the $CoCp_2$ adsorbed on graphene/Ni(111) (graphene deposited on 4 Ni layer). Here the molecule has been placed in a generic adsorption site (different from the ones presented in Section 5.3.2). Figure 3.3 displays how the exchange coupling (E_{ex} is defined as $E_{ex} = E_{AP} - E_P$, where E_{AP} (E_P) is the total energy of the system when the spin moment of the $CoCp_2$ is antiparallel (parallel) to the one of the Ni slab) varies as a function of the smearing method and an increasing number of k-points. As expected, for a large enough sampling,

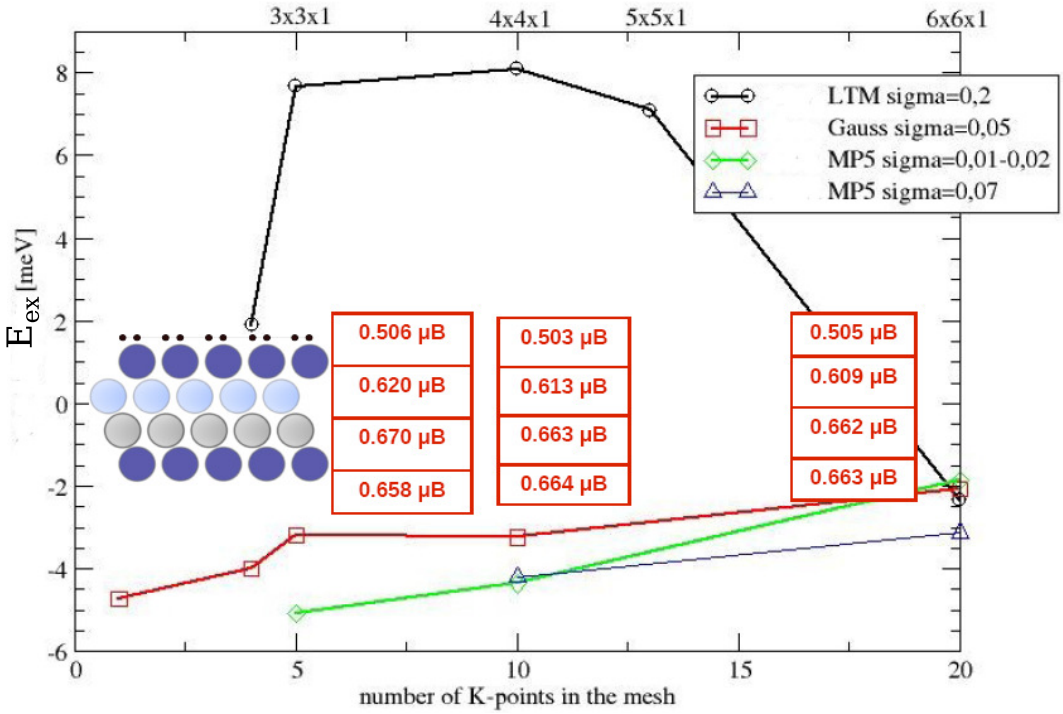

Figure 3.3.: The molecule-substrate exchange coupling as a function of the number of **k**-points for several types of smearing methods and size of σ. In the middle left a sketch of graphene/Ni(111) structure is given, and in the red tables the spin moments of the 4 Ni layers used to compose the Ni(111) slab is also given for the (3×3), (4×4) and (6×6) grids

.

all the smearing method converged to the same result but clearly with different speeds. The LTM method has been found to show the most critical convergence and only moving from a (5×5, 13 **k**-points) to a (6×6, 20 **k**-points) grid, E_{ex} seems to settle to the correct result. Both Gaussian and MP smearing perform rather nicely, but the latter smearing method appears to give a value which is within E_{ex} within 1 meV from the converged one already for a (3×3, 5 **k**-points) grid. In the red tables the corresponding spin moments of the four Ni layers, as obtained with the Gaussian smearing method, are given; we observe that the Ni spin moments are already converged within 0.01 Bohr magnetons already for the (3×3) **k**-point grid.

At the early stages of our test calculations we checked also another possibility, that we show here just for completeness. Instead of using a grid of **k**-points in the BZ, and checking the convergence of the BZ integration (important in order to correctly describe

the properties of the itinerant/delocalized electrons in the graphene/Ni(111) susbtrate), it is also possible to increase the size of the simulation cell, considering the **k**-point grid composed of only the Γ-point. This is motivated by the fact that an enlargement of the cell size in the real space produce a decreasing of the dimension for the reciprocal space. This means that for a very large supercell, only the Γ-point becomes sufficient to map the wave-function in the BZ. Usually this is not a convenient procedure from the computational point of view, but in the case of the VASP code, it could eventually turn out to be more efficient since the Γ-point binary executable, due to different implementations in the code, is much faster than the one needed for a finite ($\neq 1$) number of **k**-points. After having identified the best smearing for our system, the magnetic coupling was checked using only the Γ-point and varying the size of the supercell in the x-y plane. In order to keep the computational effort tractable, for this calculation, only three Ni layers have been considered to compose the Ni(111) slab, instead of the four used in the tests above and for the final results. Both the magnetization and the magnetic coupling were not converged even in case of a 10×10 reals-space supercell, as evident from Figure 3.4. The computational cost of a (10×10) supercell simulation in the Γ-point version was almost equivalent to a (5×5) supercell simulation with 5 k-point. Although the results were promising because the antiparallel state was still favored in all the calculations, oscillations were still to large to consider it as the method of choice, and no clear convergence is observed even for the (10×10) supercell. Due to the above tests, we therefore concluded that the more accurate methodology to simulate the magnetic properties of our molecule/graphene/Ni(111) system is embodied by the use of a (5×5) supercell with a Γ-centered grid of $(3 \times 3 \times 1)$ **k**-points, together with the Gaussian smearing method.

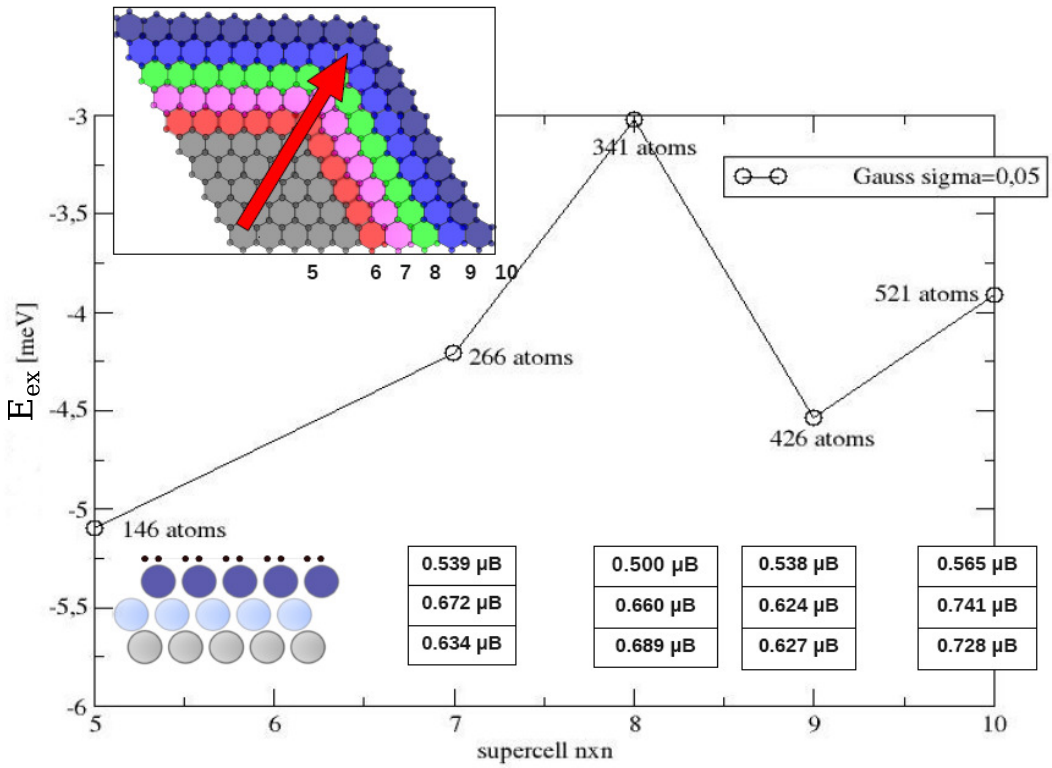

Figure 3.4.: The molecule-substrate exchange coupling as a function of the supercell size. In the upper left we give a color-coded sketch of the in-plane cells of increasing dimensions. In the tables, the spin moments of the 3 Ni layer for various supercell sizes are also reported.

Chapter 4.

Magnetic coupling in antiferromagnetic spin rings and dimers

4.1. A brief introduction to magnetic molecules

In the last decade a growing interest has been devoted to the realization and the study of magnetic molecules. These systems are constituted by one or more magnetic nuclei surrounded by organic chemical groups. Usually the magnetic cores are composed by transition metals, rare-earth ions or even organic radicals, while the organic bridges comprise light elements like C, O, H and N atoms. Although these materials appear as macroscopic samples, i. e. crystals or powders, the intermolecular magnetic interactions are in most cases negligible as compared to the intramolecular ones. This is particularly true when the total spin S associated to each molecule is not too big and the intermolecular dipolar interactions are weak. The molecular crystals could then be regarded as a monodisperse collection of non-interacting magnetic units. As a consequence, solid state experimental techniques for the measurements of thermodynamic and magnetic properties of the crystal probe at the macroscopic scale the microscopic quantum properties of the single molecules. Several classes of magnetic molecules could be defined according to their magnetic properties; among them, single molecule magnets (SMMs), photomagnetic derivatives, spin-cross-over (SCO) derivatives, single-chain magnets and antiferromagnetic rings. SMMs are magnetic molecules characterized by high anisotropy barriers [66,67] and high spins. The most popular

and perhaps most studied molecule of this class is the $Mn_{12}-$acetate [68]. Photomagnetic derivatives exhibit a photo-responsive magnetic behaviour, namely they can acquire or lose magnetic properties upon light irradiation; the most promising systems are Co−Fe Prussian Blue analogues, (i.e. compounds with the same structure and similar chemical make up of Prussian Blue) [69]. SCO derivatives are magnetic molecules where an external stimulus such as a variation of temperature, pressure, light irradiation or influence of a magnetic field can modify the crystal field splitting of the metallic ions, thus changing their spin state; among the many compounds showing SCO effects some examples are the $Fe(phen)_2(SCN)_2$ and the $[Fe^{II}(tmphen)_2]_3[Co^{III}(CN)_6]_2$, these compounds change their properties respectively for a pressure and a thermal perturbation [70]. Single-chain magnets are molecules characterized by strong intra-chain and weak inter-chain magnetic interactions; this class of compounds counts numerous ferromagnetic or antiferromagnetic compounds, but their synthesis is still not fully under control [60]. In this thesis we focus on the class of antiferromagnetic spin rings (AFRs). Due to the predominant antiferromagnetic character of the interaction between the magnetic ions these systems molecules belonging to this class show low total spin or, in the case of even-membered homometallic AF rings, a fully compensated total spin (S=0). Some molecules of this class contain Fe^{3+}(s=5/2) ions, like Fe_6 [71, 72] and Fe_{10} [72, 73] while there is another large family based on Cr^{3+} (s=3/2) like Cr_8 [74–76], which are our main interest in this thesis, and will be covered extensively in the next paragraphs.

4.1.1. Spin Hamiltonian description

The properties of magnetic molecules can be successfully described by a microscopic spin model Hamiltonian, where the spins of the magnetic ions interact with each other and with the molecular environment in different ways. This description is accurate since in molecules the magnetization density is localized in the vicinity of the ions and the spin degrees of freedom could be decoupled, in first approximation, from the electronic ones. We describe here the form of the Hamiltonian for a generic magnetic molecular system. The total Hamiltonian can be written as the sum of several contributions:

$$\mathcal{H} = \mathcal{H}_{ex} + \mathcal{H}_{cf} + \mathcal{H}_{dip} + \mathcal{H}_{Zeeman} \tag{4.1}$$

The $\mathcal{H}_{ex}$ term represent the exchange coupling, it arises from electrostatic interaction between nearest neighbor (in first approximation) metal centers. Such interaction can be described by the isotropic Heisenberg exchange Hamiltonian [77]:

$$\mathcal{H}_{ex} = -\sum_{i>j=1}^{n} J_{ij}\mathbf{s}_i \cdot \mathbf{s}_j \tag{4.2}$$

where J_{ij} are the exchange constant and s_i is the spin of the i-th metal ion, and n is the number of magnetic ions in the molecule; this is normally the leading order term of the Hamiltonian H. $\mathcal{H}_{cf}$ is the Hamiltonian corresponding to the crystal field:

$$\mathcal{H}_{cf} = \sum_{i}^{n} \mathbf{s}_i \cdot \mathbf{D}_i \cdot \mathbf{s}_i \tag{4.3}$$

where $\mathbf{D}_i$ is the crystal field anisotropy that is the sum of the *axial* and *transverse* contributions, with respect to the easy axis magnetization, and it is due to the spin-orbit coupling. $\mathcal{H}_{dip}$ represents the dipolar interactions:

$$\mathcal{H}_{dip} = \sum_{i>j=1}^{n} \mathbf{s}_i \cdot \mathbf{D}_{i,j} \cdot \mathbf{s}_i = \sum_{i>j=1}^{n} \frac{\mu_0 \mu_B^2}{4\pi \mathbf{r}_{i,j}^3}(3(g_i\mathbf{s}_i \cdot \mathbf{r}_{i,j})(g_j\mathbf{s}_j \cdot \mathbf{r}_{i,j}) - (g_i\mathbf{s}_i \cdot g_j\mathbf{s}_j)) \tag{4.4}$$

where $\mathbf{r}_{i,j}$ is the distance between the spins, g_i is the gyromagnetic factor and μ_B the Bohr magneton. If an external magnetic field $\mathbf{H}$ is present, also the *Zeeman* interaction should be taken into account:

$$\mathcal{H}_{Zeeman} = \mu_B \sum_{i}^{n} g_i \mathbf{H} \cdot \mathbf{s}_i \tag{4.5}$$

In this Hamiltonian we omit the long-range interactions that couple the spins of two different molecular units, i.e. i and j run within each molecular unit, because they are negligible in most cases if we consider that no super exchange paths between the molecules are available and that inter-rings dipolar interaction are minimized by the small total spin S. Other spin-orbit driven term, such as Dzyaloshinskii-Moriya interaction are usually very

small, and different from zero only for non-collinear arrangement of the spins. In particular for AFR, also dipolar interactions are small and, if no-spin orbit coupling is included, one is left with the plain isotropic exchange term, as we will see in the following. The observables which are obtained from the solution of this spin model Hamiltonian are fitted to experiments of different kind, e.g. magnetic susceptibility, neutron magnetic scattering and specific heat, to name a few, and the values of the parameters J, D and S are in this way obtained. It is also possible, and we will describe how in the following section, to extract the parameters from theoretical calculations; this allows an indirect comparison between the calculated parameters and the ones fitted to reproduce the experiments. We will see that in some cases such agreement is only qualitative due to approximations adopted in the calculations. Yet, theoretical results could help the experiments in those cases where unique fitting is not possible, or when the molecules are large and parameters are many.

4.1.2. Extraction of the exchange interactions from DFT

The knowledge of the microscopic spin Hamiltonian is a key element to obtain a correct picture of the ground and the excited states of magnetic molecules. In this thesis, we are interested in extracting the exchange parameters (Js) from DFT calculations, and we will describe in this section the main methodologies employed in the literature for this purpose. The more broadly used approaches are the local-force method, the magnetic transition state method and the total energy difference method. According to the original scheme [78], using the local-force method it is possible to obtain the exchange parameters by the calculations of the total energy variations of the system corresponding to small spin density perturbation (spin rotations). The local-force method was tested on simple metals Fe, Ni and Ni-Pd alloys providing rather good accuracy in the reproduction of the magnetic parameters. In the magnetic transition-state approach the energy differences between two particular magnetic configurations (ferromagnetic or antiferromagnetic states, for example) is recast in terms of the single-particle energies of a fictitious magnetic transition state defined by a transition-state Hamiltonian [79, 80], obtained as combination of the separated Hamiltonians of the two configurations. While being approximate, the magnetic transition state scheme might have a certain advantage of numerical stability over explicit comparison of large total energy values, needed in the total energy difference method. Moreover, the result is available from a single calculation and offers a microscopical insight of how different orbitals are affected by magnetic interaction, while the information which remains hidden

in the total energy numbers. For all the molecule investigated in this work the total energy difference method was adopted because of its simpler implementation with respect to the previous two methods. Moreover, its suitability for magnetic molecules has been already demonstrated in several cases, e. g. Mn_{12} [81], V_{15} [82, 83], Fe_6 [84].

For the application of this last method, convergence towards the several broken-symmetry (BS) magnetic configurations is needed. In order to achieve this we developed a scheme where intermediated constrained magnetic solutions are obtained by using C-DFT method as implemented by van Voorhis et al. [24, 25]; details on the C-DFT can be found in the previous chapter. The general scheme of the calculation is the following. First, it is helpful to start converging the ferromagnetic, highest-spin, ground state. After that, one reads the converged FM wave functions as initial guesses and the spins on the ions that should attain a negative polarization are constrained by C-DFT to have a negative sign, i.e. the spin is flipped. If there are many spins to be flipped, in order to increase the probability to converge towards the sought magnetic states, it might be more convenient to flip first only a subset of spins attaining a sort of temporary constrained BS state. The procedure is then repeated, until the desired constrained BS state is reached. After having converged the system to a certain constrained spin distribution, i.e. with the desired ions with spin 'up' and spin 'down', the converged C-DFT wavefunctions are themselves read in input as initial guesses, the constraints are removed, and self-consistent electronic convergence is reached within few iterations. Within this scheme, it is possible to obtain whatever spin-multiplicity and spin distribution (BS state) we want, in a computationally rather efficient way, guiding in some sense the system towards the correct BS solution; in fact, it would be otherwise impossible to attain low spin BS states by simply imposing the correct multiplicity of the molecule, because of the intrinsic degeneracy of such states.

When the total energies of the BS states are obtained, J_i values could be extracted by performing total energies differences. In the simplest case, where two magnetic ions with equal spin S are coupled by exchange interaction, there are only two different possible BS states, the ferromagnetic and the antiferromagnetic ones. The energy of the two states, as given by Equation 4.2, are $E_{FM} = -JS^2$ and $E_{AFM} = JS^2$. One can thus extract the value of J from the formula

$$J = \frac{(E_{AFM} - E_{FM})}{2S^2} \tag{4.6}$$

Clearly, if there are more interacting spins, there will be more Js parameter to be determined, and to this aim more BS states must be calculated. As it will be discussed in more detail later, generally there are more possible BS states, i.e. possible equations, from which one can extract the Js, and the system is overdetermined.

It should be noted that, in its standard implementation, the DFT method is a single-determinant method and thus the results are affected by the *spin-contamination error* (SCE) which arises when spin states other then the one with the highest multiplicity are calculated within a BS approach [85, 86]. This error is due to the artificial mixing of different electronic states, and it occurs when an approximate wavefunction is represented in an unrestricted form. In particular, a BS state which is still eigenfunction of the z component of the total spin operator $\mathbf{S}_z$ but not eigenfunction of the total spin squared operator $\mathbf{S}^2$, can formally be expanded in terms of pure spin states of higher multiplicities (the contaminants). Although more accurate calculations like ab initio multideterminantal method would be required to investigate this issue, the systems studied in this thesis are rather large, and the exponential growth of the computational effort of these methods makes them currently impractical. The work of Rudra et al. [86] has shown that the Js extracted from C-DFT states, instead of BS states compare better with the experimental results and the success of these methods is closely linked with the choice of the "fragment" on which the spin constraint is imposed. Unfortunately this method is not well-defined in the case of single-atom bridges (i. e., fluorine bridges in our case). Because of this ambivalence in the fragment definition, we extracted the exchange coupling parameters starting from the converged BS calculations, instead of the C-DFT states which in our case are exploited only as intermediate states used to speed up the convergence towards the BS states.

It is fairly well known in the literature that whenever the B3LYP functional and standard total energy difference methods are used to extract exchange coupling parameters the values inferred from experiments are overestimated by a factor of 2 [15]. This overestimation is primarily connected with the self-interaction error (SIE) present in approximate exchange correlation functionals [25]; since the spatial delocalization of the electrons is overestimated, the electrostatic interaction between the electrons belonging to different atoms is overestimated as well. Very recently an effective *ab initio* scheme to build many-body models for the calculations of magnetic exchange coupling has been presented. This method is based on the construction of many-body Hubbard-like models, using Foster-Boys orbitals as a one electron basis [87]. Although this method seems to provide results very close to the

experimental ones, currently it has been tested only on a small number of molecules(the SMM Fe_4, AFRs Cr_8 and *green*-Cr_7Ni).

4.2. The family of Cr-based antiferromagnetic rings: state of the art

The single units of this family are characterized by a cyclic shape and antiferromagnetic exchange coupling between nearest neighboring metal ions. The main transition metal ion that appears in this family is Cr in its 3+ oxidation state (S=3/2), but other divalent ions are also found. As it has been pointed out by recent works, such molecular rings are very promising candidates for the implementation of quantum logic devices [88], where each magnetic ring represents a qbit. Moreover, recently two or a few more of these rings have been linked together, and dimer, trimers and tetramers have been synthesized. The synthesis of molecular units with tailored different spins has proven to be routine work and a great flexibility in the choice of the linker used to build supramolecular objects have been demonstrated. Many studies have been dedicated also to the need of quantifying the effects of the environment on the magnetic properties of these molecular systems. For instance, successful grafting in ultra-high vacuum condition on surfaces was recently achieved [6, 14, 89–91] in the experimental group of Prof. Marco Affronte in Modena; these studies have demonstrated how the interaction with the substrate does not modify sensibly the magnetic properties of Cr-based molecular rings. In the following, the focus will be on the study of the molecules in the gas phase, i.e. isolated single molecules. We will describe in the next sections the structures of the more prominent molecules (or class of molecules) belonging to this family, shortly revisiting the main results that have been obtained so far by DFT approaches.

4.2.1. The parent Cr_8 molecule

The parent molecule, which could be synthesized with high yield, and from which all the others have been progressively derived, is the antiferromagnetic Cr_8 ring [92] (depicted in Fig. 4.1). This molecule is characterized by a perfect antiferromagnetic coupling between

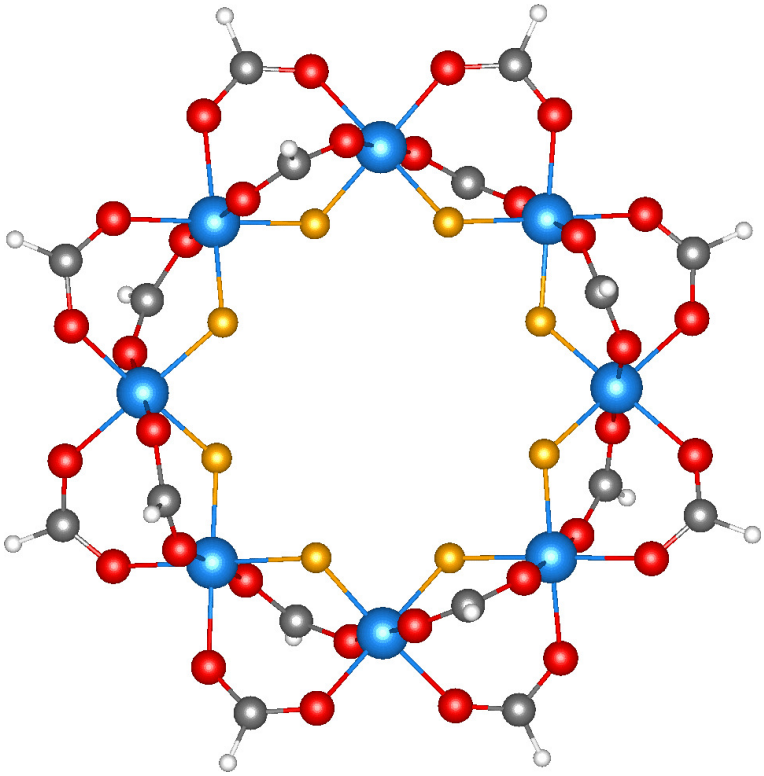

Figure 4.1.: The structure of the Cr_8 molecule, with hydrogen atoms in place of each methyl group Cr/large blue spheres, F/middle orange spheres, C/middle gray spheres, O/middle red spheres, and H/small white spheres.

eight Cr^{3+} ions. This leads to a ground state, at zero field, with total spin S=0 and shows, under applied field, quantum phenomena, such quantum oscillations of total spin [93, 94].

The eight Cr ions, which are placed at an average distance of ∼3.38 Å, are connected with each other via two independent carboxylate (-O-C-O-) bridges and one F bridge, and are arranged in an almost perfect planar octagon. According to the crystal field theory analysis, in octahedral symmetry the d-orbitals split into two sets with an energy difference defined as *crystal-field splitting parameter* ($\Delta_{crystal}$), with d_{xy}, d_{xz} and d_{yz} orbitals lower in energy than the d_{z^2} and $d_{x^2-y^2}$; this is due to the fact that the former group is farther away from the ligands than the latter and therefore experience less repulsion. The three lower-energy orbitals are collectively referred to as t_{2g}, and the two higher-energy orbitals as e_g. The Cr^{3+} ions show the valence configuration [Ar]$3d^3$. These three d electrons occupied the lower-energy t_{2g} orbitals giving a s_z=3/2 [95].

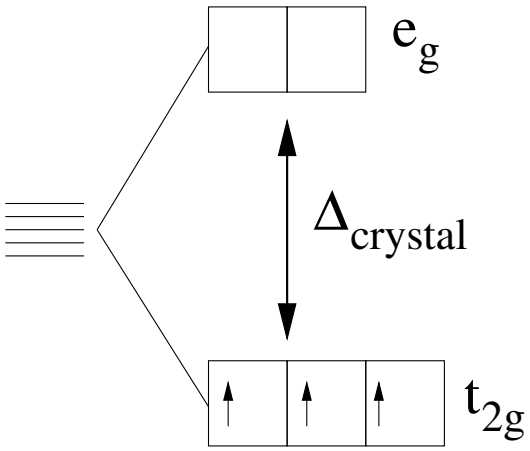

Figure 4.2.: Effect of the octahedral crystal field on Cr^{3+} ion and splitting of the 5 *d*-orbitals

In order to tackle the system with DFT techniques, it is a common practice to "prune" the building block by replacing each methyl molecule CH_3 of the pivalic group with an isovalent H atom, i. e. substituting $C-(CH_3)_3$ with C−H. After the pruning procedure the environment of the magnetic centers is retained and the magnetic moment on the Cr^{3+} ions is unchanged ($\sim 2.7\mu_B$ from DFT calculations [96]). The exact symmetry around all the magnetic centers allows to use just one exchange J_{Cr-Cr} coupling constant to describe the isotropic Heisenberg interactions. For this particular molecule, the spin model Hamiltonian becomes rather simple:

$$E^{TOT} = E_0 - J_{Cr-Cr} \sum_{i}^{7} \mathbf{s}_{z_i} \mathbf{s}_{z_{i+1}} - J_{Cr-Cr} \mathbf{s}_{z_8} \mathbf{s}_{z_1} \tag{4.7}$$

In the theoretical work of Bellini et al. [96], the exchange couplings have been extracted by total energy difference method. Calculating the total energy difference between FM state (S_z=12) and the AFM (S_z=0), and after some straightforward algebra, we obtain the formula

$$J_{Cr-Cr} = \frac{4}{9} \frac{[E^{TOT}_{AFM} - E^{TOT}_{FM}]}{16} \tag{4.8}$$

The results clearly indicates that the generalized gradient local approximation (GGA) in the version proposed by Perdew et al. [44] fails to reproduce the exchange experimental parameters (J^{GGA}_{Cr-Cr}= -5.8 meV versus $J^{Exp.}_{Cr-Cr}$= -1.5 meV [92]). The value of J can be corrected considering additional on-site correlation terms (GGA+U) [78] in the Cr d orbitals. In fact, Cr is coordinated with O and F atoms, and it is well known that in transition metal oxides both electronic and magnetic properties are badly described within mean field approximations. Supposing a value of U=2.7 meV , the agreement with the experimental results improves sensibly (J^{GGA+U}_{Cr-Cr} = -2.1 meV).

4.2.2. Green-Cr_7M (M = divalent cation, e.g. Ni) rings

In 2003, Dr. G. Timco in the group of Prof. R. E. P. Winpenny of the University of Manchester, varying the experimental conditions, as well as the components of the synthetic reaction, produced an heterometallic molecular ring from Cr_8, substituting one of the Cr^{3+} with a Ni^{2+} [2]. Such substitution leads to a breaking of the compensation of the spins and modifies the total spin of the AF ring. The derivative Cr_7Ni (named *green* after the color of the molecular crystal) is isostructural to the Cr_8, and two pivalate and one fluorine bridging ligands connect each metal pair, as it happens for the homometallic parent molecule. The substitution of one Cr^{3+} with one Ni^{2+} leads to an imbalance of the charge in the ring of one formal negative charge -*e*. In order to separate and stabilize the molecule, the ring is counterbalanced by a cation, an amino chain with different possible lengths, placed in the middle of the ring (see Fig. 4.3); this cation interacts with two fluorine atoms through three NH...F hydrogen bonds. Different experimental techniques as specific heat, torque magnetometry [97], neutron scattering [29], and micro-SQUID magnetization at very low temperature [98] have been employed and the results were fitted using a spin model Hamiltonian [93]. An S=1/2 ground state doublet well separated from the first excited state (S=3/2) was found and a time of coherence of about 3 μs at 2 K [16] have been observed. This is several order of magnitude longer than the typical time needed for spin manipulation, making it a very good candidate of a molecular qubit [97]. After Cr_7Ni, other members of the *green* derivative have been synthesized with success, substituting a Cr trivalent ions with divalent nonmagnetic and paramagnetic ions, and a whole series of heterometallic *green* rings with the general formula $[NH_2Et_2][Cr_7MF_8(O_2CCMe_3)_{16}]$ (where M = Ni^{2+}, Mn^{2+}, Zn^{2+}, Cu^{2+} and Fe^{2+}) has been engineered.

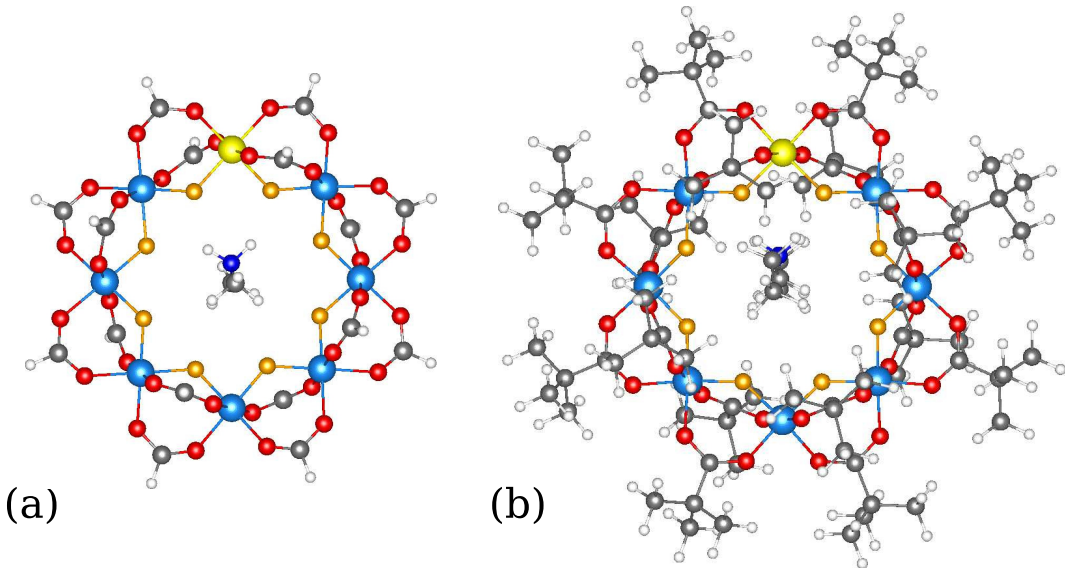

Figure 4.3.: The structures of the *green*-Cr_7M class, (a) the *pruned*-version with hydrogen atoms in place of each methyl molecule CH_3 groups, and (b) the full-version con all the pivalic groups and the whole amino chain in the center. In both the figures atoms colors are as follow Cr/large blue spheres, F/middle orange spheres, C/middle gray spheres, O/middle red spheres, N/middle dark blue spheres and H/small white spheres.

As for Cr_8, also for the *green* substituted rings it is possible to build a spin Hamiltonian to describe their magnetic properties, and the energy is given by

$$E^{TOT} = E_0 - J_{Cr-Cr} \sum_{i}^{6} \mathbf{s}_{z_i}^{Cr} \mathbf{s}_{z_{i+1}}^{Cr} - J_{Cr-M} (\mathbf{s}_{z_7}^{Cr} \mathbf{s}_{z_8}^{M} + \mathbf{s}_{z_8}^{M} \mathbf{s}_{z_1}^{Cr}) \tag{4.9}$$

where the, otherwise implicit, electronic contribution to the total energy E_0 is indicated. Whereas nominal spins are known for each metallic species ($\mathbf{s}_z$ = 3/2, 1, 5/2, 0, 1/2, 2 respectively for Cr^{3+}, Ni^{2+}, Mn^{2+}, Zn^{2+}, Cu^{2+} and Fe^{2+}), just two different exchange parameters are sufficient (J_{Cr-Cr} and J_{Cr-M}) to describe the Heisenberg interaction in these molecules. In Ref. [15], DFT calculations have been performed for Cr_7M, with M = magnetic divalent ion, pruning, as for Cr_8, the peripheral ligands but retaining the cationic alkyl chain inside the ring. In alternative the calculation could have been carried out in the absence of the alkyl chain provided that an extra electron was added in the simulation cell; in this case, additional degrees of freedom enter in the calculation, complicating the

analysis. In Sec. 4.3.1 it will be shown that if one performs a DFT calculation of the pristine molecules, keeping the whole peripheral pivalic ligands, the exchange interactions between the magnetic ions are only mildly improved with respect the ones obtained for the "pruned" molecules, when comparing with experiments. This is a demonstration that the "pruning" technique is quite robust, and it is not the main responsible for the poor agreement (for some choice of M) between theory and experiments.

4.2.3. Purple-Cr_7Ni rings

Another derivative of the Cr_7Ni molecule has been produced from the group of Prof. Winpenny in Manchester [1], called *purple*-Cr_7Ni (again, after color of the molecular crystal) with formula Cr_7NiF_3 $(C_8H_{14}NO_5)$ $(O_2CCMe_3)_{15}(H_2O)$. Compared to the *green* rings in this molecule, five out of eight fluorine bridges are replaced by N-ethyl-d-glucamine ($C_8H_{14}NO_5H_5$). There is an imbalance in the charge due to the direct coordination of one of the Cr ion with the N atom of the glucamine, and as a net effect, no cation is needed to counterbalance the molecule.

Because of the replacement of some of the fluorine atoms by a glucamine, there are in principle different Cr-Cr and Cr-Ni exchange interactions in the ring. Notwithstanding this large modification, the magnetic interactions between the Cr-Cr and Cr-Ni paramagnetic ions, as extracted from a temperature-dependent susceptibility analysis [18], have been found to be only slightly larger to the ones observed in *green*-Cr_7Ni ($J_{Cr-Ni} = J_{Cr-Cr} = -2.0$meV). Similarly in Ref. [15] only two different Js have been considered for practical purposes, to match the experimental assumption, and Js have been extracted from total energy difference analysis ($J_{Cr-Ni} = -2.0$ meV and $J_{Cr-Cr} = 3.9$ meV). We will extend in Sec. 4.3.2 the DFT analysis of the *purple*-Cr_7Ni, accounting for different Js, and trying to understand if all the Js or, for instance, only the ones where the glucamine replaces the fluorine bridges, are subject to this increase.

4.2.4. Supramolecular dimers

The most important feature of the *purple* derivative is that one of the Ni coordination positions is free for a neutral terminal ligand (the reaction chemistry supports the assumption that the terminal ligand is a water molecule). It has been experimentally showed that is

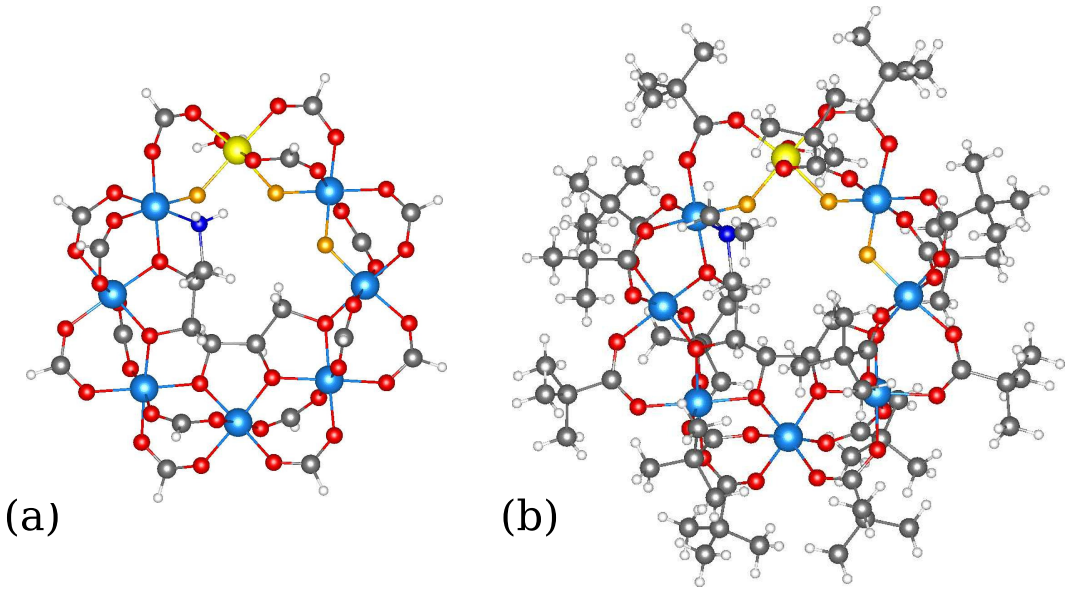

Figure 4.4.: The structures of the *purple*-Cr_7Ni, (a) the *pruned*-version with hydrogen atoms in place of each methyl molecule CH_3 groups, and (b) the full-version con all the pivalic groups and the whole N-ethyl-d-glucamine in the center. In both the figures atoms colors are as follow Cr/large blue spheres, F/middle orange spheres, C/middle gray spheres, O/middle red spheres, N/middle dark blue spheres and H/small white spheres.

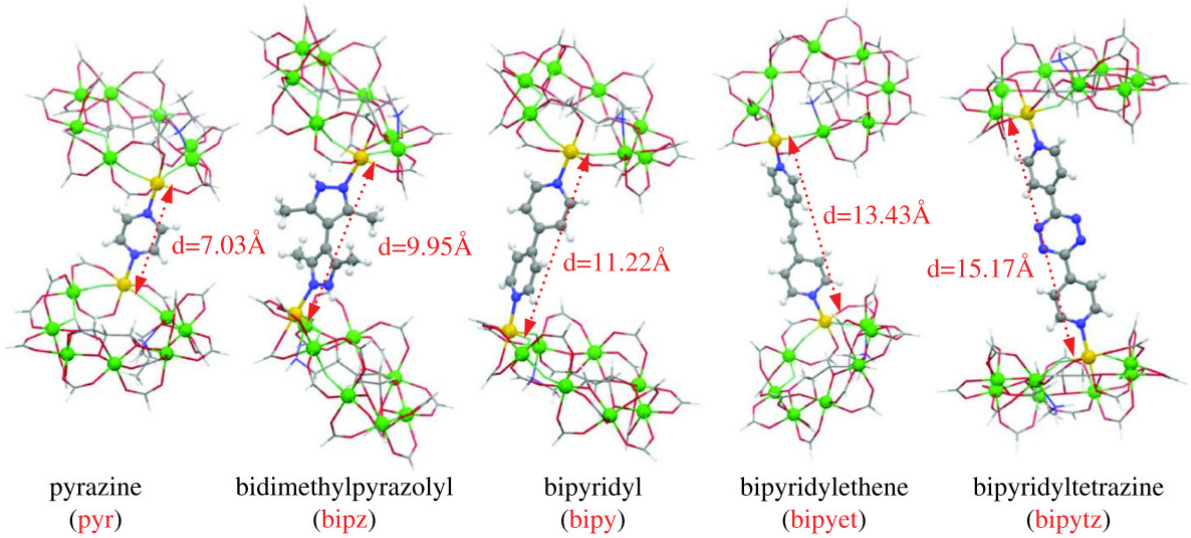

Figure 4.5.: The molecular structures of Cr_7Ni purple dimers with different organic bridges (pyr, bipz, bipy, bipyet, and bipytz) with the inter-rings through-space Ni-Ni distances (d) for each dimer. (Reproduced from Ref. [17]

possible to exchange the water molecule with neutral pyridine-based ligands, opening up the possibility of synthesizing novel ring dimers and oligomers [1]. Several studies have then been dedicated to study how to bind two or more *green*-Cr_7Ni rings without altering the properties of the single rings, in order to realize two-qbit devices. Interestingly molecular spin dimers represent a testing ground also for what concerns the study of entanglement. Additionally, the study of supramolecular dimers is of great interest because it allows a deep investigation of the efficiency of spin's propagation through organic bonds. Although exchange interactions, stemming from direct overlapping of nearest neighboring metal orbitals, as well as superexchange, mediated by the orbitals of bridging on distance of one or two atoms, are mechanisms which had been studied in detail both experimentally and theoretically, a recent article has shed light on spin interactions between metal centers through long organic groups [17] in a series of *purple*-Cr_7Ni - L - *purple*-Cr_7Ni dimers, with L = organic linker.

Usually the building block which acts as linker is chosen among the aromatic rings family. This class of compounds has specific characteristics, i.e. (i) coplanar structure, with all the contributing atoms in the same plane, (ii) largely delocalized π-molecular orbital formed by overlap of atomic p-orbitals above and below the plane of the ring. The progenitor of this class is benzene, formed by a ring of six C, but several heteroaromatic compounds

can be built inserting in the ring one or more different atoms (N, O, S). Dimers composed by two *purple*-Cr_7Ni rings have been synthesized (see Fig. 4.5), systematically changing the aromatic linker (pyrazine (pyr, in short), bidimethylpyrazolyl (bipz), $4,4'$-bipyridyl (bipy), trans-1, 2-bipyridylethene (bipyet), and bipyridyltetrazine (bipytz)), thus tuning the strength of the magnetic interaction. Their behavior was rationalized by density-functional theory calculations, low temperature micro-SQUID and specific heat measurements. Low temperature specific heat $C(T, H)$ data suggested that the pattern of the lowest lying states of the single ring is preserved also in supramolecular systems, while micro-SQUID analysis was able to provide a more quantitative estimate of the exchange coupling between the two S=1/2 of the two rings. The trend in the experimental J values as a function of the linker is nicely reproduced in the calculation. Moreover, in that work some general empirical rules about the strength of the interaction between units linked by an aromatic bridge [99] have been verified; namely i) the larger the number of bonds which compose the interaction path, the smaller the interaction is, ii) charge and spin polarization induced by bonding to a metal site proceed in an alternating fashion in aromatic bridges, iii) since a magnetic interaction can be sustained by different bond paths in the linker, the strength of the interaction depends on whether quantum constructive or destructive interference between paths with different lengths arise [100]. Especially point iii) reinforces the hypothesis that the spin-polarization mechanism involves hopping of electrons in the π orbitals at the atom sites of the conjugated system as much as electron transfer, which is directly related to the π-π orbital overlap throughout the linker.

Exploiting the expertise maturated on these molecules, we will discuss in Section 4.3.3 a new class, recently synthesized, of supramolecular dimers, where one *purple* and one *green* ring are linked by a pyridine molecule. Here instead of varying the bridging ligand, chemical synthesis was able to substitute different divalent ions in both the rings; similarly to *purple-purple* dimers. We will provide a quantification by DFT total energy calculations of the magnetic coupling between the magnetic ions belonging to different rings through the pyridine linker.

4.3. Results

The results presented in the following have been obtained employing the NWChem quantum chemistry package [23]. In order to account for the electronic correlations in these transition

metal complexes, we used the B3LYP hybrid exchange-correlation functional [101]. Ahlrichs valence triple-ζ(VTZ) basis set for the transition metal ions and Ahlrichs valence double-ζ (VDZ) basis set for the rest of the elements have been considered. Broken-symmetry (BS) magnetic configurations were obtained using C-DFT. More detail on the calculations can be found in Sec. 3.2. We will first discuss some test calculations on the *green*-Cr_7M AFRs, in order to countercheck the "pruning" procedure that has been adopted so far in the literature. After that, the extraction of the exchange interaction parameters in *purple*-Cr_7Ni AFR will be presented. In the last section, we give a comprehensive analysis of the magnetic couplings in *purple-green* supramolecular dimers.

4.3.1. Green-Cr_7M rings

An extensive theoretical investigation of the *green*-Cr_7M class has been done recently [15], considering the "*pruned*" structures of such molecules (see Fig. 4.3(a)). Here, we are interested in performing DFT calculations for the intact structures (see Fig. 4.3(b)) of the same molecules. Our aim is to understand if such pruning technique, which is routinely done to limit the computational effort, shows some flaws. The main question is clearly if this structural approximation induce some modifications on the charge and spin distribution of the bridging ligands, i.e. the F and the O-C-O bridges, that mediate the exchange coupling between the magnetic ions. Four different substituted rings, i.e. *green*-Cr_7M, with M= Ni^{2+}, Mn^{2+}, Fe^{2+} and Cu^{2+}, have been considered. In Tab. 4.1 a comparison between the exchange parameters extracted from the calculations of the whole structures, the ones extracted for the *pruned* structures [15] and the values extracted in the experiments are listed.

We observe that the agreement with the experiments is not impressively improved by considering the pristine structures as compared to the "*pruned*" structures. Yet some variations are found and we can extrapolate in the following some trends. First, in the pristine structures the exchange parameters which quantify the coupling between two Cr ions are less negative than in the pruned ones, i.e. the AFM coupling is smaller, in better agreement with experiment. Secondly for all the AFRs except Cr_7Fe, the ratio between J_{Cr-M} and J_{Cr-Cr} is closer to one for the pristine structures, similarly to what is found in experiments. Another point which is worth to mention is the larger (and of different sign) variations observed for J_{Cr-M} as compared to J_{Cr-Cr}. The substitution of an H

Table 4.1.: Comparison among exchange parameters (in meV) for *green*-Cr_7M, M = Ni, Mn, Fe and Cu. Obtained from DFT calculations of *pruned*-versions (first column), full-version (second column) and experimentally

	theory pruned			theory full		exp		
M atom	J_{Cr-M}	J_{Cr-Cr}	ref.	J_{Cr-M}	J_{Cr-Cr}	J_{Cr-M}	J_{Cr-Cr}	ref.
Ni	−0.5	−3.3	[15]	−1.2	−2.9	−1.7	−1.5	[29]
						−1.3	−1.4	[30]
Mn	−1.3	−3.3	[15]	−2.0	−2.6	−1.4	−1.5	[29]
Fe	−2.2	−3.3	[15]	−0.7	−2.9	−1.1	−1.1	[31]
						−0.8	−1.5	[30]
Cu	1.7	−3.3	[15]	0.1	−2.6	−1.6	−1.5	[102]
						−1.5	−1.5	[30]

atom in the place of a $C(CH_3)_3$ introduces a small change in the electronic distribution in the O-C-O bridge. Utilizing a more "chemical" language, the pK_a (which is related to the acidity constant K_a by the formula, $pK_a = -log_{10}K_a$) of the formic acid H_2CO_2 is lower than the one of the pivalic acid $(CH_3)_3CCOOH$, i.e. 3.77 and 5.03 respectively. The lower the pK_a, the more acid the molecule is, which means that it decomposes more easily releasing a proton H^+. On the other hand the decomposition is related to how many electrons are localized on the oxygen atoms: less electrons favor the decomposition, since the H atom would have more charge than it pleases. To summarize, replacing the pivalic groups present in the pristine ring with formic groups (that is, pruning the structure replacing the $C(CH_3)_3$ fragment with H atoms) leads to a larger localization of the electrons in the O atoms belonging to the carboxylic group, i.e. the O atoms of the bridge. If the exchange interactions between two Cr atoms are in average around 0.5 meV smaller (less antiferromagnetic) for the pristine molecule as compared to the pruned ones, the exchange coupling between Cr and the M divalent substituting ions are in average 1.1 meV larger (more antiferromagnetic).

If we do not find any straightforward argument for the different sign, the large sensitivity in absolute values of J_{Cr-M} upon electronic/structural modification in the bridges as compared to J_{Cr-Cr} has been already postulated in a combined experimental and theoretical work published by the Modena group [14]. In this paper, a change in sign in the Ni XMCD signal from *green*-Cr_7Ni rings, when moving from a bulk sample to a monolayer grafted on

Au(111) by liquid phase deposition, has been explained by an alteration of the exchange interaction between Cr and Ni due to a "breathing" (structural expansion of a few %) of the molecule, since upon adsorption the tight packing between the molecules present in the crystal is relieved.

4.3.2. Purple-Cr_7Ni rings

The *purple*-Cr_7Ni, in its pruned version (see Figure 4.4(a)), has been characterized by DFT calculations [15], and by specific heat and susceptibility measurements [103]. In these works, as done for the *green* derivative, only two different exchange parameters, i.e. J_{Cr-Cr} and J_{Cr-Ni} have been assumed in the spin model Heisenberg Hamiltonian, and values of J_{Cr-Ni} = J_{Cr-Cr} = 1.9 meV, and J_{Cr-Ni} = 2.0 meV and J_{Cr-Cr} = 3.9 meV have been obtained, respectively from theory and experiments. As compared to the *green*-Cr_7Ni derivative, magnetic couplings are larger (more antiferromagnetic). Because of the asymmetry in the bridges induced by the presence of the glucamine, the *purple*-Cr_7Ni represents an interesting play ground for a deeper comprehension of the exchange parameters.

In fact, after a close inspection of the molecular structure, it is possible to identify four different types of connections between the magnetic centers (see Fig. 4.6), namely:

(a) $J_{Cr-Ni(1)}$ associated to one Cr-Ni interaction mediated by a carboxylate ligand and a fluorine bridge;

(b) $J_{Cr-Ni(2)}$ associated to one Cr-Ni interaction mediated by two carboxylate ligands and a fluorine bridge;

(c) $J_{Cr-Cr(1)}$ associated to one Cr-Cr interaction mediated by two carboxylate ligands and a fluorine bridge;

(d) $J_{Cr-Cr(2)}$ associated to five Cr-Cr interactions mediated by two carboxylate ligands and a oxygen bridge (which belongs to the glucamine);

This "four Js" spin model Hamiltonian becomes then,

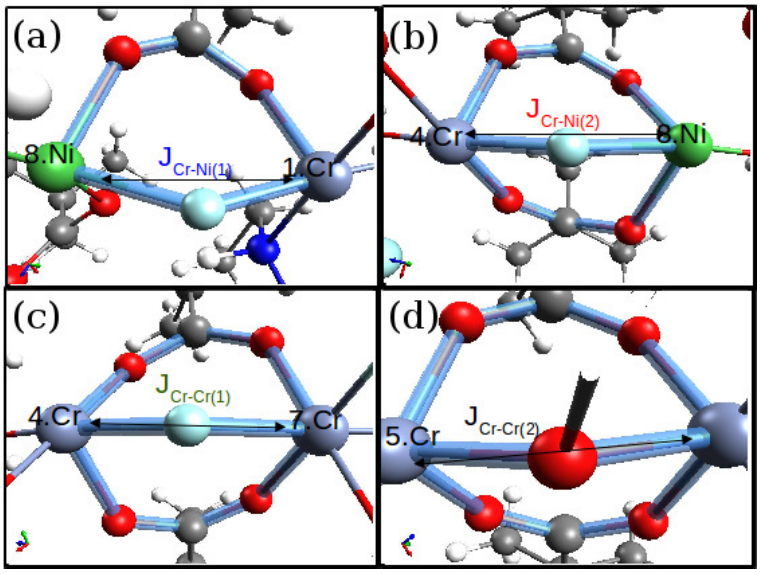

Figure 4.6.: The four different types of connections in *purple*-Cr_7Ni, $J_{Cr-Ni(1)}$ (a), $J_{Cr-Ni(2)}$ (b), $J_{Cr-Cr(1)}$ (c) and $J_{Cr-Cr(2)}$ (d)

$$\begin{aligned} E^{TOT} =& E_0 - J_{Cr-Ni(1)}(\mathbf{s}^{Cr}_{z_1}\mathbf{s}^{Ni}_{z_8}) - J_{Cr-Ni(2)}(\mathbf{s}^{Cr}_{z_4}\mathbf{s}^{Ni}_{z_8}) - J_{Cr-Cr(1)}(\mathbf{s}^{Cr}_{z_4}\mathbf{s}^{Cr}_{z_7}) + \\ & - J_{Cr-Cr(1)}(\mathbf{s}^{Cr}_{z_7}\mathbf{s}^{Cr}_{z_3} + \mathbf{s}^{Cr}_{z_3}\mathbf{s}^{Cr}_{z_6} + \mathbf{s}^{Cr}_{z_6}\mathbf{s}^{Cr}_{z_2} + \mathbf{s}^{Cr}_{z_2}\mathbf{s}^{Cr}_{z_5} + \mathbf{s}^{Cr}_{z_5}\mathbf{s}^{Cr}_{z_1}) \end{aligned} \tag{4.10}$$

Although many types of exchange interactions have been studied in detail, both experimentally and theoretically as the direct overlapping of nearest neighboring metal orbitals or the superexchange mediated by the bridging orbitals (oxygen or fluorine atoms, for example) [104], the *purple*-Cr_7Ni offers the peculiar opportunity to investigate the effect of an additional carboxylate ligand, $J_{Cr-Ni(2)}$ vs. $J_{Cr-Ni(1)}$, and the effect of the replacement of a fluorine bridge by an oxygen bridge, $J_{Cr-Cr(2)}$ vs. $J_{Cr-Cr(1)}$, in the very same molecule.

To find the four exchange parameters it is then necessary to solve a system of four linear equations (five if we consider also the E_0 energy). It is easy to realize that several different BS states are possible and, as before, the exchange parameters are overdetermined. The work of Bencini et al. [85] clearly evidenced that for molecular magnets, the computed exchange couplings extracted by DFT calculations may vary depending on the BS states chosen to extract them. They used a complete set of BS determinants to compute the exchange coupling constants of a three− and four−spin system averaging on all the total energy differences available. In principle, this method could be used also for our systems.

Unfortunately, since we have eight inequivalent magnetic ions that would require the calculation of $\frac{2^8}{2} = 128$ different BS states (the factor two indicates that half of them can be obtained just reversing all the spins). Such calculations would require a large amount of computational resources considering also all the difficulties described in Appendix A to achieve the correct BS state, without mentioning that this method does not lead, however, in some cases a considerable improvement. In order to reduce the spin contamination error in the exchange parameters within a reasonable computational effort, we have chosen, among all the possible states, only the ones with high spin because they have smaller spin contamination, as compared to BS solutions with lower spin.

In Figure 4.7 are represented three of the nine BS configurations used in our calculations [1].

Table 4.2.: List of the broken symmetry configurations of the *purple* rings used to extract the exchange constants, with the relative Total Spin (S) of each state.

Label	spin (−) atoms	S
HS	all spin (+)	23/2
LS1	1,2	11/2
LS2	1,4	11/2
LS3	4,8	13/2
LS4	2,8	13/2
LS5	2	17/2
LS6	4	17/2
LS7	8	19/2
LS8	1	17/2

To further minimize the spin-contamination errors we calculated the total energies of all the possibles BS states and then we averaged over all the $9!/(9-5)!5! = 126$ subsystems chosen to solve the Hamiltonian equation. In Table 4.3 the exchange parameters obtained as solutions of a specific subgroup of BS states and the averaged results on all the 126 possible subgroups are listed.

[1] It should be noted that although in Figure 4.7 were depicted the pruned versions of the purple rings for clarity, all the DFT calculations have been made with the full version of these molecules (complete pivalic groups).

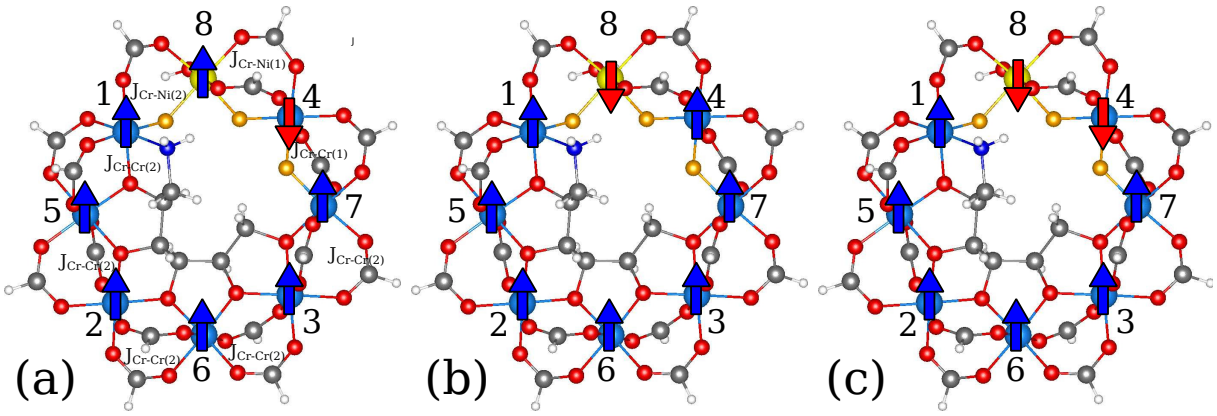

Figure 4.7.: Schematic representations of three different BS states (a) LS6, (b) LS7, (c) LS3.

Table 4.3.: Comparison among exchange parameters (in meV) for *purple*-Cr_7Ni. Obtained from DFT calculations of several BS subgroups

	$J_{Cr-Ni(1)}$	$J_{Cr-Ni(2)}$	$J_{Cr-Cr(1)}$	$J_{Cr-Cr(2)}$
HS, LS1, LS2, LS3, LS4	−2.8	−4.4	−3.0	−4.4
HS, LS5, LS6, LS7, LS8	−3.2	−4.2	−2.9	−4.3
mean value on HS, LS1, LS2, LS3, LS4, LS5	−3.0	−4.4	−2.9	−4.3
mean value on all higher spin states	−3.0	−4.3	−2.8	−4.3

The results of Table 4.3 shows that the Js found for the *purple*-Cr_7Ni are only marginally affected by the subgroup of the BS states chosen for the solution of the linear system. The values of the two exchange parameters $J_{Cr-Ni(1)} = -3.0$ meV and $J_{Cr-Ni(2)} = -4.3$ meV show how an increase in the number of carboxylate bridges enhances, as expected, the magnetic coupling. In addition the comparison between $J_{Cr-Cr(1)} = -2.8$ meV and $J_{Cr-Cr(2)} = -4.3$ meV shows that the p-character orbitals of a O^- (part of the glucamine) allow more efficient spin communication between the two ionic spins, as compared to the F^-; this is likely due the larger spacial extension of the p orbital and, consequently, the larger overlap with the d-orbitals of the Cr^{3+} ions. If we average the Js for the Cr-Ni and Cr-Cr interactions (considering also how many times they appear in the ring), we obtain $J^{av}_{Cr-Ni} = -3.65$ meV and $J^{av}_{Cr-Cr} = -4.05$ meV , to be compared with the values $J_{Cr-Ni} = -2.0$ meV and $J_{Cr-Cr} = 3.9$ meV obtained for the pruned structure, and with a simplified "two Js" model Hamiltonian [15]. If the value of the exchange interaction between the Cr atoms is very similar in the two cases, the one between Cr an Ni ions is sensibly different; the averaged values calculated here are now more similar to each other, in agreement with the experimental evidence (despite the overestimation of a factor of two, which is always present due to the missing correlation effects).

4.3.3. Purple-Cr_7M/pyr/Green-Cr_7M' supramolecular dimers

Recently the research group of Prof. Winpenny in Manchester has worked on another interesting class of dimers labeled *purple-green* with the general formula $[NH_2Et_2]$ $[Cr_7\mathbf{M}F_3(C_8H_{14}NO_5)(O_2CCMe_3)_{15}C_5H_4NCO_2Cr_7\mathbf{M}'F_8(O_2CCMe_3)_{15}]$ (briefly *purple*-$Cr_7\mathbf{M}$-pyr-*green*-$Cr_7\mathbf{M}'$ with $\mathbf{M}, \mathbf{M}' = Ni^{2+}$, Mn^{2+}, Zn^{2+} , and pyr = pyridine). From now on, for clarity, we indicate with M the substituting metal ion belonging to the *purple* ring and with M' the one belonging to the *green* ring. Observing 4.8, where the structure of the *purple*-Cr_7Ni-pyr-*green*-Cr_7Ni is depicted, we note that the N atom of the pyrimidine group inside INA is able to complex the metal atom in the free position M of the *purple* ring, while the carboxyl group can perfectly fit inside the *green* ring connecting two of the eight metal atom, Moreover, the M ion in the *purple* ring is connected to the M' ion and one Cr ion in the *green* ring through a isonicotinic acid molecule (C_5H_4NCOOH also know as INA). Thus, magnetic communication through the INA bridge between the spins of three different metal ions is active in this class of dimers. In the following, several combinations of M and M' metals on the two rings have been characterized, with the aim to shed light onto the multiple

exchange pathways hosted by INA bridge. Moreover we have the possibility to compare our results with specific heat experiments [103].

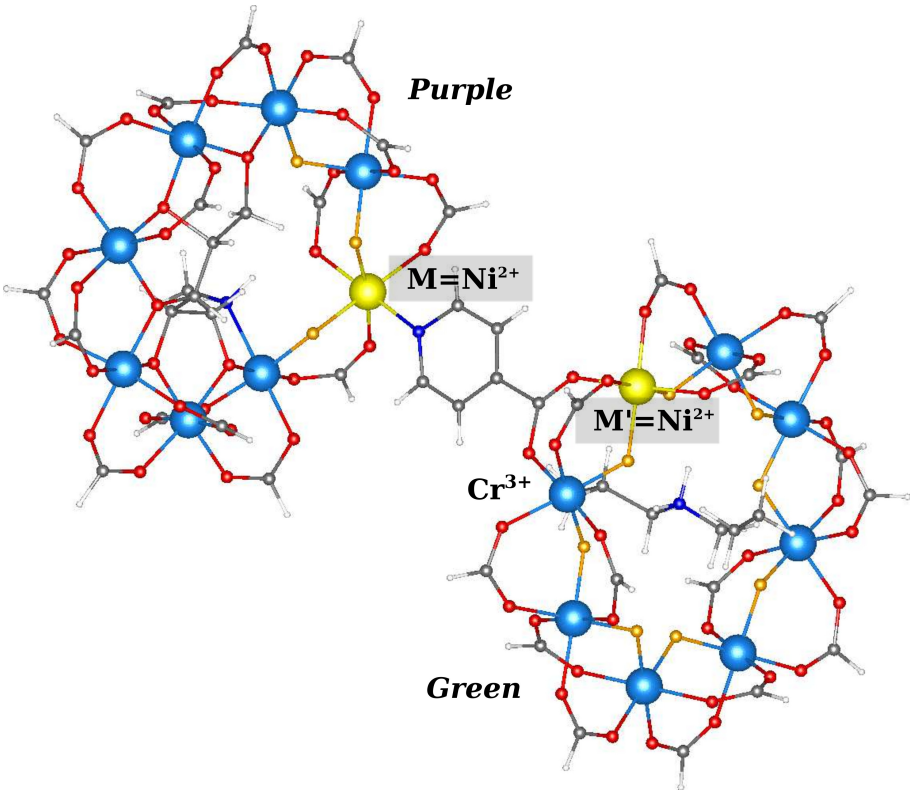

Figure 4.8.: Crystallographic structure of *purple*-Cr_7Ni/pyr/*green*-Cr_7Ni obtained from X-ray diffraction (private communication). The atoms colors are as follow Cr/large blue spheres, Ni/large yellow spheres, F/small orange spheres, C/small gray spheres, O/small red spheres, N/small dark blue spheres and H/small white spheres.

By looking at Fig. 4.9, where the spin density in the bridge region is plotted for the M = M' = Ni dimer, we note the same alternation mechanism , i.e. a change in sign, in the spin polarization when moving from one atom to the next, following bond paths, observed in the *purple-purple* dimers case.

As a first approximation, the total macroscopic ring-ring exchange coupling was traced back to the sum of two main microscopic contributions, the $M-M'$ and $M-Cr^{3+}$ magnetic couplings; thus, the spin model Hamiltonian (Eq. 4.11) reads,

$$E = E_0 - J_{M-Cr}\mathbf{s}_z^M\mathbf{s}_z^{Cr} - J_{M-M'}\mathbf{s}_z^M\mathbf{s}_z^{M'} \tag{4.11}$$

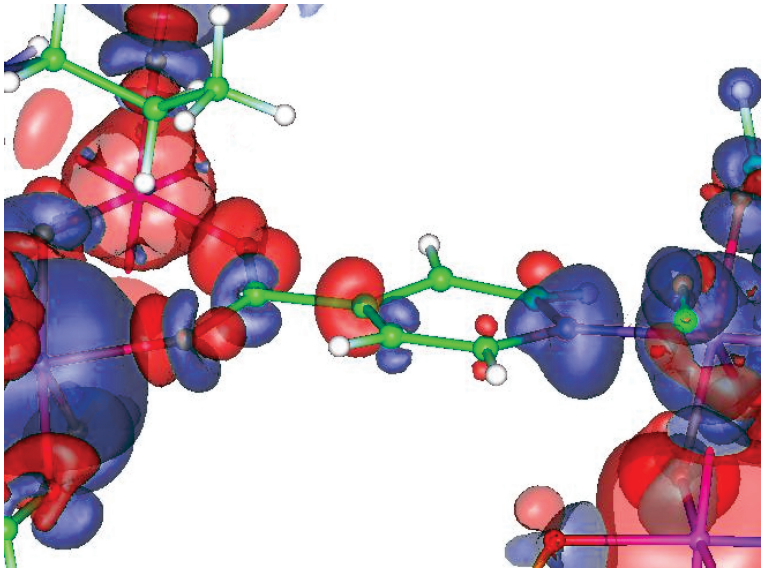

Figure 4.9.: Spin-polarization density in *purple*-Cr_7Ni/pyr/*green*-Cr_7Ni in the AFM configuration, zoomed in the region of the linker, for isovalues of + (blue) and − (red) 0.0005 electrons/a.u.^{3}

where the Js are the inter-ring exchange parameters, and the various s_z are the spin moments of the three frontier ions (see Figure 4.8).

If we want to extract from BS state total energy calculations the microscopic exchange parameters responsible for the coupling of the two rings, we need to tackle the issue of a simultaneous three spin centers interaction. Since inter-ring couplings are expected to be order of magnitude smaller than intra-ring couplings, and since uncertainties in the extraction of the latter risk to spoil the information needed to extract the former, care has to be taken when choosing the BS states. Namely, BS states where the AFM coupling between the ions within the same ring is broken were not included in the calculations, because additional intra-ring exchange parameters would have necessarily to be included in the Hamiltonian. In order to solve the problem we instead postulated that the two microscopic interaction $M - M'$ and $M - Cr^{3+}$ could be considered, in first approximation, independent from each other, i.e. if the M' is substituted with a different divalent ion, the interaction between M and Cr^{3+} remains unaltered. Accordingly, the interaction $M - M'$ was turned off in an intermediate calculation, substituting the M' ion on the green ring with a Zn^{2+} (s=0) non magnetic ion. In this way it was possible to simplify the equation 4.11 and obtain the value of J_{M-Cr}. Once J_{M-Cr} is known, it is inserted in the original Hamiltonian, and by performing the usual total energy difference between the AFM and

the FM states, it is possible to determine the $J_{M-M'}$ exchange coupling. A more detailed description of this procedure applied on a test case is available in Appendix A

The results obtained for the different choices of M and M' are summarized in Table 4.4.

Table 4.4.: Inter-ring Exchange Interaction Parameters (in meV); Total Spin S and energy difference (in meV) for the Antiferromagnetic (AFM) ground state and the first Ferromagnetic excited state (FM) for several members of the *purple*-$Cr_7\mathbf{M}$/pyr/*green*-$Cr_7\mathbf{M'}$ class

dimer	**M**	**M'**	$J_{\mathbf{M}-Cr}$	$J_{\mathbf{M}-\mathbf{M'}}$	S_{AFM}	S_{FM}	$E_{AFM} - E_{FM}$
1	Zn	Ni	0.00	0.00	1	2	0.00
2	Ni	Zn	0.06	0.00	1	2	−0.18
3	Ni	Ni	0.06	−0.05	0	1	−0.27
4	Ni	Mn	0.06	0.10	1/2	3/2	−0.30
5	Mn	Zn	−0.08	0.00	1/2	5/2	−0.58
6	Mn	Ni	−0.08	0.07	1/2	3/2	−0.92

The total energy differences reported in the last column of Table 4.4 show that in all the dimers the low spin state is always energetically favored respect to the high spin one. The inter-ring exchange parameters found for this class of dimers were not always antiferromagnetic ($J < 0$) as it happens in *purple-purple* dimers (see Section 4.2.4) but they can be ferromagnetic as well. The inter-ring Js are more than an one order of magnitude smaller than the intra-ring Js, shown for the single rings in the previous Sections 4.3.1 and 4.3.2, never exceeding 0.10 meV.

First we can notice, comparing the FM - AFM energy differences in dimers 1 (M=Zn, M'=Ni) and 2 (M=Ni, M'=Zn), the dramatic effect of the Zn^{2+} in the spin communication. Interestingly, when the Zn^{2+} ion is substituted in the purple ring (dimer 1) magnetic communication between the two rings is completely suppressed, and FM and AFM solutions become degenerate (within 0.01 meV). The spin-polarized density for this dimer (see Fig. 4.10 (a)) zoomed-in in the region of the linker clearly show this effect, i.e. spin polarization in the pyridine ring is barely visible. On the contrary, when the Zn^{2+} ion is substituted in the green ring (dimer 2) the AFM coupling is preferred over the FM one by −0.18 meV. This is visible also in Fig. 4.10 (b) where the presence of an alternating polarization of the

π orbitals in the pyridine linker demonstrate how there is an active spin-path between the Cr^{3+} in the *green* ring and the Ni^{2+} ion in the *purple* ring.

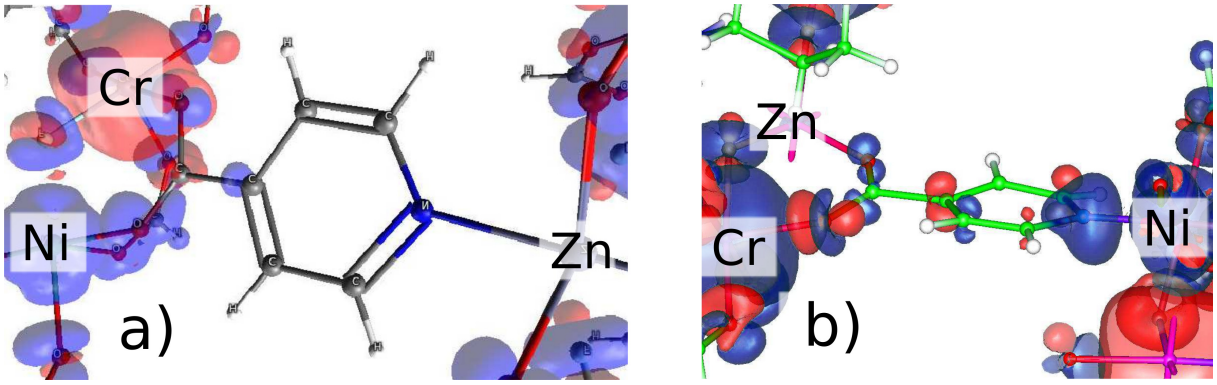

Figure 4.10.: Spin-polarization density in (a) *purple*-Cr_7Zn/pyr/*green*-Cr_7Ni (dimer 1) and (b) *purple*-Cr_7Ni/pyr/*green*-Cr_7Zn (dimer 2), both in the AFM configuration, zoomed in the region of the linker, for isovalues of + (blue) and − (red) 0.0005 electrons/a.u.^{3}

If we perform a similar permutation, placing Ni^{2+} in the *purple* ring and Mn^{2+} in the *green* ring (dimer 4) or viceversa (dimer 6) again a considerable variation in the AFM-FM energy difference, i.e. 0.30 meV for dimer 4 and 0.92 meV for dimer 6, is observed. Moreover, a direct comparison of the spin-polarization density for the two cases (see Fig. 4.11) confirms a considerable increase in the π-orbitals delocalization in the linker moving from dimer 4 to dimer 6. From the accurate analysis of the spin-polarized electron density in the carboxylate group belonging to the INA bridge in Figures 4.10 and 4.11, a sort of competition emerges between the two metallic ions placed on the *green* ring of the dimer: the atom with the largest absolute value of the spin imposes his own spin alternation along the carboxylate bridge up to the first C atom of the pyridine ring. The theoretical work on the *purple-purple* dimers [17] has already shown the spin alteration of the pyridine ring is mainly due to the spin moment of the divalent ion of the *purple* ring. The seminal paper of Bencini et al. [105] showed that this effect, in reality, could be traced back to the different hybridization of the $4s$ and $3d$ orbitals of the metallic ion with the $2p$ orbitals of the O and N involved. In particular, for a given interatomic metal-ligand distance the relative orientation of the half-filled $3d$ orbitals respect to the $2p$ orbitals severely affects the exchange coupling parameters, especially in long-range exchange coupled systems.

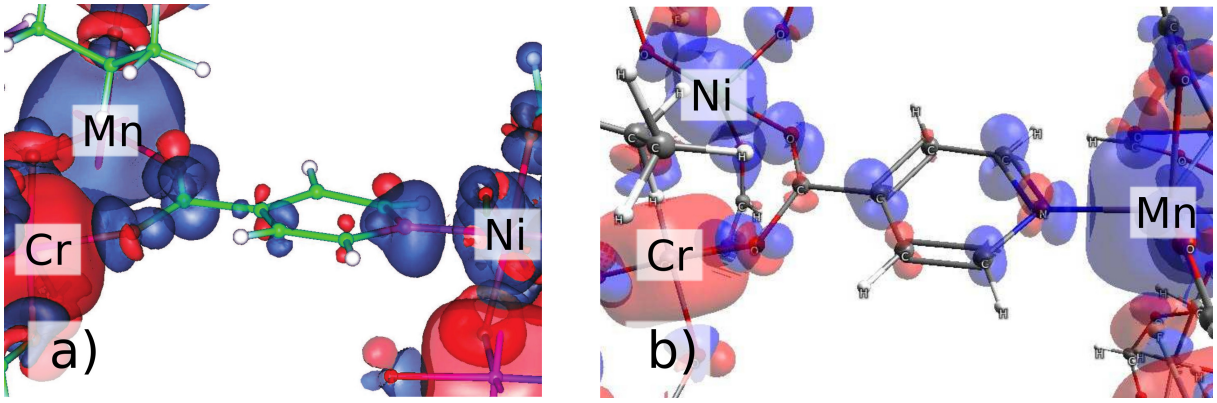

Figure 4.11.: Spin-polarization density in (a) *purple*-Cr_7Ni/pyr/*green*-Cr_7Mn (dimer 4) and (b) *purple*-Cr_7Mn/pyr/*green*-Cr_7Ni (dimer 6), both in the AFM configuration, zoomed in the region of the linker, for isovalues of + (blue) and − (red) 0.0005 electrons/a.u.^{3}

In order to rationalize more quantitatively the above findings, we write down explicitly the microscopic spin Hamiltonian used to map the magnetic configurations energies for dimer 4:

$$Dimer\ 4 \begin{cases} E_{AFM} = E_0 + J_{Ni-Cr}|\mathbf{s}_z^{Ni}||\mathbf{s}_z^{Cr}| - J_{Ni-Mn}|\mathbf{s}_z^{Ni}||\mathbf{s}_z^{Mn}| \\ E_{FM} = E_0 - J_{Ni-Cr}|\mathbf{s}_z^{Ni}||\mathbf{s}_z^{Cr}| + J_{Ni-Mn}|\mathbf{s}_z^{Ni}||\mathbf{s}_z^{Mn}| \end{cases}$$

$$\Rightarrow E_{AFM} - E_{FM} = 2|\mathbf{s}_\mathbf{z}^\mathbf{Ni}|(J_{Ni-Cr}|\mathbf{s}_z^{Cr}| - J_{Ni-Mn}|\mathbf{s}_z^{Mn}|) \tag{4.12}$$

and for dimer 6:

$$Dimer\ 6 \begin{cases} E_{AFM} = E_0 + J_{Mn-Cr}|\mathbf{s}_z^{Mn}||\mathbf{s}_z^{Cr}| - J_{Mn-Ni}|\mathbf{s}_z^{Mn}||\mathbf{s}_z^{Ni}| \\ E_{FM} = E_0 - J_{Mn-Cr}|\mathbf{s}_z^{Mn}||\mathbf{s}_z^{Cr}| + J_{Mn-Ni}|\mathbf{s}_z^{Mn}||\mathbf{s}_z^{Ni}| \end{cases}$$

$$\Rightarrow E_{AFM} - E_{FM} = 2|\mathbf{s}_\mathbf{z}^\mathbf{Mn}|(J_{Mn-Cr}|\mathbf{s}_z^{Cr}| - J_{Mn-Ni}|\mathbf{s}_z^{Ni}|) \tag{4.13}$$

Substituting the exchange parameters of Table 4.4, we see that in equations 4.12 and 4.13 the quantity in the curved brackets is very similar (-0.16 meV versus -0.19 meV); hence the only remarkable difference is the pre-multiplicative factor represented by the spin value of the substituting ion in the *purple* ring, e. g. $|\mathbf{s}_z^{Ni}| = 1$ and $|\mathbf{s}_z^{Mn}| = 5/2$ for dimer 4 and 6, respectively.

The specific heat curves for dimer 4 and 6 depicted in Figure 4.12 supply a nice experimental confirmation of our results.

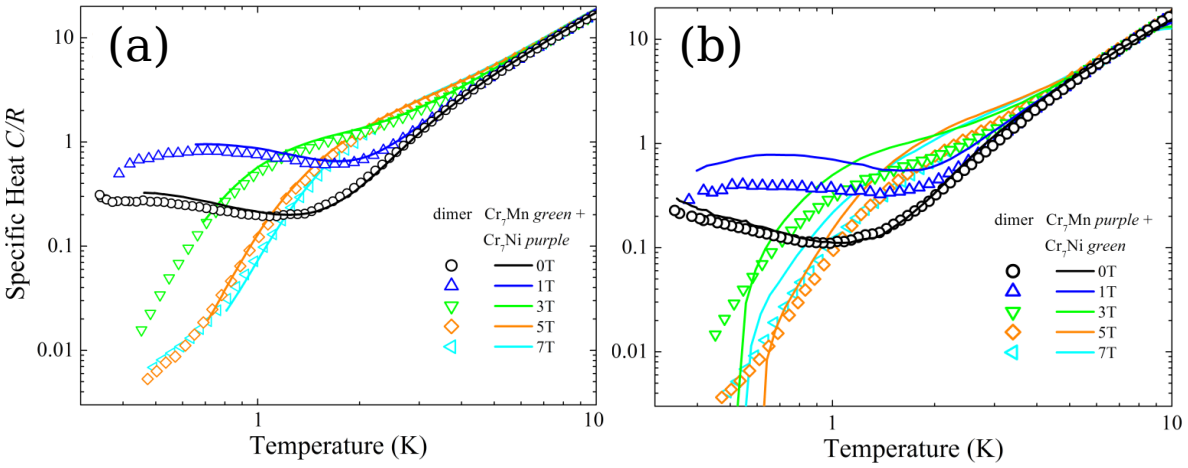

Figure 4.12.: Specif heat of (a) *purple*-Cr_7Ni and *green*-Cr_7Mn rings added compared with the *purple*-Cr_7Ni/pyr/*green*-Cr_7Mn (dimer 4), and (b) *purple*-Cr_7Mn and *green*-Cr_7Ni rings added compared with the *purple*-Cr_7Mn/pyr/*green*-Cr_7Ni (dimer 6). The curves are measured at different magnetic fields and normalized to the gas constant R. The solid lines are the fitted curves of the dimers, while the dot lines represent the sum of the two separated rings.

The sum of the specific heat curves obtained for the separate *purple* and *green* rings (dotted lines) are compared with the specific heat curve measured in the corresponding dimeric supramolecule (solid lines). The magnetic contribution to the specific heat depends on the energy gaps between the magnetic ground state and the lowest lying excited states according to the well known Schottky anomaly expression [106]. In this case, the deviation of the the solid lines from the dotted lines is directly related to the existence of a magnetic coupling between the two rings. The larger deviation in dimer 6 (panel (b)) than in dimer 4 (panel (a)) is in agreement with the DFT results presented in Table 4.4.

Chapter 5.

Graphene-mediated exchange coupling between a molecular spin and magnetic substrates

5.1. Motivations and state of the art

The growing field of organic spintronics capitalizes on the novel functionalities achieved when organic molecules are adsorbed on magnetic substrates. The ability to manipulate and tune these functionalities is an important goal. Several problems remain however, before such systems can be incorporated into new technological devices. One in particular is the capability to adsorb magnetic molecules on surfaces without any detrimental effects being caused to either its structural or magnetic properties. It is thus vital to choose molecules with maximum structural robustness upon adsorption [4, 107, 108]. To this end, the phthalocyanine (Pc) and porphyrin families are popular choices, due to their planar geometry [7, 8, 10, 109–111]. However, the strong interaction between the metal ion of such flat molecules and the substrate often modifies its electronic states and can even quench its magnetic moment [112].

The use of non-planer molecules, such as metallocenes, can minimize this effect. Metallocenes are composed of a $3d$ transition-metal ion sandwiched between two cyclopentadienyls (Cp). Depending on the metal ion species, both non-magnetic and paramagnetic behavior can be found [19]. The spin of the metal ion is shielded from the surface by the cage formed by the two Cp rings, reducing the possibility that it will be modified substantially after ad-

sorption. Other viable route to further decrease an excessive interaction is the intercalation of a decoupling layer between the reactive surface and the molecule [108, 113]. Graphene is an attractive candidate in this regard, primarily due to the unique electronic properties that render it appealing for spintronic applications. It has already been successfully used to decouple Pc molecules from Ru(0001) and Ir(111) [114, 115] substrates. It is still an open question, however, if a graphene layer can preserve the magnetic properties of an adsorbed molecule without simultaneously hindering a stable magnetic coupling between the molecular moment and the magnetic substrate. Recent observations of charge transfer at molecule-graphene-Ni(111) interfaces [116, 117] would suggest that a magnetic coupling between a molecule and a substrate through a graphene layer is achievable. Due to the unique electronic properties of graphene [118–120], metal-organic systems of this kind could serve as a basis for future spintronic devices.

During this thesis first-principles calculations were used to investigate the magnetic properties of cobaltocene ($CoCp_2$) adsorbed on a graphene layer deposited on a magnetic substrate, in the first part Ni(111). Furthermore, intercalation of different ferromagnetic metal monolayers, such as Fe and Co, between graphene and the Ni substrate were proposed as a route to change the magnetic coupling.

5.2. Description of the system

For a comprehensive and complete theoretical characterization of the magnetic exchange between $CoCp_2$ and the graphene/metals substrate, in addition to a systematics on the adsorption site that the molecule attains on the surface, we had to proceed with a refined study on the two components of our system, i.e. the molecule and the substrate, separately. In fact, the singular components, even though extensively studied, still present unclear points. In the following sections we will shortly revisit the main results that have been obtained so far by experimental and theoretical approaches.

The electronic and molecular structure of $CoCp_2$ predicted by DFT approaches is presented, and compared with our calculations. The structures/stackings which have been identified in the graphene/Ni(111) and graphene/Fe/Ni(111) substrates are revisited and discussed.

5.2.1. The Cobaltocene molecule

The family of metallocenes is composed by a $3d$ transition metal ion (Tm) ion sandwiched between two cyclopentadienyl (Cp, C_5H_5) rings, i.e. $TmCp_2$. Depending on the choice of Tm, a spin is induced on the molecule for all the elements of the $3d$ series, with the exception of Fe (see Tab. 5.1)

Table 5.1.: Spin induced on a metallocene molecule $TmCp_2$, as a function of the transition metal ion Tm

Tm ion	V	Cr	Mn	Fe	Co	Ni
S	3/2	1	1/2	0	1/2	1

Isolated $CoCp_2$, and other members of the metallocene family have already been studied extensively by DFT [19]. Two possible conformations with different symmetry are observed, labelled as D_{5h} and D_{5d} and shown in Fig. 5.1. Total energy calculations show that D_{5h} symmetry is energetically favored for all the choice of Tm, with respect to D_{5d}.

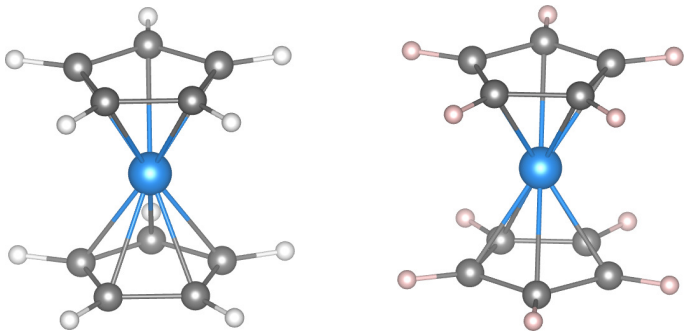

Figure 5.1.: (a) $CoCp_2$ in the symmetry configuration D_{5h}. (b) $CoCp_2$ in the symmetry configuration D_{5d}. Co, C, H atoms in $CoCp_2$ are colored blue, grey, white, respectively.

If we consider $CoCp_2$ in the energetically lowest high-symmetry configuration (D_{5h}), there are two possible Jahn-Teller distorted structures with lower symmetries, characterized by two different electronic states. The crystal field produced by the Cp rings splits the $3d$ orbitals of Co. If we consider the axis of the molecule (intersecting the centers of the two Cp rings) as our z-axis, the seven $3d$ electrons are split in: (i) two electrons in a single orbital derived from d_{z^2}, (ii) four electrons in a doubly degenerate orbitals derived from d_{xy}

and $d_{x^2-y^2}$, (iii) one electron in a doubly degenerate orbitals derived from d_{yz} and d_{xz}. The D_{5h} symmetry is distorted to remove the degeneracy of the frontier orbitals, according to the Jahn-Teller effect, so the symmetry is reduced to C_{2v}. Depending on whether the Cp rings tilt slightly toward the molecular center or outwards, the $^2B_2$ or the $^2A_2$ electronic states are respectively produced (see Fig. 5.2). During our work, the two stable structures $^2B_2$ and $^2A_2$ were recalculated using the PBE functional as implemented in VASP. We confirmed the $^2B_2$ as the ground state. The energy difference between the two states was 0.3 meV , in good agreement with the calculated value of 0.26 meV obtained with the B3LYP functional [19].

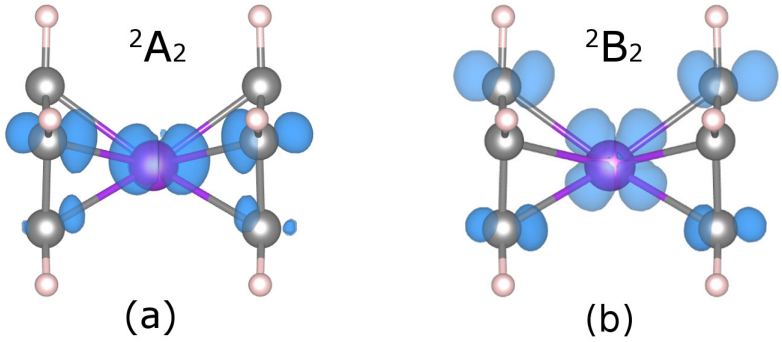

Figure 5.2.: Probability density of the $CoCp_2$ HOMO for the (a) $^2A_2$ and (b) $^2B_2$ states.

To each distorted structure is associated a different electronic state, but in both cases, the $CoCp_2$ molecule attains a nominal S=1/2 spin. The magnetic moment of Co ion calculated by the VASP code, by integrating the spin density within a sphere of 1.3Å is 0.74 μ_B. The probability density of the highest occupied molecular orbital (HOMO) of the two possible electronic states are plotted in Figure 5.2. In the $^2B_2$ state, the HOMO has d_{yz} character while in the $^2A_2$ state it has d_{xz} character. It is important to notice that the extension of the HOMO of $^2A_2$ on the Cp rings is quite small compared to the $^2B_2$. As we will see later, the magnetic coupling between molecule and substrate is largely affected by these small changes in the HOMO. For the sake of completeness the density of states (DOS) of the $^2B_2$ state, in the case the Co atom attains a negative spin, is shown in Figure 5.3. According to the previous investigations, also in our calculations the HOMO and LUMO energy are close in energy (less than 1 eV).

We also mention a DFT characterization of the trend in charge transfer between metallocenes and an unsupported graphene layer [121]. In this work two main messages, interesting for our purpose, could be captured. The first is that cobaltocene is the member

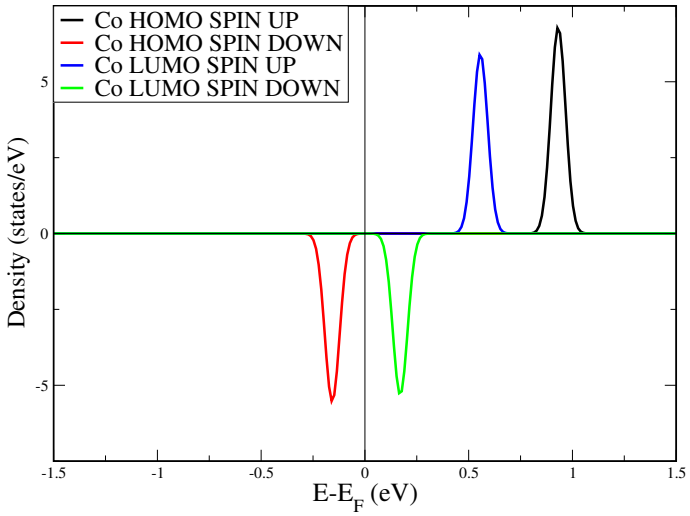

Figure 5.3.: Spin-polarized LDOS of $CoCp_2$ in $^2B_2$ with a $(-)$ spin moment projected on $3d$ states of Co.

across the metallocene family which presents the largest charge transfer to the graphene layer; this has been somehow inspiring for our work, since a large interaction with the graphene layer could then imply the existence of communication channels, eventually able to mediate the spin interaction through the graphene layer.

5.2.2. Graphene on metal substrates

Large efforts have been dedicated to grow graphene on metal substrates, with a variety of experimental methods. The very small lattice mismatch (1.2%) between the graphene and Ni(111) surface lattice constant results in pseudomorphic growth and the flat conformation of the graphene layer [122]. This is in contrast with other metallic substrate, for instance Rh, where Moiré patterns, with hills and valleys, are observed in graphene [123]. The morphology of the graphene/Ni(111) interface has been investigated experimentally by a combined high-resolution X-ray photoelectron spectroscopy (HR-XPS) and DFT calculations [20] and two stable configurations have been observed (see Figure 5.4(a)-(b)). The top-fcc stacking has two inequivalent C atoms, one on top of the Ni(111) surface atom (C_{top}), the other on the fcc site (C_{fcc}). The carbon atoms of the bridge-top stacking are in bridge positions with respect to underlying Ni atoms. All the other possible stacking of graphene on Ni have been found to be energetically unstable, and allowing structural relaxation at the interface they are observed to fall into the energy minimum of the two stacking described

above. Considering the the energy difference between the top-fcc and bridge-top stackings is not large (and most importantly, depending on the method/code used, one or the other are predicted to be the ground state), we had necessarily to consider both of them, check within our method which of the two is the ground state, and see how the stacking influences the molecule-substrate magnetic exchange.

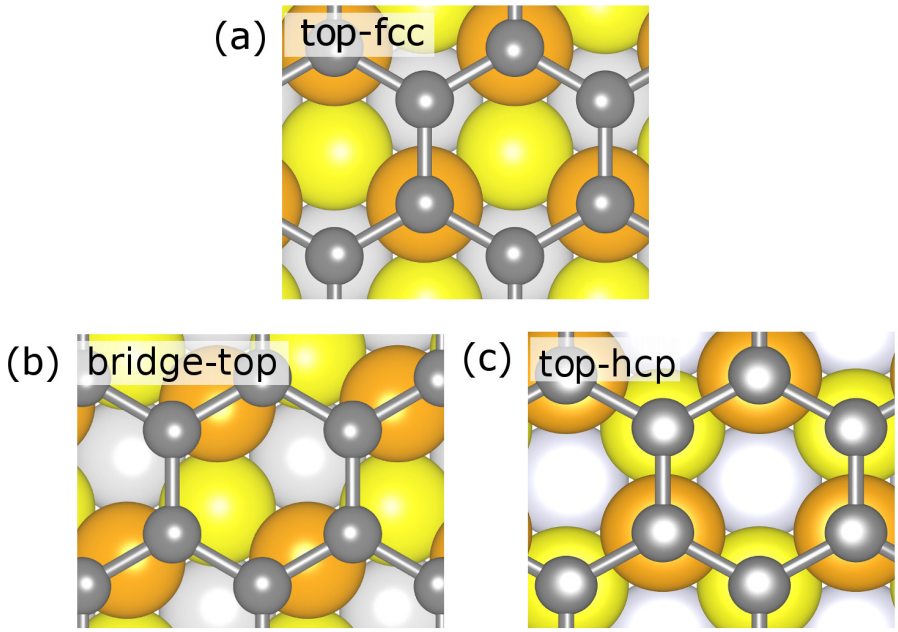

Figure 5.4.: (a) top-fcc stacking of graphene on Ni(111) . (b) bridge-top stacking of graphene on Ni(111). (c) top-hcp stacking of graphene on Me/Ni(111) (Me = Fe, Co). The topmost, second, and third metal layers are colored orange, yellow, and grey, respectively.

Direct deposition of graphene on Fe and Co has not been achieved, due to the lattice mismatch. Instead, when graphene is deposited on Ir(111), it is possible to intercalate below graphene monolayer of 3*d* tansition metals, e.g. Ni and Co [124,125] ; similarly, intercalation of Fe between graphene and Ni(111) [126] has been successfully achieved experimentally. As discussed in Ref. [126], the intercalated Fe atoms are preferentially placed in the fcc hollow sites of the Ni, following the Ni(111) stacking. On this substrate, graphene adsorbs in a top-hcp structure (see Figure 5.4(c)), where the two inequivalent graphene C atoms are placed alternatively above the Fe atoms and the hcp sites (corresponding to the topmost Ni layer). No intercalation of Co between graphene and Ni has been tempted so far.

5.3. Results

Hereafter we present the results obtained employing by using the VASP code (see Chapter 3 for details). We will first discuss some test calculations on the graphene/M/Ni(111) (M=Ni, Fe and Co) substrates, comparing our findings with the previous literature. Later, the possible adsorption sites of the $CoCp_2$ molecule on the graphene/Ni(111) will be presented. The exchange parameters founded for different situation will be shown with a detailed explanation of how the structural factors affect the magnetic coupling. In the last sections, the results will be rationalized with the assistance of spin-polarized LDOS analysis and cross sectional plots of the magnetization density, leading us to the final considerations.

5.3.1. The graphene/M/Ni(111) substrate, with M=Ni, Fe and Co

As described in Chapter 3 the non-local exchange-correlation energy functional vdW-DF results in an equilibrium distance between graphene and the topmost Ni layer larger than 3.5 Å [127] for all the calculated structures, in disagreement with experiments. We thus employed DFT-D2 method in all our calculations. We found a binding distance of ∼2.1 Å for both the top-fcc and bridge-top, in good agreement with experiments [63]. Regarding the simulation cells, we proceeded in a two step characterization of the molecule-substrate interface. A preliminary calculation on a p(1 × 1) hexagonal supercell has been carried out to obtain geometry optimized graphene/M/Ni(111) (M = Ni, Co, Fe) structures, simulating the substrate with a slab containing one layer (two C atoms) of graphene and four layers of metal. Here, an optimized Γ-centered k-point grid of 17 × 17 × 1 has been used for the Brillouin Zone (BZ) sampling. The graphene layer together with the metal layer below were allowed to relax along the z-axis, while the three bottom layers of Ni were kept fixed in their bulk geometry, i.e. with a PBE optimized lattice parameter of 2.49 Å. We verified the validity of this geometry comparing it to a p(1× 1) unit cell with a six-layer metal slab allowing the graphene layer and the three topmost layers of Ni to relax in all directions (i.e. fully relaxing four substrate layers). The geometry parameters are compared in Table 5.2. In summary, the C-Ni distance (d_0) changes as little as 0.001 Å and the distance between the Ni surface and subsurface layer (d_1) varies of 0.004 Å. The magnetic moments of C atoms and Ni topmost atoms changes respectively of 0.002 μ_B and 0.019 μ_B. Overall, we

conclude the modifications in the C-Ni distance and the magnetic moments of the C atoms and the surface Ni atoms are minor and they would not affect the interaction between molecule and substrate, allowing us to use a four-layer rather than a six-layer Ni slab.

Table 5.2.: Geometry parameters of graphene/Ni(111) substrate obtained with a four− and six−layer metal slab, respectively. d_0 is the distance between the graphene overlayer and the interface Ni layer; d_1 is the distance between the interface Ni layer and the second Ni layer; d_2 is the distance between the second and third Ni layers; d_3 is the distance between the third and fourth Ni layers. All the distances are in Angstrom (Å).

	4−layer slab	6−layer slab
d_0	2.118	2.119
d_1	1.995	1.998
d_2	2.015	1.987
d_3	2.015	2.003

Also, in our simulations the top-fcc and bridge-top stacking are very close in energy but in contradiction with the theoretical calculations of Zhao et al. [20], we found the top-fcc is more stable by 6.5 meV per C atom than the bridge-top stacking. We believe this difference is due to the use of a different semi-empirical potential for the description of the dispersion forces [128]. To the best of our knowledge, there is no experimental data regarding the intercalation of Co between graphene and Ni(111) and so we have used the same structure as for graphene/Fe/Ni(111). This has the added advantage that it allows for a direct comparison between the different systems and therefore a clearer insight into the mechanism of the exchange interaction. We found for both graphene/Fe/Ni(111) and graphene/Co/Ni(111) a distance of ∼2.1 Å (close to the one of graphene/Ni(111)) between the graphene and the topmost metal layer.

5.3.2. The adsorption of $CoCp_2$ on graphene/Ni(111) and pristine Ni(111)

Electronic coupling

The molecule-substrate systems have been simulated building a p(5×5) supercell, where molecule replicas are separated from each other by more than 8 Å. In these second set of calculations, the atomic positions in the graphene and metal layers are the ones minimized in the p(1×1) cell, and only the $CoCp_2$ coordinates were allowed to further relax till forces were lower than 0.01 eV $Å^{-1}$. A Γ-centered grid of $3 \times 3 \times 1$ k-points has been used for BZ sampling. Several ingredients have been tested in order to thoroughly characterize the cobaltocene/graphene/metal interface, namely the structural conformation of the isolated molecules, the type of stacking that graphene attains on the metal substrates, and the possible adsorption sites of the $CoCp_2$ molecule. The configuration with the molecule axis parallel to the graphene layer is found to be more stable (by 40 meV), compared to the case of perpendicular orientation, consistent with Ref. [121]. Keeping the molecule axis parallel to the graphene layer, we have taken into account several possible adsorption site that $CoCp_2$ can attain on graphene/Ni(111), which we labelled as hollow, bridge, and top, depending on the position of the Co atom with respect to the C atoms below (Figure 5.5).

The main results are presented in Table 5.3, which list the total energy difference ΔE (with respect to the ground state) together with the Co-graphene distance d (third and fourth column). A comparison of the total energies in Table 5.3 shows that, except for the case of configuration 2, all other structural configurations are energetically unfavorable by several tens of meVs. The lowest energy configuration is found when the molecule is adsorbed on the hollow site of graphene, with graphene with top-fcc stacking on the underlying Ni(111) substrate. This adsorption is accompanied by a charge transfer of 0.28 e^- from the molecule to the surface and a decrease of the magnetic moment associated to the Co atom from +0.74 μ_B to +0.47 μ_B [1]. The calculated adsorption energy in the ground state configuration, i.e. configuration 1 in Table 5.3, is ∼0.64 eV, a value somewhere between those indicating physisorption and chemisorption.

We argue that the binding can be regarded as strong physisorption - inferred from the fact that (i) the smallest distance between the H atoms of $CoCp_2$ and the C atoms of

[1] Charge transfers were calculated using the Bader analysis [129]

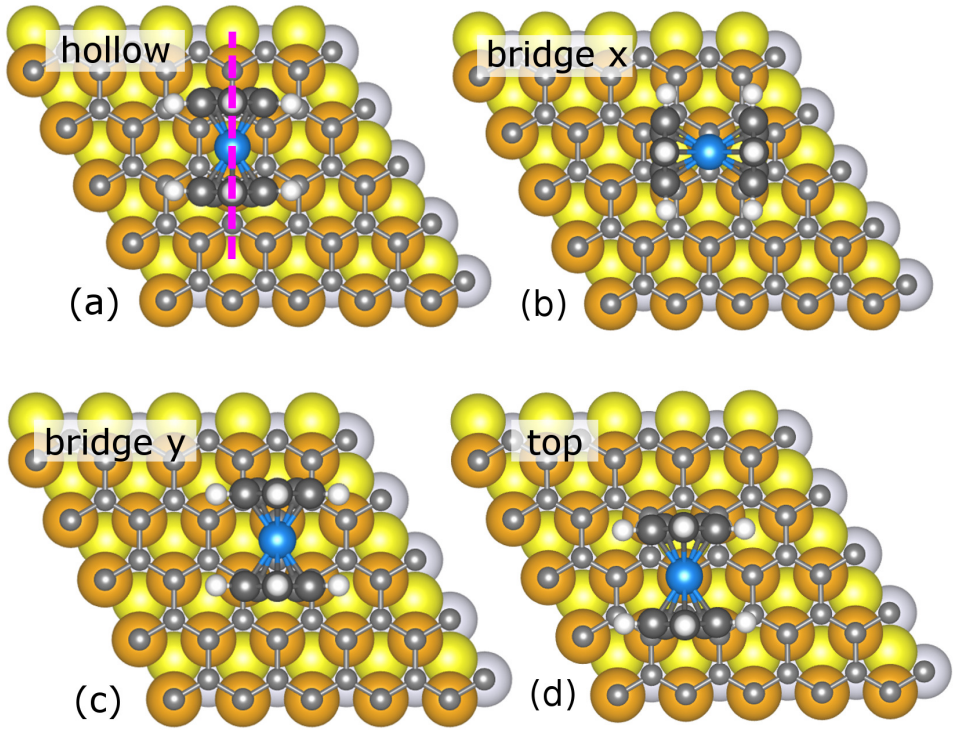

Figure 5.5.: Adsorption geometries of the $CoCp_2$ on graphene/Ni(111) for the top-fcc stacking. Depending on the position they were called (a) hollow, (b) bridge x, when the axis of the molecule is parallel to the arbitrary defined x-axis, (c) bridge y, when the axis of the molecule is parallel to the arbitrary defined y-axis and (d) top. In all the representations Co, C, H atoms in $CoCp_2$ are colored blue, dark grey, white, respectively).

Table 5.3.: Total energy difference ΔE (meV), Co-graphene distance d (Å), and exchange energy E_{ex} (meV) for different structural and electronic configurations of $CoCp_2$ on graphene/Ni(111) for antiparallel alignment of Co and Ni magnetic moments.

	Configuration	ΔE	d	E_{ex}
$^2B_2$, top-fcc, hollow	1	0.0	4.31	−9.7
$^2A_2$, top-fcc, hollow	2	+4.6	4.31	−1.3
$^2B_2$, top-fcc, bridge x	3	+55.2	4.30	−4.6
$^2B_2$, top-fcc, bridge y	4	+74.8	4.31	−8.1
$^2B_2$, bridge-top, hollow	5	+105.2	4.29	−9.2
$^2B_2$, top-fcc, top	6	+147.9	4.40	−6.8

graphene is ∼2.4 Å, (ii) there is no appreciable distortion of the structure of $CoCp_2$ upon deposition on the surface, and (iii) the C – C, C – Ni and C – H bonds are non-polar (or only weakly polar) excluding the formation of hydrogen bonds. To unambiguously determine the role of graphene in mediating the interaction between $CoCp_2$ and the magnetic substrate, we considered the situation when $CoCp_2$ is adsorbed directly on the Ni(111) surface. In this case, the molecule is chemisorbed with a distance between the Co and Ni atoms of $d = 4.3$ Å and an adsorption energy of ∼1.3 eV, i.e. about twice as large the one found in the presence of the graphene layer. The charge transfer from $CoCp_2$ to Ni approximately doubles from 0.28 to 0.64 electrons if the spacing layer is removed. This indicates that graphene plays a crucial role in the electronic decoupling of the molecule and the substrate, and can facilitate the preservation of the structural integrity of such molecules upon deposition on metallic surfaces. As a matter of fact, it has been previously shown that deposition of metallocenes on metallic surfaces is a difficult process [130] and can, in some cases, result in the complete dissociation of the molecule [131, 132].

Magnetic coupling

In Table 5.3 the exchange coupling energies E_{ex} are shown, defined as $E_{ex} = E_{AP} - E_P$, where E_{AP} (E_P) is the total energy of the system when the spin moment of the Co atom is antiparallel (parallel) to the one of the Ni slab. Here, a negative value of the exchange energy indicates that the cobaltocene's spin moment preferentially orients antiparallel to the Ni magnetization. In the ground state, the molecular spin preferentially aligns antiparallel to the Ni magnetization, with E_{ex} of the order of -10 meV. This energy is remarkably large if we consider that the distance between the Co and Ni atoms is approximately 6.4 Å. As a comparison, an exchange energy of only 50 meV was found for chemisorbed Fe porphyrin on Co(100) [8], despite the much smaller Fe – Co distance of 3.5 Å. The values of E_{ex} that we find are high enough to ensure the stability of the spin moments against fluctuations induced by temperature under typical experimental conditions, i.e. well above the temperature of the order of a few Kelvins that is employed in state-of-the-art X-ray magnetic dichroism and spin-polarized scanning tunneling microscopy (STM) experiments. In all cases, the relaxed adsorption distance between the Co ion and graphene lies between 4.3 and 4.4 Å and, therefore, cannot play a strong role in the differing exchange energies.

To elucidate the physical origin of the molecule-substrate exchange coupling we modified independently three possible contributions: the $CoCp_2$ electronic state, the graphene

stacking, and the $CoCp_2$ adsorption site, as sketched in Figures 5.2, 5.4 and 5.5, respectively Regarding the first contribution, we found that switching from the $^2B_2$ to the $^2A_2$ electronic configurations (configurations 1 and 2 in Table 5.3) lowers the exchange energy from -9.7 to -1.3 meV. This considerable decrease can be attributed to the reduced extent of the $CoCp_2$ spin-polarized HOMO (see Figure 5.2), which is critical to determining the size of the coupling. Varying the graphene stacking from top-fcc to bridge-top (configurations 1 and 5) does not influence the magnetic coupling in any appreciable way, indeed the E_{ex} of configuration 5 is -9.2 meV. This is somewhat surprising since the magnetic moment induced on graphene is approximately one order of magnitude smaller in the bridge-top than in the top-fcc stacking, with values of $+0.002$ μ_B and -0.03 / $+0.02$ μ_B, respectively. We can conclude therefore that the magnetic coupling does not depend on the size of the magnetic moment induced on the graphene atoms. Finally, varying the adsorption site (configurations 1, 3, 4 and 6) we found the values of -9.7, -4.6, -8.1 and -6.8 meV, respectively for the configurations 1, 3, 4 and 6. However, although E_{ex} changes up to a factor of two, the coupling remains antiferromagnetic in all cases. As discussed in Section 5.3.2 the magnetic moment of Co ion for the isolated $CoCp_2$ molecule is 0.74 μ_B; this moment becomes fully quenched when it is directly adsorbed on Ni(111). The molecular spin can be recovered by rigidly shifting the molecule away from the surface by 1 Å whereby the Co ion attains a magnetic moment of $+0.26$ μ_B. As for the case including the graphene layer, the magnetic coupling is antiparallel, albeit weakly ($E_{ex} = -0.4$ meV). A further rigid shift of the molecule by 1 Å results in an increase of the Co magnetic moment to $+0.35$ μ_B while the exchange coupling becomes negligibly small. This clearly demonstrates that graphene is essential to preserve the magnetic properties of the molecule. The influence of an on-site Coulomb interaction in the d orbitals of the Co atom in $CoCp_2$ on the exchange coupling energies E_{ex} for the cases of $CoCp_2$ on graphene/Ni(111) and $CoCp_2$ on graphene/Fe/Ni(111) has been also checked, using the GGA+U the formalism introduced in Section 3.3.4, and values of U-J up to 4 eV have been tested. The magnetic coupling of the investigated systems results only weakly affected by the application of an effective Hamiltonian U. The net effect is a small rise (less than 1 meV) in the exchange coupling magnitude.

Our results differ from the ones contained in a recent study of Co-porphyrin on graphene/Ni(111) [9]. From XMCD measurements they estimate an antiferromagnetic coupling of $E_{ex} = (-1.8 \pm 0.5)$ meV . They present also a DFT characterization of the system, with a methodology similar to ours, i.e. VASP and GGA+U functional. They

calculate a ferromagnetic coupling of hundred meV for the bridge-top stacking, and an antiferromagnetic coupling of the same amount for top-fcc stacking, thus concluding that it must necessarily be the bridge-top the most present stacking in the sample of the experiments. Further, they suggest the graphene π-bonded sheet mediates a weak super-exchange between the spin polarization of Ni and the pyrrolic nitrogens of the ring. Since the exchange between Co-porpyrin and the Ni substrate depends in their case crucially on the spin-polarization of the C atoms of graphene (while in our case, the stacking is not influential), it is likely that the molecules adsorbe on different sites and couple both ferro- and antiferromagnetically to the substrate; the XMCD signal is then an average of all this coupling, and this could also explain the overestimation of a factor of 50, which is well beyond the precision of the DFT calculation.

5.3.3. Understanding and tuning the magnetic coupling

In Figure 5.6 we present the spin-polarized local density of states (LDOS) of the system in its ground state (configuration 1). Majority (upper panel) and minority (lower panel) states are defined according to the magnetization of the Ni(111) substrate. Upon adsorption on the surface, we observe a small shift to higher energies of the molecular Co d orbitals with the result that the HOMO is pinned to the Fermi level (E_F) of the substrate. It also becomes partially depopulated. As indicated in the previous sections this depopulation is accompanied by a charge transfer of 0.28 e^- from the molecule to the surface and a decrease of the magnetic moment associated to the Co atom from +0.74 μ_B to +0.47 μ_B. A hybridization between the $2p_z$ orbital of the graphene atoms and the $3d_{z^2}$ orbital of the Ni atom is also evident, resulting in the polarization of graphene.

Notably, only the C_{fcc} atoms exhibit this strong hybridization with the Ni atoms close to E_F. The energy overlap between the minority states of graphene and the minority d states of $CoCp_2$ just below E_F is responsible for the stabilization of the antiparallel alignment. This energy matching is absent for the parallel alignment, due to the inverted HOMO spin polarization. We can thus conclude that the spin polarization of graphene close to E_F determines the sign of the magnetic coupling. This is further corroborated by the analogous situation occurring for configuration 5, for which both the graphene LDOS around E_F (see Figure 5.7(a)-(b)) and the magnetic coupling are similar to the ones of configuration 1.

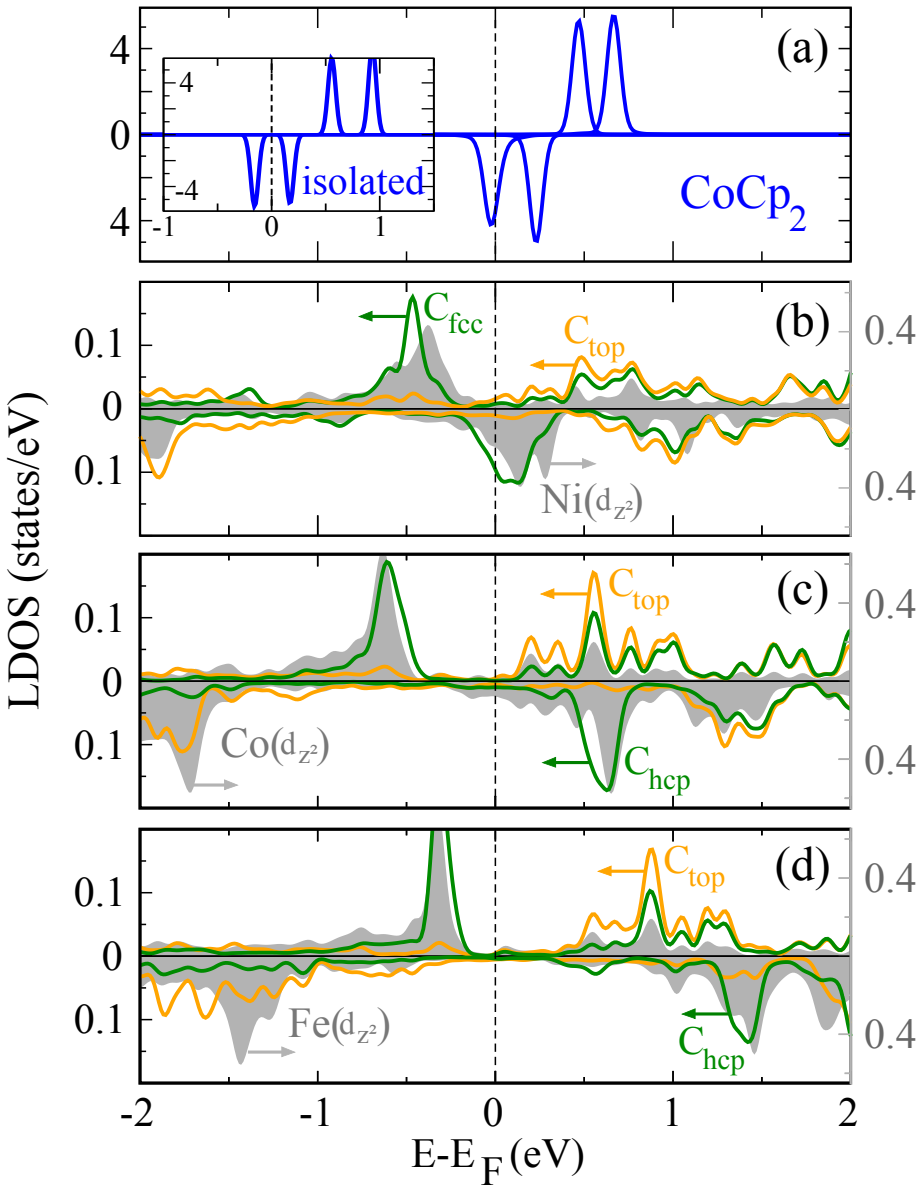

Figure 5.6.: Spin-polarized LDOS of $CoCp_2$ on graphene/M/Ni(111) in the antiparallel configuration, with M = Ni, Co and Fe: (a) $3d$ states of Co of $CoCp_2$; (b)-(d) $3d_{z^2}$ states of the M layer atoms and $2p_z$ states of C_{top} and C_{fcc} (for M=Ni) or C_{top} and C_{hcp} (for M = Co, Fe; see text). The d states of the M layer are plotted in grey, while graphene C p states are in orange and dark green. Each curve in panels (b)-(d) is the average over the three atoms of that species closest to the $CoCp_2$ center. Inset in panel (a): $3d$ states of Co of $CoCp_2$ for the isolated molecule

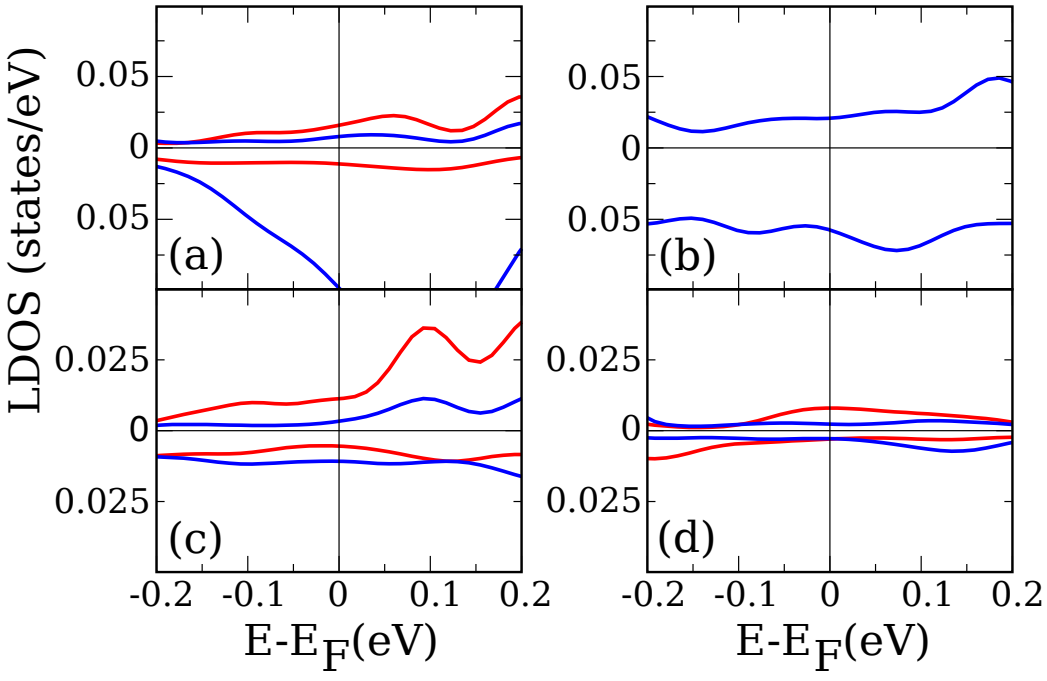

Figure 5.7.: Spin-polarized LDOS at the C graphene atoms, close to the Fermi level (E_F). (a) $2p_z$ states of C_{top} and C_{fcc} atoms for the configuration 1 of Table 5.3. (b) $2p_z$ states of the only inequivalent C atom for the configuration 5 of Table 5.3. (c) $2p_z$ states of C_{top} and C_{hcp} atoms for the Co system. (d) $2p_z$ states of C_{top} and C_{hcp} atoms for the Fe system. Each curve is the average over the three atoms of that species closest to the $CoCp_2$ center. The C_{top} and C_{fcc}/C_{hcp} curves are colored red and blue, respectively.

Such a dependence suggests that if one can modify the induced spin polarization of graphene in this energy window, one can modify the magnetic coupling. As a possible realization, we have explored the effect of intercalating different magnetic monolayers (Fe and Co) between graphene and the Ni(111) substrate.

Table 5.4.: Magnetic moments of the two non-equivalent atoms of graphene m_C^{top} (μ_B) and $m_C^{fcc/hcp}$ (μ_B), the interface metal monolayer m_M (μ_B), and the exchange energies E_{ex} (meV) for $CoCp_2$ on graphene/M/Ni(111) (M = Ni, Co, Fe).

	gr/Ni/Ni	gr/Co/Ni	gr/Fe/Ni
m_C^{top}	−0.02	−0.04	−0.05
$m_C^{fcc/hcp}$	+0.03	+0.04	+0.04
m_M	+0.47	+1.52	+2.39
E_{ex}	−9.7	−2.3	+2.0

We present in Figure 5.6 (c) and (d) the LDOS in the case of Fe and Co intercalation. The values of the corresponding magnetic moments and the exchange energies are listed in Table 5.4. The magnitude of the spin moment in the interface metal (M) layer increases as one goes from Ni to Co to Fe and, due to hybridization, this increase also occurs for the moments induced on the C atoms, i.e., m_C^{top} and $m_C^{fcc/hcp}$. As we showed earlier, the magnetic coupling is not found to increase in line with the magnetic moment and in fact decreases. We can identify a trend for the exchange energy between $CoCp_2$ and the investigated substrate from large antiferromagnetic ($E_{ex} = -9.7$ meV) for graphene/Ni(111), to weak antiferromagnetic ($E_{ex} = -2.3$ meV) for graphene/Co/Ni(111) and weak ferromagnetic ($E_{ex} = +2.0$ meV) for graphene/Fe/Ni(111). The energy matching between the HOMO of $CoCp_2$ and the p_z states of the carbon atoms, which drives the coupling between the molecule and substrate, is disrupted by the intercalation of the metal layer. The minority d_{z^2} states of the Co layer lie at higher energies than those of Ni and the Fe states are found at even higher energies. Due to hybridisation, the p_z orbitals of the graphene atoms are similarly shifted to higher energies. This reduces (for Co intercalation) and finally prevents (for Fe intercalation) the energy matching of the C states with the spin-polarized HOMO of $CoCp_2$ with a resultant decrease in the magnetic coupling. Figure 5.7(c) confirms this behavior for graphene/Co/Ni(111) system, indeed the area subtended by the two curves in the region within 0.1 eV below E_F in the minority spin channel is larger than the one in the majority channel, and so the matching with the $CoCp_2$ HOMO results still in a

(slightly smaller) antiparallel coupling. On the other hand, for graphene/Fe/Ni(111) (see Figure 5.7(d)), in the same energy region, there is a small excess of majority spin, which is consistent with the small parallel coupling between the molecule and the substrate spins. To complete our investigations, 4s states of the topmost metal layer M for graphene/M/Ni(111) systems with M= Fe, Co, Ni are shown in Figure 5.8. The majority 4s states of Co are slightly shifted at lower energy than those of Ni and the Fe states are shifted at even lower energies, very close to the Fermi energy. The central peak in the majority states increases their intensity moving from Ni to Fe. The LDOS of the 4s states are smaller than the corresponding 3d states, nevertheless in cases where the intensity of the 3d becomes sufficiently small, the 4s states could give a significant contribution in the polarization of the $2p_z$ orbitals of the graphene. The trend in the exchange coupling for the intercalation of different monolayer (Ni, Co and Fe) support this hypothesis, changing from strongly antiferromagnetic for the Ni to weakly ferromagnetic for Fe.

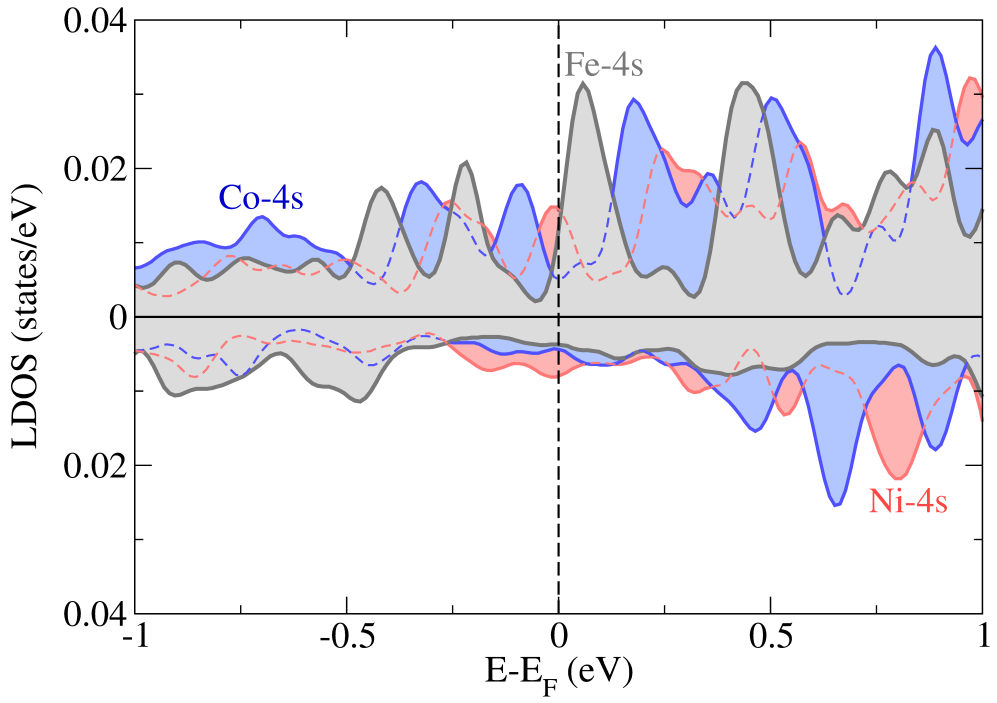

Figure 5.8.: Projected density of states for the intercalated metallic monolayer in graphene/Me/Ni(111) (Me = Fe, Co, Ni) structures; 4s states of Fe (dark grey), 4s states of Co (light blue), 4s states of Ni (light red).

5.3.4. Charge-transfer 3D plots and magnetization density cross-sections

As discussed early, upon adsorption a charge transfer from the molecule to the substrate occurs. In order to visualize where the charge redistribution takes place, we plot in Fig. 5.9 the three-dimensional charge density difference, defined as follows. First, we calculated the charge density of the whole system molecule+substrate, then we calculated the charge density of the single components (e. g. the molecule and the substrate, separately), using the same simulation cell. Finally the charge density of the two components were subtracted by the density of the whole system. This has been done for the two spin channels, (+) and (−), separately. Regions of electron accumulation (depletion) are indicated with the red(blue) color.

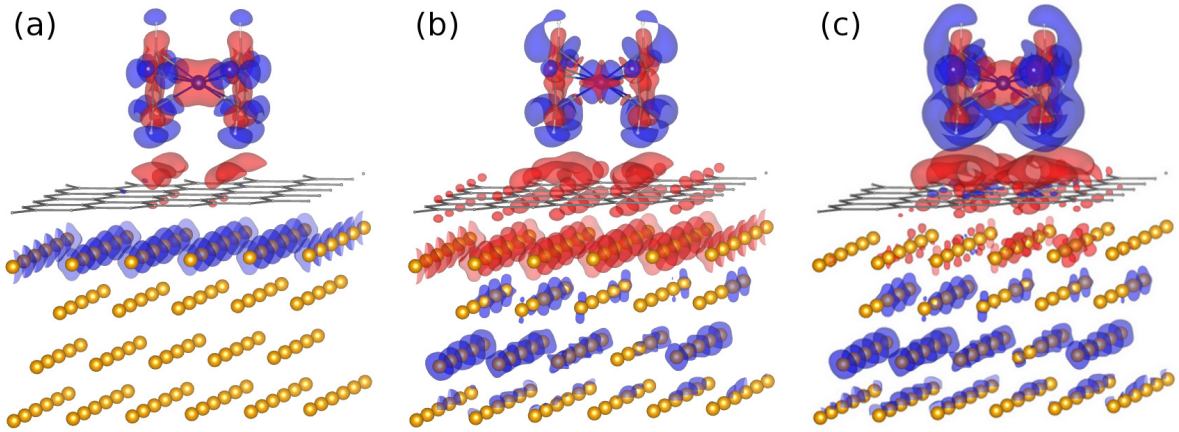

Figure 5.9.: Charge density difference $\Delta\rho^{\sigma}$ for the $CoCp_2$ on graphene/Ni(111) ($^2B_2$, top-fcc, hollow), defined as $\Delta\rho^{\sigma} = \rho^{\sigma}_{mol.+sub.} - \rho^{\sigma}_{mol.} - \rho^{\sigma}_{sub.}$, with σ=(+), (−), (+ & −). Charge density difference for σ=(+) (a). The charge density difference for σ=(−) (b). The charge density difference for σ=(+ & −) (c). The isosurface is of $\pm 7.5 \times 10^{-8} e/\text{Å}^3$. The electron accumulation and depletion regions are depicted in red and blue, respectively.

Looking only at the spin (+) density (Figure 5.9(a)) it can be noticed a density depletion in the topmost Ni layer. This is opposite to what happens for the spin (−) density (Figure 5.9(b)) where a marked density increase can be observed both over the graphene and the topmost Ni layer. The negative value of E_{ex} observed for configuration 1 is connected with the enhanced density of the spin (−) along the first Ni layer. The total charge redistribution depicted in Figure 5.9(c) reveals an increase of the charge density (red) in a region between

the molecule and the graphene. The molecule undergoes an internal charge rearrangement. The same effect, albeit weaker, can be observed also between the Ni layers. A very small charge density increase can be recognized in the density of the topmost Ni layer together with a small decrease in the lower layers. This redistribution in the Ni inner layer can be tentatively explained with a image-charge effect due to the presence of the molecole; yet, it could also be somehow enhanced in a artificial way because of the finite size of the Ni slab.

Cross sectional plots of the magnetization density, i.e. the difference between the spin up and down charge densities, close to the Fermi level are given in Figure 5.10. In panel (a) the spatial matching of the $CoCp_2$ HOMO with the p_z orbitals of the C_{fcc} atom of graphene adsorbed on Ni(111) is evident in the antiparallel alignment where spin density lobes from the molecule and the surface atoms merge. In contrast, it is absent in the parallel alignment resulting in a negative exchange energy. For $CoCp_2$ on graphene/Co/Ni (Figure 5.10(b)) there is an excess of majority spin for the C_{top} atoms and of minority spin for the C_{hcp} atoms which almost cancel each other.

However, a small preference towards communication through the minority spin is suggested by the plot in accordance with the weak antiferromagnetic coupling. For the Fe intercalated layer (Figure 5.10(c)), the spin density in the graphene indicates spin communication for the parallel alignment, but not for the antiparallel, explaining the positive exchange energy. The analysis performed for configuration 5 of Table 5.3 (see Figure 5.11) reveals a scenario similar to the one of Figure 5.10(a) and is consistent with an exchange coupling of similar size. In contrast, in configuration 2 spatial overlap between $CoCp_2$ and graphene states at E_F is absent, which explains the much weaker magnetic interaction as compared to configuration 1.

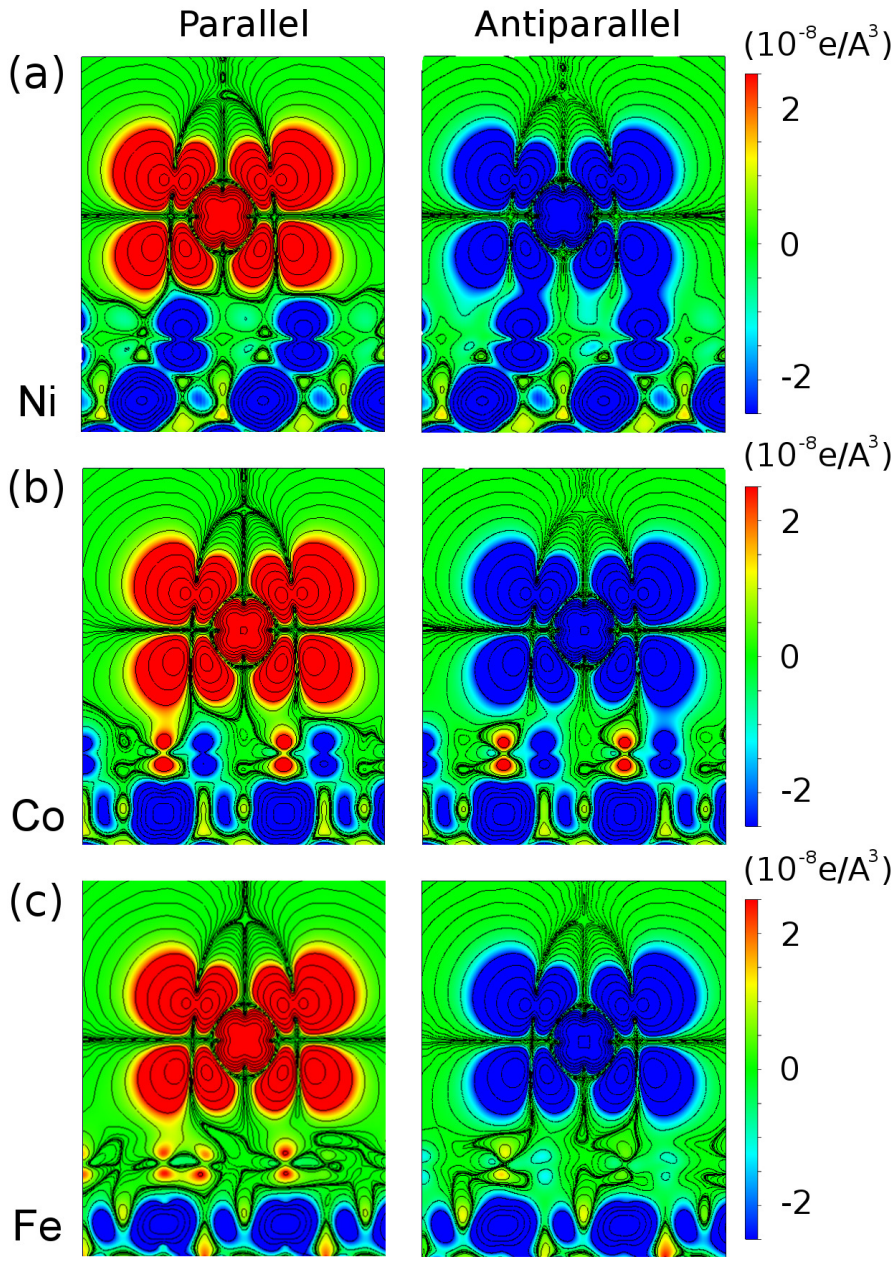

Figure 5.10.: Cross-sectional plots of the local magnetization density integrated from −0.1 eV to the Fermi level of $CoCp_2$ on (a) graphene/Ni(111) in top-fcc stacking, (b) graphene/Co/Ni(111), and (c) graphene/Fe/Ni(111). Left (right) panels refer to the parallel (antiparallel) configuration. The cross sectional plane, indicated as purple broken line in Figure 5.5(c) (hollow adsorption site), cuts through the Co atom and is perpendicular to both the substrate and the Cp rings.

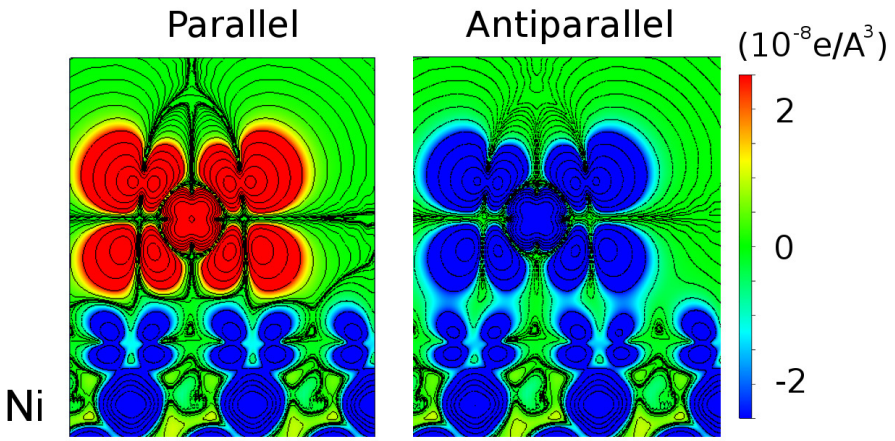

Figure 5.11.: Cross-sectional plots of the local magnetization density integrated from −0.1 eV to the Fermi level of $CoCp_2$ on graphene/Ni(111) in bridge-top stacking. Left (right) panels refer to the parallel (antiparallel) configuration.

Chapter 6.

General Conclusions

In this thesis we have performed *ab initio* calculations, within a Density Functional Theory (DFT) based methodology, of magnetic molecules in vacuum and adsorbed on magnetic substrates. The aim was to understand how well DFT could describe, help to comprehend, and, eventually, suggest possible routes toward the control of the magnetic properties of the molecules itself and the interaction with a composite graphene/ferromagnetic metal substrates. This work integrates into the research line devoted to the study of novel functional materials, as molecular magnets and hybrid organic-inorganic complexes, with possible application in spintronic devices and quantum information processing. In this respect, theoretical studies play a crucial role in supporting the experimental evidences and, with its predictive power, inspiring chemical synthesis and magnetic characterization in order to improve the functionality.

We have concentrated, concerning the isolated molecules, on the family of heterometallic Cr-based antiferromagnetic rings, and supramolecular dimeric complexes of such rings, while the molecule of choice to study the interaction with a magnetic substrate was cobaltocene. For the former study we employed a local orbital gaussians-based code, i.e. NWChem, being such methods best suited for the study of molecular non-periodic systems, while for the study of cobaltocene on magnetic substrates a plane-wave-based supercell code, i.e. VASP, was chosen. Since no experience on the use of the VASP software was present in our group, an important task of my doctorate was to learn how to use it, and most importantly, exploit at best its capabilities. This required several months, and scalability and convergence tests on the essential parameters of the simulations (e. g. number of CPUs, energy cut-off and k-point grid) have been carried out extensively. The main results of my tests are presented

in Chapter 3. Further tests using the Quantum Espresso code on the molecule-substrate magnetic interaction issues could be found in Appendix B. We summarize in the following the main scientific results obtained for the two different systems investigated during this thesis.

In Chap. 4 we investigated the magnetic properties of several magnetic molecules, namely *green*-Cr_7M rings (with M= Ni^{2+}, Mn^{2+}, Fe^{2+} and Cu^{2+}), the *purple*-Cr_7Ni and *purple*-Cr_7M/pyr/*green*-Cr_7M, supramolecular dimers (M, M' are divalent ions chosen among Ni^{2+}, Mn^{2+} and Zn^{2+}) with NWChem. This work was inspired by the many experimental and theoretical investigations that indicate this class of compound as promising candidates for magnetic information storage and processing or the implementation of quantum logic devices [17, 18, 88]. At first we calculated the exchange coupling constants Js between first-neighbor metal spins (Cr-Cr and Cr-Ni atoms) of the pristine *green*-Cr_7M rings mapping the total energies of several broken symmetry (BS) states onto a isotropic Heisenberg Hamiltonian. The values were not impressively improved compared to the ones obtained for the "pruned" structure [15], that is the structure where the pivalic bridges connecting the metal ions are replaced, for simplicity, by carboxylate bridges (approximating each $C(CH_3)_3$ complex with a single H atom). As a general finding, in the pristine structure the antiferromagnetic couplings were smaller than in the pruned structure, the ratio between J_{Cr-M} and J_{Cr-Cr} being closer to one, similarly to what is observed in experiments [29–31]. If the pruning procedure modifies both the J_{Cr-Cr} and J_{Cr-M}, the variation was larger for the latter constant. The exchange parameters obtained for the pristine *purple*-Cr_7Ni were only marginally affected by the choice of the subgroup of the BS states chosen for the solution of the linear system in the J variables. The study of heterometallic rings moved further for a different derivative, i.e. the *purple* one, where the structural asymmetry of the system allows, in the more general case, to consider four different types of exchange couplings, instead of two (as above for the *green* derivative), in the Heisenberg model Hamiltonian. We observe that (i) an increase in the number of carboxylate bridges between two ionic spins enhances the magnitude of the magnetic coupling (as expected), and (ii) the *p*-character orbitals of a O^- allow more efficient spin communication between the two ionic spins, as compared to the F^-, leading to large magnetic coupling between atoms bridged by the glucamine as compared to standard F bridges. Moreover, a detailed analysis of the intermolecular magnetic couplings in *purple*-Cr_7M/pyr/*green*-Cr_7M, supramolecular dimers with several combinations of the divalent ions M, M' on the two rings was performed, focusing on the effects produced by the systematic variation of the frontier atoms on

the coupling between the spins of the two rings. The energy differences between the antiferromagnetic-ferromagnetic (AFM-FM) configurations and the analysis of the spin polarized density show that when the Zn^{2+} ion is substituted in the purple ring and Ni^{2+} in the green ring, the magnetic communication between the two rings is completely suppressed. On the contrary, when the Zn^{2+} ion is substituted in the green ring, and Ni^{2+} in the purple ring, the antiferromagnetic coupling is kept, due to the remaining microscopic interaction between the Cr close to Zn in the green ring, and the Ni ion in the purple ring. In case of Mn and Ni substituting ions, the considerable AFM-FM energy difference produced by considering Ni^{2+} in the *purple* ring and Mn^{2+} in the *green* ring or viceversa, can be explained by the pre-multiplicative factor represented by the spin value of the substituting ion in the *purple* ring which plays a fundamental role in the mapping of the total energies on the microscopic spin Hamiltonian. The results obtained for the supramolecular rings give further insight into the propagation of spin information at the supramolecular scale. Our results on these latter dimers (Ni- and Mn-substituted) compare well with the findings obtained in specific-heat measurements performed in the group of Prof. Affronte in Modena.

The second part of this thesis was triggered by the strong interest shown by the scientific community in investigating the magnetic coupling between magnetic molecules and magnetic substrates, and on the possible routes to tailor it at will [8, 109]. Along this line, our aim was to investigate the magnetic properties of cobaltocene ($CoCp_2$) adsorbed on a graphene layer deposited on different magnetic substrates. The VASP code was employed, with PBE functional + van der Waals interactions considered within the semi-empirical potential DFT−D2 method [27]. The first substrate investigated was graphene on a slab of Ni(111). Concerning the possible stacking/registry that graphene can adopt on Ni(111), we found for the two geometries indicated as energetically favored by the literature [133], namely top-fcc and bridge-top, a binding distance between C and Ni comparable with experiments [63]. In our simulations, the top-fcc and bridge-top stacking are very close in energy but in variation with the theoretical calculations of Zhao et al. [20], we found the top-fcc stacking to be more stable as compared to the bridge-top one; this is probably only due to the employment of a different implementation of the dispersion forces [128]. The magnetic exchange coupling between the cobaltocene spin and the Ni magnetization was investigated varying separately the structure of the molecule (there are two possible, almost degenerate, structural forms with different electronic structures, with label $^2B_2$ and $^2A_2$), the stacking of graphene on the metal slab and the adsorption sites of the molecule. The switching from the $^2B_2$ to the $^2A_2$ molecular structures leads to a considerable decrease in the exchange coupling,

and could be attributed to the reduced extent of the $CoCp_2$ spin-polarized HOMO in the cyclopentadienyl rings moving from $^2B_2$ the $^2A_2$. The exchange energy was not modified in any appreciable way varying the graphene stacking from top-fcc to bridge-top, despite the remarkable change in the size of the magnetic moment induced on the graphene atoms. The adsorption site that $CoCp_2$ can attain on graphene/Ni(111) and its orientation with respect to the surface was varied in order to find the ground state adsorption geometry. The configuration with the molecule axis parallel to the graphene layer was found to be more stable than the case of perpendicular orientation, in agreement with the theoretical study of Li et al. [121]. The calculated lowest energy configuration is the one where the Co ion is aligned to a hollow site of the C hexagonal ring network of graphene. A noticeable charge transfer occurs during the adsorption process accompanied by a slight decrease of the magnetic moment of the Co ion, as compared to the molecule in the gas phase. The analysis of the binding energy suggests us that the adsorption of cobaltocene on graphene/Ni could be classified as a strong physisorption event. The main finding is that the molecular spin preferentially aligning antiparallel to the Ni magnetization. The absolute value of the exchange energy is of the order of ten meVs, and shows some variation as a function of the adsorption site, yet the interaction remaining always antiferromagnetic. Detailed analysis of the spin-polarized LDOS for the $CoCp_2$ on graphene/Ni(111) were presented, and indicate that the energy overlap between the minority states of graphene and the minority d states of $CoCp_2$ just below E_F is responsible for the stabilization of the antiparallel alignment. This energy matching is absent for the parallel alignment, due to the inverted HOMO spin polarization. We can thus conclude that the spin polarization of graphene close to E_F determines the sign of the magnetic coupling. In order to cross-check this interpretation, we studied the effect of intercalating different magnetic monolayers (Fe and Co) between graphene and the Ni(111) substrate on the magnetic interaction between the molecular spins and the magnetization of the substrate.

According to Weser et al. [21] we employed for both graphene / Fe / Ni(111) and graphene / Co / Ni(111) the top-hcp stacking. The exchange energy between $CoCp_2$ and these new substrates changes from large antiferromagnetic for graphene/Ni(111), to weak antiferromagnetic for graphene/Co/Ni(111) to weak ferromagnetic for graphene/Fe/Ni(111). As expected the obtained exchange couplings are not connected to the size of the magnetic moment of the topmost metal layer. A detailed analysis of the LDOS confirmed that also for these systems the magnetic coupling is driven by the energy matching of the spin-polarized HOMO of the $CoCp_2$ and the $2p_z$ orbitals of the graphene hybridized with the $3d$ orbitals

of the layer beneath. The plotting of cross sectional magnetization density close to the Fermi level provided a nice visual representation of this spatial and energy matching of the orbitals, both for parallel or antiparallel alignment, supporting our numerical data. Since experimentally the direct deposition of the $CoCp_2$ on a metallic surface can lead to the dissociation of the molecule [132], we simulated, as a test case, the deposition of $CoCp_2$ on Ni(111). The charge transfer observed in the graphene/Ni(111) case from $CoCp_2$ to Ni is approximately doubled when the graphene spacing layer is removed.

This is a further confirmation of the crucial role of graphene in the electronic decoupling of the molecule and the substrate, facilitating and preserving the structural integrity of such molecules. Our investigation demonstrates, for the first time, that graphene can preserve the magnetic properties of an adsorbed molecule by acting as an electronic decoupling layer but at the same time propagate the magnetic interaction to the substrate thereby stabilizing the molecular magnetic moment from temperature fluctuations under typical experimental conditions.

Although our results apply in the particular case of cobaltocene on graphene/Ni(111), their implications overreach the boundary of this specific system and could be of broad interest to the large graphene and organic spintronics communities.

Appendix A.

Methodology to extract exchange parameters from supramolecular dimers

In this Appendix the methodology that was used for the quantification of the microscopic exchange coupling parameters through the linker for the *purple*/pyr/*purple* and *purple*/pyr/*green* dimers is explained in more detail. The total Spin Hamiltonian of these dimers is composed by two different groups of exchange constants associated (i) to the intra-ring magnetic interactions mediated by the fluorine, glucamine and carboxylate bridges and (ii) to the inter-ring interaction between two spins belonging to different rings which is mediated by the INA linker. Based on the results showed in the Chapter 4 it is evident that the former are larger than the latter. It means that the transitions from the ground state to the first high-energy states concern an alteration of the magnetic communications of the metallic ions on the two sides of the INA bridge, keeping all the nearest-neighbors intra-ring communications have to be unaltered. In line with this consideration, the inter-ring exchange parameters have been obtained by retaining the AFM distribution in each of the rings (see Fig. A.1), while flipping coherently all the spins in one of the ring in order to change the total spin of the dimer.

The microscopic spin Hamiltonian for the *purple*-Cr_7Ni/pyr/*purple*-Cr_7Ni is represented in the Equation A.1, and just two different projected BS configurations are necessary to achieve the J_{Ni-Ni} value (FM and AFM states sketched in Fig. A.1(a)).

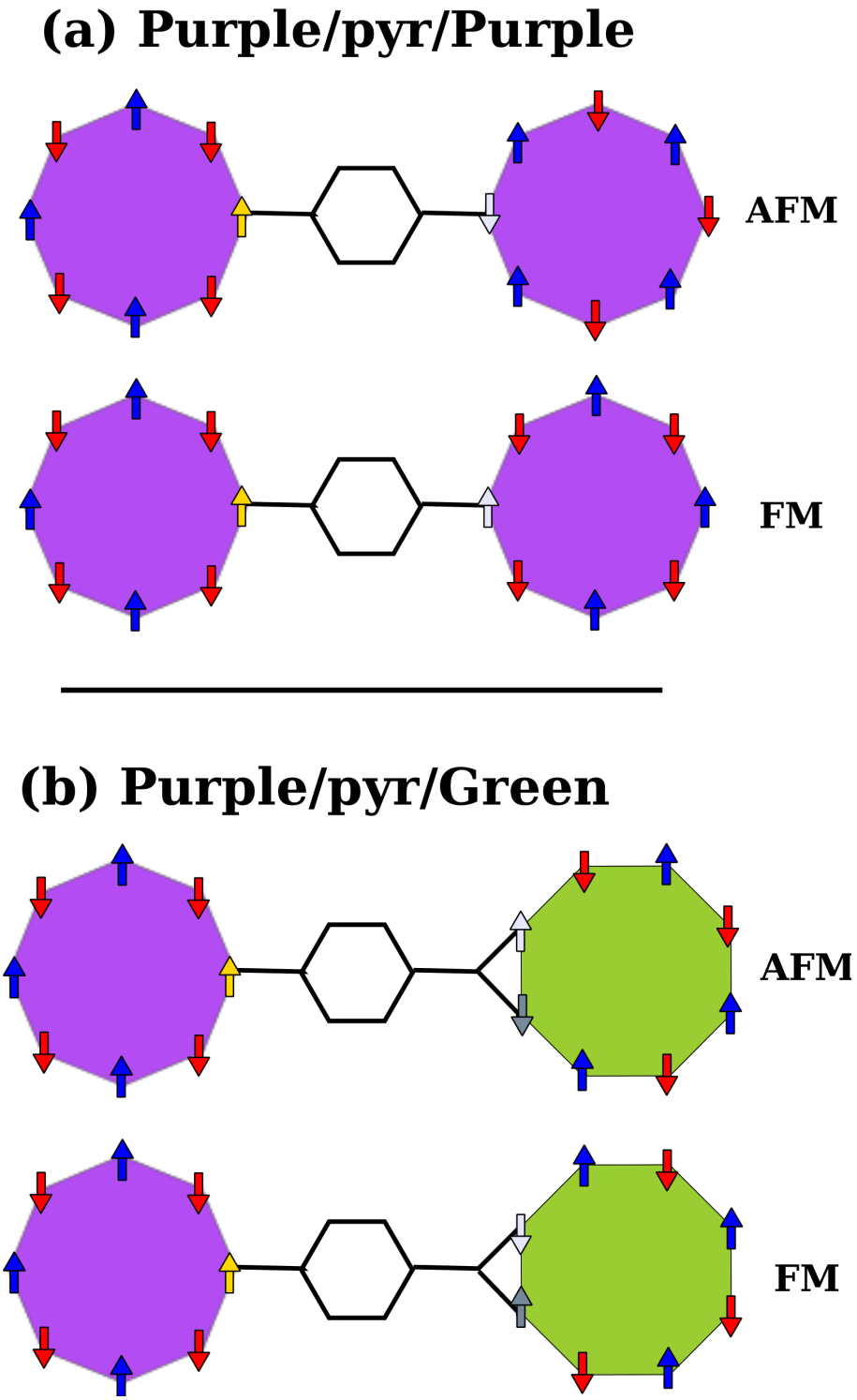

Figure A.1.: Schematic representation of the ferromagnetic (FM) and antiferromagnetic (AFM) states for (a) the *purple*-Cr_7M/pyr/*purple*-Cr_7M, dimer and (b) the *purple*-Cr_7M/pyr/*green*-Cr_7M, dimer. The spin polarized Cr^{3+} ions are represented as blue (up) and red (down) arrows while the replaceable positions in the two families of molecules are depicted as gold, silver and gray arrows.

$$E^{TOT} = E_0 - J_{Ni-Ni}\mathbf{s}_z^{Ni}\mathbf{s}_z^{Ni} \tag{A.1}$$

As mentioned in Section 4.3.3 in the case of *purple*/pyr/*green* dimers, two exchange parameters are necessary to describe the magnetic coupling through the linker. Therefore the only knowledge of the total energies of FM and AFM state is insufficient (sketch is depicted in Fig. A.1(b)). In an attempt to split this problem an intermediate system with a Zn^{2+} ion (s=0) on the *green* ring was built. From the FM and AFM total energies of this intermediary system it can be extracted one of the two exchange coupling parameters, i.e. the M-Cr one, necessary to solve the whole microscopic spin Hamiltonian. Here, for the sake of completeness the resolution of the *purple*-Cr_7Mn/pyr/*green*-Cr_7Ni case will be presented. In Equation A.2 is represented the microscopic spin Hamiltonian of the intermediate *purple*-Cr_7Mn/pyr/*green*-Cr_7Zn dimer.

$$E^{TOT} = E_0 - J_{Mn-Cr}\mathbf{s}_z^{Mn}\mathbf{s}_z^{Cr} \tag{A.2}$$

A total energy difference $E_{AFM} - E_{FM} = -0.58$ meV was found. The J_{Mn-Cr}, describing the magnetic coupling between the Mn^{2+} (s=5/2) and the Cr^{3+} (s=3/2), was obtained by the solution of the following linear system:

$$\begin{cases} E_{AFM} = E_0 + 15/4 J_{Mn-Cr} \\ E_{FM} = E_0 - 15/4 J_{Mn-Cr} \end{cases} \Rightarrow J_{Mn-Cr} = -0.08 \text{ meV} \tag{A.3}$$

The J_{Mn-Cr} was then used in the microscopic spin Hamiltonian of the *purple*-Cr_7Mn/pyr/*green*-Cr_7Ni dimer:

$$E^{TOT} = E_0 - J_{Mn-Cr}\mathbf{s}_z^{Mn}\mathbf{s}_z^{Cr} - J_{Mn-Ni}\mathbf{s}_z^{Mn}\mathbf{s}_z^{Ni} \tag{A.4}$$

From the knowledge of the total energy difference $E_{AFM} - E_{FM} = -0.92$ meV in this dimer, the missing parameter J_{Mn-Ni}, describing the magnetic coupling between the Mn^{2+} (s=5/2) and the Ni^{2+} (s=1), was obtained:

$$\begin{cases} E_{AFM} = E_0 + 15/4 J_{Mn-Cr} - 5/2 J_{Mn-Ni} \\ E_{FM} = E_0 - 15/4 J_{Mn-Cr} + 5/2 J_{Mn-Ni} \end{cases} \Rightarrow J_{Mn-Ni} = 0.07 \text{ meV} \qquad \text{(A.5)}$$

A similar procedure was applied to map the microscopic spin Hamiltonian for all the dimers of the *purple*/pyr/*green* family.

Appendix B.

Comparison with Quantum Espresso

In this Appendix we present some tests calculations performed on the cobaltocene on Graphene/Ni scientific issue discussed in Chap. 5. More precisely, in order to validate our VASP results, we carried out some of the calculations discussed there by employing a different numerical, open-source, code, namely Quantum Espresso (QE). Along with comparing the results obtained by the two numerical codes we will also provide a thorough analysis of the scaling performances of QE as compared to the VASP code.

Most simulations that have been shown in this thesis were made on the FERMI supercomputer at the CINECA laboratory.

The FERMI computer has a Blue Gene architecture which consists in having thousands of cores with limited memory supplies (1GB). Codes developed for full-atomistic simulations (VASP included) have been instead wrote initially for machines with lower number of cores, higher clock frequency and large memory size per core (as for instance IBM-SP machines). Therefore they can scale linearly only up to hundreds of processes and they can not take advantage of the whole resources offered by a blue-gene architecture (several thousands of processors available for a single run). Currently, in order to exploit the full potentials of this architecture, the best parallel programming model is the hybrid MPI/OpenMP. The OpenMP [134] is an application programming interface for the implementation of multithreading, in simple terms it allows to split a single MPI process in several subprocesses that share the same RAM, with benefits for the occupied memory and the calculation speed. Many developers are migrating their software in accordance to these new needs. In this migration QE [135] is particularly ahead with respect to other ab initio simulation packages like VASP, because it was designed from scratch for a high level scalability. QE collects a

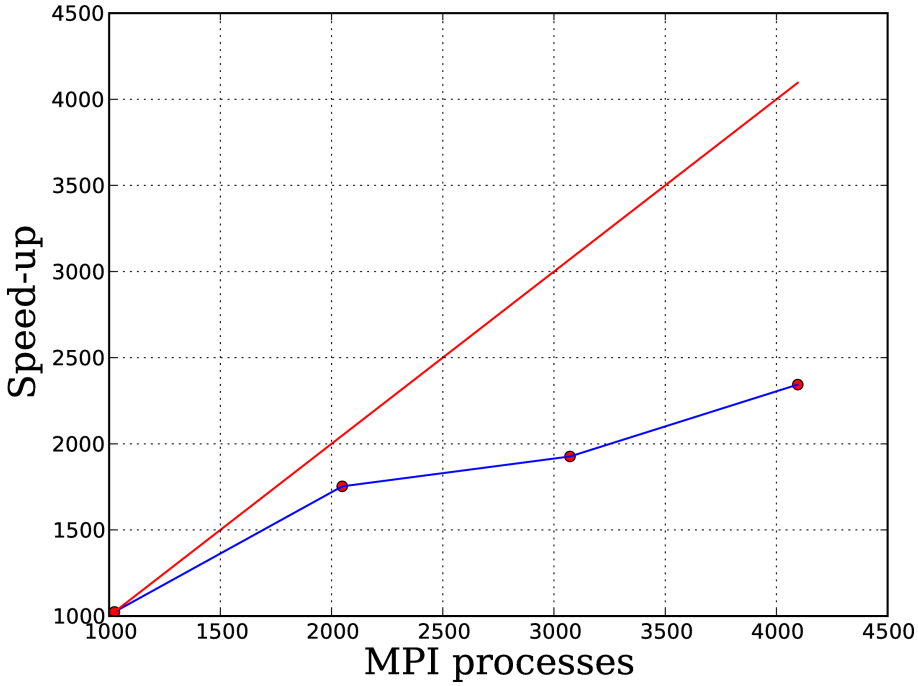

Figure B.1.: Scalability for large-scale calculations: speed-up as a function of the number of cores. The system is a molecule of $CoCp_2$ adsorbed on a graphene/Ni(111) surface, 5 k-points, 171 atoms, on a Blue Gene Q.

wide groups of open-source computer codes for electronic structure calculations, it is based on the density functional theory and works with plane waves and pseudopotentials. Among the many packages it contains (ground-state calculation, ab initio molecular dynamics, many-body perturbation theory, just to cite some of them). We benchmarked QE on the Fermi machine for the $CoCp_2$ on graphene/Ni(111) system. As demonstrate in Figure B.1 QE shows a nice scalability up to 4000 MPI processes.

The improvements due to the OpenMP application can be observed in Figure B.2. The number of threads was increased up to 4, according to the maximum number of multiple threads efficiently supported by the Blue Gene Q cores. The speed-up produced by the multithreading is not larger as the one due to the MPI scaling, but it allows to decrease both the wall time of 35 % and the occupied RAM per processor, giving the chance to simulate larger systems without increasing the number of processors. Several others input parameters can be tuned in order to give minor improvements on the total speed. Among them is important to mention the good acceleration obtained by distributing and parallelizing the matrix diagonalization and the matrix-matrix multiplications on a N $\times$ N MPI processes grid. N can be tuned in the input file through the *ndiag* variable (*ndiag*=N). Figure B.3

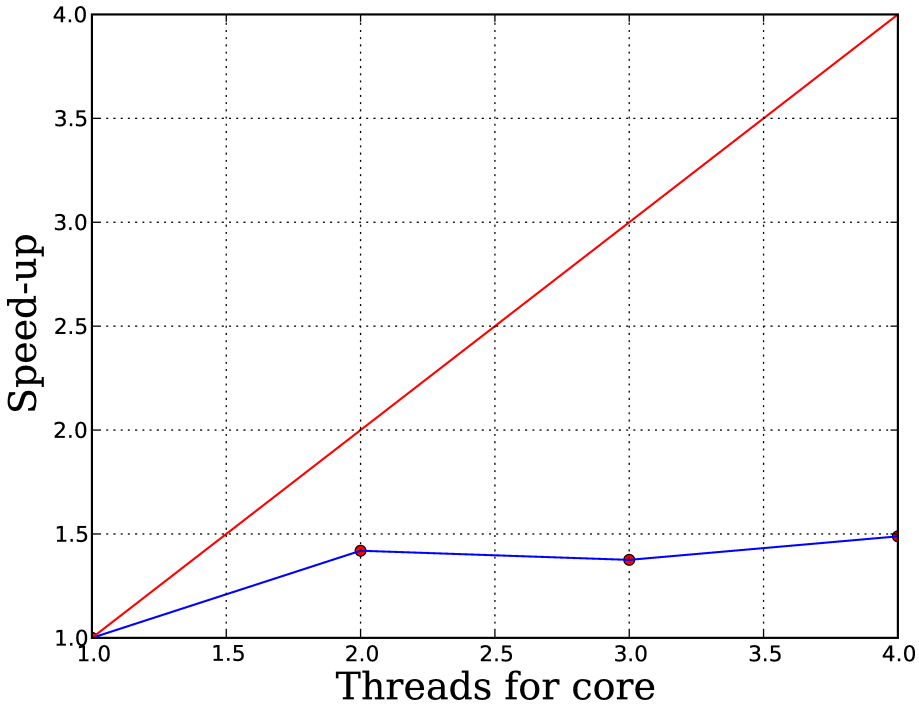

Figure B.2.: Scalability for large-scale calculations: speed-up as a function of the number of threads per core. All the simulations were calculated on 1024 MPI processes. The system is a molecule of $CoCp_2$ adsorbed on a graphene/Ni(111) surface, 5 k-points, 171 atoms, on a Blue Gene Q.

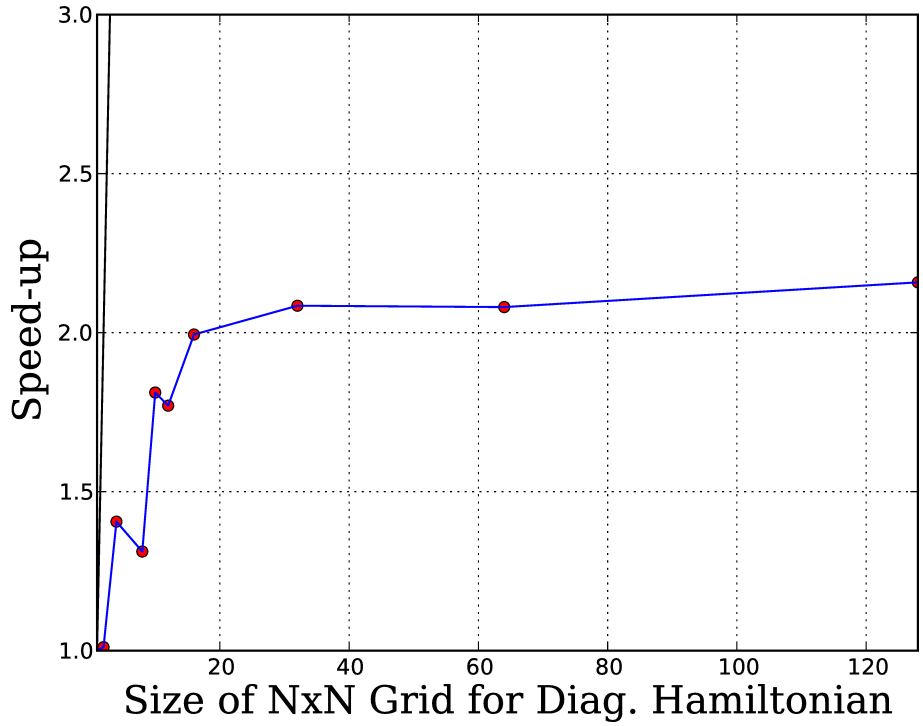

Figure B.3.: Scalability for large-scale calculations: speed-up as a function of the N × N grid size used to parallelize the Hamiltonian diagonalization. All the simulations were calculated on 1024 MPI processes. The system is a molecule of $CoCp_2$ adsorbed on a graphene/Ni(111) surface, 5 k-points, 171 atoms, on a Blue Gene Q.

shows how an accurate choice of this parameter can double the calculation speed. In this last test we employed 1024 MPI processors and indeed the speed-up shows an increasing trend up to a grid of $32 \times 32 = 1024$ MPI processes, but not over. This is because QE can not exploit a grid bigger than the total number of MPI processes.

The main difference between VASP and QE stands in the building of the PAW pseudopotentials. In the QE simulations we used the pseudopotentials H.pbe-kjpaw_psl.0.1.UPF, C.pbe-n-kjpaw_psl.0.1.UPF, Ni.pbe-n-kjpaw_psl.0.1.UPF, Co.pbe-n-kjpaw_psl.0.2.3.UPF and Fe.pbe-spn-kjpaw_psl.0.2.1.UPF from http://www.quantum-espresso.org. In order to show the differences in PAW implementations, we did not relax the atomic coordinates with QE, but we considered the ones obtained by VASP; moreover, for better comparison, we also used the same k-point grid obtained by VASP. Even though most of the PAW pseudopotentials of QE have been used with satisfactory results in published work it is always necessary to check the absolute convergence respect to the quantity of interest. In our case the convergence of the E_{ex} was checked increasing the energy cut-off. The tests for

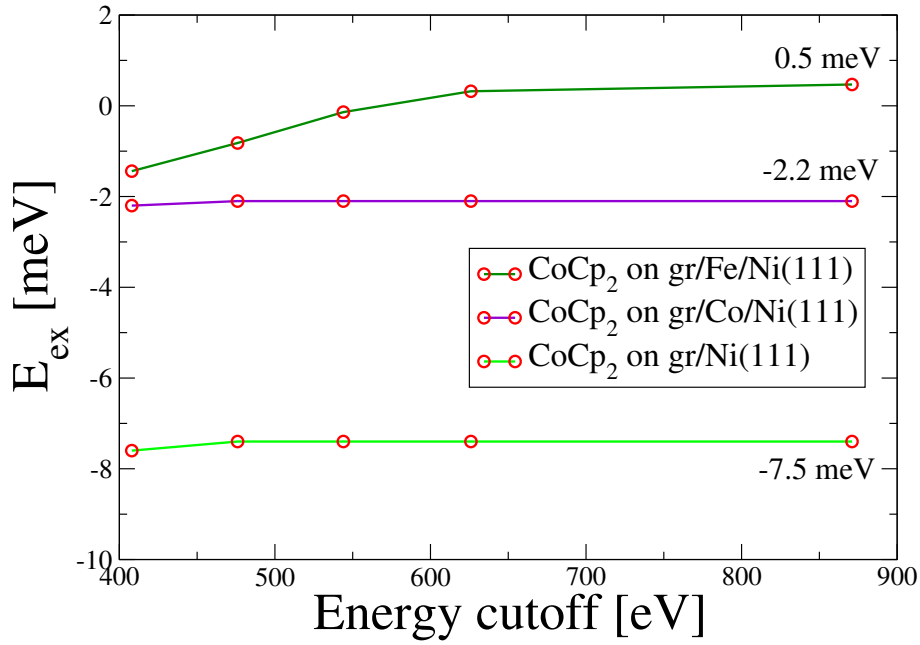

Figure B.4.: Magnetic coupling convergence with respect to the energy cut-off, tested for $CoCp_2$ on graphene/M/Ni(111) (M=Ni, Fe, Co).

the $CoCp_2$ on graphene/M/Ni(111) with M= Fe, Co, Ni are shown in Figure B.4. For the case of the Ni and Co monolayers the convergence was already achieved at 400 eV (the same value used in the VASP calculations), while for the Fe case was necessary to reach 600 eV to obtain stable values. In this last case high level of convergence was crucial to reproduce the positive value of E_{ex} previously found with VASP; indeed moving from 400 to 600 eV the E_{ex} changes more than 1 meV, and reverses its sign. A general comparison of the E_{ex} values obtained by VASP (see Table 5.4) and QE (see Figure B.4) confirms a gradual change from antiferromagnetic to ferromagnetic, moving from Ni, Co and finally Fe. The E_{ex} calculated with QE for the Ni and the Fe monolayers are systematically smaller of ~ 2 meV respect to the values obtained with VASP ($-7.5/-9.7$ meV for Ni and 0.5/2.0 meV for Fe, respectively for QE/VASP), while for the Co case the exchange parameters are almost identical, $-2.2/-2.3$ meV. In this last case VASP and QE bring to the same value and the convergence is already achieved with an energy cut-off of 400 eV. These tests demonstrated that, a part from a small variation in the absolute value of the obtained exchange energies, the trend observed intercalating the Fe and Co monolayers below graphene is robust, and very similar results are obtained by two codes.

Bibliography

[1] G. Timco, E. McInnes, R. Pritchard, F. Tuna, and R. Winpenny, "Heterometallic rings made from chromium stick together easily," *Angew. Chem.*, vol. 120, pp. 9827–9830, 2008.

[2] F. K. Larsen, E. J. L. McInnes, H. E. Mkami, J. Overgaard, S. Piligkos, G. Rajaraman, E. Rentschler, A. A. Smith, G. M. Smith, V. Boote, M. Jennings, G. A. Timco, and R. E. P. Winpenny, "Synthesis and characterization of heterometallic Cr_7M wheels," *Angew. Chem.*, vol. 42, pp. 101–105, 2003.

[3] A. Cornia, A. C. Fabretti, M. Pacchioni, L. Zobbi, D. Bonacchi, A. Caneschi, D. Gatteschi, R. Biagi, U. Del Pennino, V. De Renzi, L. Gurevich, and H. S. J. Van der Zant, "Direct observation of single-molecule magnets organized on gold surfaces," *Angew. Chem. Int. Ed.*, vol. 42, no. 14, pp. 1645–1648, 2003.

[4] A. Ghirri, V. Corradini, V. Bellini, R. Biagi, U. del Pennino, V. De Renzi, J. C. Cezar, C. A. Muryn, G. A. Timco, R. E. P. Winpenny, and M. Affronte, "Self-Assembled Monolayer of Cr_7Ni Molecular Nanomagnets by Sublimation," *ACS Nano*, vol. 5, no. 9, p. 7090, 2011.

[5] V. Corradini, F. Moro, R. Biagi, U. del Pennino, V. De Renzi, S. Carretta, P. Santini, M. Affronte, J. C. Cezar, G. Timco, and R. E. P. Winpenny, "X-ray magnetic circular dichroism investigation of spin and orbital moments in Cr_8 and Cr_7Ni antiferromagnetic rings ," *Phys. Rev. B*, vol. 77, p. 014402, Jan 2008.

[6] V. Corradini, A. Ghirri, E. Garlatti, R. Biagi, V. De Renzi, U. del Pennino, V. Bellini, S. Carretta, P. Santini, G. Timco, R. E. P. Winpenny, and M. Affronte, "Magnetic anisotropy of Cr_7Ni spin clusters on surfaces," *Adv. Funct. Mater.*, vol. 22, no. 17, pp. 3706–3713, 2012.

[7] E. Annese, F. Casolari, J. Fujii, and G. Rossi, "Interface magnetic coupling of Fe-

phthalocyanine layers on a ferromagnetic surface," *Phys. Rev. B*, vol. 87, p. 054420, 2013.

[8] H. Wende, M. Bernien, J. Luo, C. Sorg, N. Ponpandian, J. Kurde, J. Miguel, M. Piantek, X. Xu, P. Eckhold, W. Kuch, K. Baberschke, P. M. Panchmatia, B. Sanyal, P. M. Oppeneer, and O. Eriksson, "Substrate-induced magnetic ordering and switching of iron porphyrin molecules," *Nat. Mater.*, vol. 6, p. 516, 2007.

[9] C. F. Hermanns, K. Tarafder, M. Bernien, A. Krüger, Y.-M. Chang, P. M. Oppeneer, and W. Kuch, "Magnetic coupling of porphyrin molecules through graphene," *Adv. Materials*, vol. 25, no. 25, pp. 3473–3477, 2013.

[10] J. Schwöbel, Y. Fu, J. Brede, A. Dilullo, G. Hoffmann, S. Klyatskaya, M. Ruben, and R. Wiesendanger, "Real-space observation of spin-split molecular orbitals of adsorbed single-molecule magnets," *Nat. Commun.*, vol. 3, p. 953, 2012.

[11] M. J. Rodriguez-Douton, M. Mannini, L. Armelao, A.-L. Barra, E. Tancini, R. Sessoli, and A. Cornia, "One-step covalent grafting of Fe_4 single-molecule magnet monolayers on gold," *Chem. Commun.*, vol. 47, pp. 1467–1469, 2011.

[12] F. Moro, V. Corradini, M. Evangelisti, V. D. Renzi, R. Biagi, U. d. Pennino, C. J. Milios, L. F. Jones, and E. K. Brechin, "Grafting Derivatives of Mn_6 Single-Molecule Magnets with High Anisotropy Energy Barrier on Au(111) Surface," *J. Phys. Chem. B*, vol. 112, no. 32, pp. 9729–9735, 2008, http://pubs.acs.org/doi/pdf/10.1021/jp802195x. PMID: 18646796.

[13] F. Totti, G. Rajaraman, M. Iannuzzi, and R. Sessoli, "Computational Studies on SAMs of Mn_6 SMMs on Au(111): Do Properties Change upon Grafting?," *J. Phys. Chem. C*, vol. 117, no. 14, pp. 7186–7190, 2013, http://pubs.acs.org/doi/pdf/10.1021/jp4009916.

[14] V. Corradini, F. Moro, R. Biagi, V. De Renzi, U. del Pennino, V. Bellini, S. Carretta, P. Santini, V. A. Milway, G. Timco, R. E. P. Winpenny, and M. Affronte, "Successful grafting of isolated molecular Cr_7Ni rings on Au(111) surface," *Phys. Rev. B*, vol. 79, p. 144419, Apr 2009.

[15] V. Bellini and M. Affronte, "A density-functional study of heterometallic Cr-based molecular rings," *J. Phys. Chem. B*, vol. 114, no. 46, pp. 14797–14806, 2010.

[16] F. Troiani, V. Bellini, and M. Affronte, "Decoherence induced by hyperfine interactions

with nuclear spins in antiferromagnetic molecular rings," *Phys. Rev. B*, vol. 77, p. 054428, Feb 2008.

[17] V. Bellini, G. Lorusso, A. Candini, W. Wernsdorfer, T. B. Faust, G. A. Timco, R. E. P. Winpenny, and M. Affronte, "Propagation of spin information at the supramolecular scale through heteroaromatic linkers," *Phys. Rev. Lett.* , vol. 106, p. 227205, Jun 2011.

[18] A. Candini, G. Lorusso, F. Troiani, A. Ghirri, S. Carretta, P. Santini, G. Amoretti, C. Muryn, F. Tuna, G. Timco, E. J. L. McInnes, R. E. P. Winpenny, W. Wernsdorfer, and M. Affronte, "Entanglement in supramolecular spin systems of two weakly coupled antiferromagnetic rings (purple-$\mathbf{Cr}_7$Ni)," *Phys. Rev. Lett.* , vol. 104, p. 037203, Jan 2010.

[19] Z. Xu, Y. Xie, W. Feng, and H. Schaefer III, "Systematic investigation of electronic and molecular structures for the first transition metal series metallocenes $M(C_5H_5)_2$ (M= V, Cr, Mn, Fe, Co, and Ni)," *J. Phys. Chem. A*, vol. 107, no. 15, p. 2716, 2003.

[20] W. Zhao, S. M. Kozlov, O. Höfert, K. Gotterbarm, M. P. A. Lorenz, F. Viñes, C. Papp, A. Görling, and H.-P. Steinrück, "Graphene on Ni(111): Coexistence of Different Surface Structures," *J. Phys. Chem. Lett.* , vol. 2, no. 7, p. 759, 2011.

[21] M. Weser, E. N. Voloshina, K. Horn, and Y. S. Dedkov, "Electronic structure and magnetic properties of the graphene/Fe/Ni(111) intercalation-like system.," *Phys. Chem. Chem. Phys.*, vol. 13, no. 16, p. 7534, 2011.

[22] G. Kresse and D. Joubert, "From ultrasoft pseudopotentials to the projector augmented-wave method," *Phys. Rev. B*, vol. 59, p. 1758, 1999.

[23] M. Valiev, E. J. Bylaska, N. Govind, K. Kowalski, T. P. Straatsma, H. J. J. Van Dam, D. Wang, J. Nieplocha, E. Apra, T. L. Windus, *et al.*, "NWChem: A comprehensive and scalable open-source solution for large scale molecular simulations," *Comp. Phys. Commun.*, vol. 181, no. 9, pp. 1477–1489, 2010.

[24] Q. Wu and T. Van Voorhis, "Direct optimization method to study constrained systems within density-functional theory," *Phys. Rev. A*, vol. 72, p. 024502, Aug 2005.

[25] I. Rudra, Q. Wu, and T. Van Voorhis, "Accurate magnetic exchange couplings in transition-metal complexes from constrained density-functional theory,"

J. Chem. Phys. , vol. 124, p. 024103, Jan. 2006.

[26] P. E. Blöchl, "Projector augmented-wave method," *Phys. Rev. B*, vol. 50, p. 17953, 1994.

[27] S. Grimme, "Semiempirical GGA-type density functional constructed with a long-range dispersion correction," *J. Comp. Chem.* , vol. 27, no. 15, p. 1787, 2006.

[28] S. L. Dudarev, G. A. Botton, S. Y. Savrasov, C. J. Humphreys, and A. P. Sutton, "Electron-energy-loss spectra and the structural stability of nickel oxide: An LSDA+U study," *Phys. Rev. B*, vol. 57, no. 3, p. 1505, 1998.

[29] R. Caciuffo, T. Guidi, G. Amoretti, S. Carretta, E. Liviotti, P. Santini, C. Mondelli, G. Timco, C. A. Muryn, and R. E. P. Winpenny, "Spin dynamics of heterometallic Cr_7M wheels (M = Mn, Zn, Ni) probed by inelastic neutron scattering," *Phys. Rev. B*, vol. 71, p. 174407, May 2005.

[30] M. Allalen and J. Schnack, "Theoretical estimates for proton-NMR spinlattice relaxation rates of heterometallic spin rings," *J. Magn. Magn. Materials*, vol. 302, no. 1, pp. 206–210, 2006.

[31] H. Amiri, M. Mariani, A. Lascialfari, F. Borsa, G. A. Timco, F. Tuna, and R. E. P. Winpenny, "Magnetic properties and spin dynamics in the Cr_7Fe nanomagnet: A heterometallic antiferromagnetic molecular ring," *Phys. Rev. B*, vol. 81, p. 104408, Mar 2010.

[32] M. Born and J. M. Oppenheimer, "Zur quantentheorie der molekeln," *Ann. Phys.*, vol. 84, p. 457, 1927.

[33] P. Hohenberg and W. Kohn, "Inhomogeneous electron gas," *Phys. Rev.*, vol. 136, pp. B864–B871, Nov 1964.

[34] L. H. Thomas, "The calculation of atomic fields," *Proc. Cambridge Philos.*, vol. 23, pp. 542–548, 1 1927.

[35] E. Fermi, "Eine statistische methode zur bestimmung einiger eigenschaften des atoms und ihre anwendung auf die theorie des periodischen systems der elemente," *Z. Physik*, vol. 48, no. 1-2, pp. 73–79, 1928.

[36] P. A. M. Dirac, "Note on exchange phenomena in the thomas atom," *Proc. Cambridge*

Philos., vol. 26, pp. 376–385, 7 1930.

[37] W. Kohn and L. J. Sham, "Self-consistent equations including exchange and correlation effects," *Phys. Rev.*, vol. 140, pp. A1133–A1138, Nov 1965.

[38] R. P. Feynman, *Statistical Mechanics*. Benjamin Publishing Company Reading, 1972.

[39] H. Hellmann, *Einführung in die Quantenchemie*. Franz Deuticke, 1937.

[40] R. P. Feynman, "Forces in molecules," *Phys. Rev.*, vol. 56, pp. 340–343, Aug 1939.

[41] R. Dreizler and E. Gross, *Density Functional Theory: An Approach to the Quantum Many-Body Problem*. Springer-Verlag, 1990.

[42] D. M. Ceperley and B. J. Alder, "Ground state of the electron gas by a stochastic method," *Phys. Rev. Lett.* , vol. 45, pp. 566–569, Aug 1980.

[43] J. P. Perdew and A. Zunger, "Self-interaction correction to density-functional approximations for many-electron systems," *Phys. Rev. B*, vol. 23, pp. 5048–5079, May 1981.

[44] J. P. Perdew, K. Burke, and M. Ernzerhof, "Generalized gradient approximation made simple," *Phys. Rev. Lett.* , vol. 77, p. 3865, 1996.

[45] A. D. Becke, "Density-functional exchange-energy approximation with correct asymptotic behavior," *Phys. Rev. A*, vol. 38, pp. 3098–3100, Sep 1988.

[46] C. Lee, W. Yang, and R. G. Parr, "Development of the Colle-Salvetti correlation-energy formula into a functional of the electron density," *Phys. Rev. B*, vol. 37, pp. 785–789, Jan 1988.

[47] C. A. Ullrich, U. J. Gossmann, and E. K. U. Gross, "Time-dependent optimized effective potential," *Phys. Rev. Lett.* , vol. 74, pp. 872–875, Feb 1995.

[48] S. Kümmel and J. P. Perdew, "Simple iterative construction of the optimized effective potential for orbital functionals, including exact exchange," *Phys. Rev. Lett.* , vol. 90, p. 043004, Jan 2003.

[49] A. D. Becke, "A new mixing of hartree-fock and local density-functional theories," *J. Chem. Phys.* , vol. 98, pp. 1372–1377, jan 1993.

[50] J. P. Perdew, E. M., and K. Burke, "Rationale for mixing exact exchange with density

functional approximations," *J. Chem. Phys.* , vol. 105, pp. 9982–9985, dec 1996.

[51] C. C. J. Roothaan, "New developments in molecular orbital theory," *Rev. Mod. Phys.*, vol. 23, pp. 69–89, Apr 1951.

[52] E. Ruiz, P. Alemany, S. Alvarez, and J. Cano, "Toward the Prediction of Magnetic Coupling in Molecular Systems: Hydroxo- and Alkoxo-Bridged Cu(II) Binuclear Complexes," *J. Am. Chem. Soc.*, vol. 119, no. 6, pp. 1297–1303, 1997, http://pubs.acs.org/doi/pdf/10.1021/ja961199b.

[53] S. H. Vosko, L. Wilk, and M. Nusair, "Accurate spin-dependent electron liquid correlation energies for local spin density calculations: a critical analysis," *Can. J. Phys.*, vol. 58, no. 8, pp. 1200–1211, 1980, http://www.nrcresearchpress.com/doi/pdf/10.1139/p80-159.

[54] F. Cinquini, L. Giordano, G. Pacchioni, A. M. Ferrari, C. Pisani, and C. Roetti, "Electronic structure of NiOAg(100) thin films from DFT + U and hybrid functional dft approaches," *Phys. Rev. B*, vol. 74, p. 165403, Oct 2006.

[55] C. Adamo, V. Barone, A. Bencini, F. Totti, and I. Ciofini, "On the Calculation and Modeling of Magnetic Exchange Interactions in Weakly Bonded Systems: The Case of the Ferromagnetic Copper(II) μ2-Azido Bridged Complexes," *Inorg. Chem.*, vol. 38, no. 9, pp. 1996–2004, 1999, http://pubs.acs.org/doi/pdf/10.1021/ic9812306.

[56] M. C. Payne, M. P. Teter, D. C. Allan, T. A. Arias, and J. D. Joannopoulos, "Iterative minimization techniques for *ab initio* total-energy calculations: molecular dynamics and conjugate gradients," *Rev. Mod. Phys.*, vol. 64, pp. 1045–1097, Oct 1992.

[57] N. Troullier and J. L. Martins, "Efficient pseudopotentials for plane-wave calculations," *Phys. Rev. B*, vol. 43, pp. 1993–2006, Jan 1991.

[58] G. Kresse and J. Furthmüller, "Efficient iterative schemes for ab initio total-energy calculations using a plane-wave basis set," *Phys. Rev. B*, vol. 54, p. 11169, 1996.

[59] O. K. Andersen, "Simple approach to the band-structure problem," *Solid State Commun.*, vol. 13, no. 2, pp. 133–136, 1973.

[60] H.-L. Sun, Z.-M. Wang, and S. Gao, "Strategies towards single-chain magnets," *Coord. Chem. Rev.*, vol. 254, no. 9, pp. 1081–1100, 2010.

[61] S. J. Gong, Z. Y. Li, Z. Q. Yang, C. Gong, C.-G. Duan, and J. H. Chu, "Spintronic properties of graphene films grown on Ni(111) substrate," *Journal of Applied Physics*, vol. 110, no. 4, p. 043704, 2011.

[62] J. Klimeš, D. Bowler, and A. Michaelides, "Van der Waals density functionals applied to solids," *Phys. Rev. B*, vol. 83, p. 195131, May 2011.

[63] Y. Gamo, A. Nagashima, M. Wakabayashi, and M. Terai, "Atomic structure of monolayer graphite formed on Ni (111)," *Surf. Sci.* , vol. 374, p. 61, Mar. 1997.

[64] H. J. Monkhorst and J. D. Pack, "Special points for brillouin-zone integrations," *Phys. Rev. B*, vol. 13, pp. 5188–5192, Jun 1976.

[65] J. Moreno and J. M. Soler, "Optimal meshes for integrals in real- and reciprocal-space unit cells," *Phys. Rev. B*, vol. 45, pp. 13891–13898, Jun 1992.

[66] T. Lis, "Preparation, structure, and magnetic properties of a dodecanuclear mixed-valence manganese carboxylate," *Acta Cryst. B*, vol. 36, pp. 2042–2046, 1980.

[67] J. R. Friedman, M. P. Sarachik, J. Tejada, and R. Ziolo, "Macroscopic measurement of resonant magnetization tunneling in high-spin molecules," *Phys. Rev. Lett.* , vol. 76, no. 20, pp. 3830–3833, 1996.

[68] A. Caneschi, D. Gatteschi, R. Sessoli, A. L. Barra, L. C. Brunel, and M. Guillot, "Alternating current susceptibility, high field magnetization, and millimeter band EPR evidence for a ground S= 10 state in $[Mn_{12}O_{12}(Ch_3COO)_{16}(H_2O)_4]_2CH_3COOH_4H_2O$," *J. Am. Chem. Soc.*, vol. 113, pp. 5873–5874, 1991.

[69] T. Kawamoto, Y. Asai, and S. Abe, "Novel mechanism of photoinduced reversible phase transitions in molecule-based magnets," *Phys. Rev. Lett.* , vol. 86, pp. 348–351, Jan 2001.

[70] P. Gütlich and H. Goodwin, *Spin Crossover in Transition Metal Compounds II.* Spin Crossover in Transition Metal Compounds, Springer, 2004.

[71] G. L. Abbati, A. Cornia, A. C. Fabretti, W. Malavasi, L. Schenetti, A. Caneschi, and D. Gatteschi, "Modulated magnetic coupling in alkoxoiron (iii) rings by host-guest interactions with alkali metal cations," *Inorg. Chem.*, vol. 36, no. 27, pp. 6443–6446, 1997.

[72] M. Affronte, J. C. Lasjaunias, A. Cornia, and A. Caneschi, "Low-temperature specific heat of Fe_6 and Fe_{10} molecular magnets," *Phys. Rev. B*, vol. 60, no. 2, p. 1161, 1999.

[73] K. L. Taft, C. D. Delfs, G. C. Papaefthymiou, S. Foner, D. Gatteschi, and S. J. Lippard, "$[Fe(OMe)_2(O_2CCH_2Cl)]_{10}$, a molecular ferric wheel," *J. Am. Chem. Soc.*, vol. 116, no. 3, pp. 823–832, 1994.

[74] E. Micotti, Y. Furukawa, K. Kumagai, S. Carretta, A. Lascialfari, F. Borsa, G. Timco, and R. E. P. Winpenny, "Local spin moment distribution in antiferromagnetic molecular rings probed by NMR," *Phys. Rev. Lett.* , vol. 97, no. 26, p. 267204, 2006.

[75] F. Borsa, A. Lascialfari, and Y. Furukawa, "NMR in magnetic molecular rings and clusters," in *Novel NMR and EPR techniques*, pp. 297–349, Springer, 2006.

[76] S. Carretta, J. Van Slageren, T. Guidi, E. Liviotti, C. Mondelli, D. Rovai, A. Cornia, A. L. Dearden, F. Carsughi, M. Affronte, *et al.*, "Microscopic spin hamiltonian of a Cr_8 antiferromagnetic ring from inelastic neutron scattering," *Phys. Rev. B*, vol. 67, no. 9, p. 094405, 2003.

[77] S. Blundell, *Magnetism in Condensed Matter*. Oxford University Press, 2001.

[78] A. Liechtenstein, M. Katsnelson, V. Antropov, and V. Gubanov, "Local spin density functional approach to the theory of exchange interactions in ferromagnetic metals and alloys," *J. Magn. Magn. Materials*, vol. 67, no. 1, pp. 65–74, 1987.

[79] Z. Zeng, D. Guenzburger, and D. E. Ellis, "Electronic structure, spin couplings, and hyperfine properties of nanoscale molecular magnets," *Phys. Rev. B*, vol. 59, pp. 6927–6937, Mar 1999.

[80] V. A. Gubanov and D. E. Ellis, "Magnetic transition-state approach to antiferromagnetic ordering: Nio," *Phys. Rev. Lett.* , vol. 44, pp. 1633–1636, Jun 1980.

[81] K. Park and M. R. Pederson, "Effect of extra electrons on the exchange and magnetic anisotropy in the anionic single-molecule magnet Mn_{12}," *Phys. Rev. B*, vol. 70, p. 054414, Aug 2004.

[82] J. Kortus, C. S. Hellberg, and M. R. Pederson, "Hamiltonian of the V_{15} spin system from first-principles density-functional calculations," *Phys. Rev. Lett.* , vol. 86, pp. 3400–3403, Apr 2001.

[83] D. W. Boukhvalov, V. V. Dobrovitski, M. I. Katsnelson, A. I. Lichtenstein, B. N. Harmon, and P. Kögerler, "Electronic structure and exchange interactions in V_{15} magnetic molecules: LDA+U results," *J. Appl. Physics*, vol. 93, no. 10, pp. 7080–7082, 2003.

[84] A. V. Postnikov, J. Kortus, and S. Bluegel, "Ab initio simulations of Fe-based ferric wheels," *arXiv preprint cond-mat/0307292*, 2003.

[85] A. Bencini and F. Totti, "DFT description of the magnetic structure of polynuclear transition-metal clusters: The complexes $[\{Cu(bpca)_2(H_2O)_2\}\{Cu(NO_3)_2\}_2]$, (bpca = Bis(2-pyridylcarbonyl)amine), and $[Cu(DBSQ)(C_2H_5O)]_2$, (DBSQ = 3,5-di-tert-butyl-semiquinonato)," *Intern. J. Quantum. Chem.*, vol. 101, no. 6, pp. 819–825, 2005.

[86] I. Rudra, Q. Wu, and T. Van Voorhis, "Predicting exchange coupling constants in frustrated molecular magnets using density functional theory," *Inorg. Chem.*, vol. 46, no. 25, pp. 10539–10548, 2007, http://pubs.acs.org/doi/pdf/10.1021/ic700871f. PMID: 17999488.

[87] A. Chiesa, S. Carretta, P. Santini, G. Amoretti, and E. Pavarini, "Many-body models for molecular nanomagnets," *Phys. Rev. Lett.* , vol. 110, p. 157204, Apr 2013.

[88] F. Troiani, V. Bellini, A. Candini, G. Lorusso, and M. Affronte, "Spin entanglement in supramolecular structures.," *Nanotechnology*, vol. 21, p. 274009, July 2010.

[89] V. Corradini, A. Ghirri, U. del Pennino, R. Biagi, V. A. Milway, G. Timco, F. Tuna, R. E. P. Winpenny, and M. Affronte, "Grafting molecular Cr_7Ni rings on a gold surface," *Dalton Trans.*, vol. 39, pp. 4928–4936, 2010.

[90] A. Ghirri, V. Corradini, C. Cervetti, A. Candini, U. del Pennino, G. Timco, R. J. Pritchard, C. A. Muryn, R. E. P. Winpenny, and M. Affronte, "Deposition of functionalized Cr_7Ni molecular rings on graphite from the liquid phase," *Adv. Funct. Mater.*, vol. 20, no. 10, pp. 1552–1560, 2010.

[91] V. Corradini, R. Biagi, U. del Pennino, V. De Renzi, A. Gambardella, M. Affronte, C. A. Muryn, G. A. Timco, and R. E. P. Winpenny, "Isolated heterometallic Cr_7Ni rings grafted on Au(111) surface," *Inorg. Chem.*, vol. 46, no. 12, pp. 4937–4943, 2007, http://pubs.acs.org/doi/pdf/10.1021/ic0624266.

[92] J. van Slageren, R. Sessoli, D. Gatteschi, A. A. Smith, M. Helliwell, R. E. P. Winpenny, A. Cornia, A.-L. Barra, A. G. M. Jansen, E. Rentschler, and G. A. Timco, "Magnetic anisotropy of the antiferromagnetic ring $[Cr_8F_8Piv_{16}]$," *Chem. Eur. J.*, vol. 8, no. 1, pp. 277–285, 2002.

[93] S. Carretta, P. Santini, G. Amoretti, M. Affronte, A. Ghirri, I. Sheikin, S. Piligkos, G. Timco, and R. E. P. Winpenny, "Topology and spin dynamics in magnetic molecules," *Phys. Rev. B*, vol. 72, p. 060403, Aug 2005.

[94] S. Carretta, P. Santini, G. Amoretti, T. Guidi, J. R. D. Copley, Y. Qiu, R. Caciuffo, G. Timco, and R. E. P. Winpenny, "Quantum oscillations of the total spin in a heterometallic antiferromagnetic ring: Evidence from neutron spectroscopy," *Phys. Rev. Lett.* , vol. 98, p. 167401, Apr 2007.

[95] J. Lee, *Concise Inorganic Chemistry, 5th ed.* Wiley India Pvt. Limited, 2008.

[96] V. Bellini, A. Olivieri, and F. Manghi, "Density-functional study of the Cr_8 antiferromagnetic ring," *Phys. Rev. B*, vol. 73, p. 184431, May 2006.

[97] F. Troiani, A. Ghirri, M. Affronte, S. Carretta, P. Santini, G. Amoretti, S. Piligkos, G. Timco, and R. E. P. Winpenny, "Molecular engineering of antiferromagnetic rings for quantum computation," *Phys. Rev. Lett.* , vol. 94, p. 207208, May 2005.

[98] W. Wernsdorfer, D. Mailly, G. A. Timco, and R. E. P. Winpenny, "Resonant photon absorption and hole burning in Cr_7Ni antiferromagnetic rings," *Phys. Rev. B*, vol. 72, p. 060409, Aug 2005.

[99] D. E. Richardson and H. Taube, "Electronic interactions in mixed-valence molecules as mediated by organic bridging groups," *J. Am. Chem. Soc.*, vol. 105, no. 1, pp. 40–51, 1983.

[100] V. Marvaud, J.-P. Launay, and C. Joachim, "Electron transfer through 2,7,9,10-tetraazaphenanthrene: a quantum "interference" effect?," *Chem. Phys.*, vol. 177, no. 1, pp. 23–30, 1993.

[101] A. D. Becke, "Density-functional thermochemistry. III. the role of exact exchange," *J. Chem. Phys.* , vol. 98, no. 7, pp. 5648–5652, 1993.

[102] L. Engelhardt, C. Muryn, R. Pritchard, G. Timco, F. Tuna, and R. Winpenny, "Octa-, deca-, trideca-, and tetradecanuclear heterometallic cyclic chromiumcopper cages,"

Angew. Chem. Int. Ed., vol. 47, no. 5, pp. 924–927, 2008.

[103] G. Lorusso, *Quantum effects in molecular spin clusters*. PhD thesis, Nano PhD School - University of Modena and Reggio-Emilia, 2011.

[104] D. Gatteschi, R. Sessoli, and J. Villain, *Molecular Nanomagnets*. Mesoscopic Physics and Nanotechnology, OUP Oxford, 2006.

[105] A. Bencini, D. Gatteschi, F. Totti, D. N. Sanz, , and M. D. Ward, "Density Functional Modeling of Long Range Magnetic Interactions in Binuclear Oxomolybdenum(V) Complexes," *J. Phys. Chem. A*, vol. 102, no. 51, pp. 10545–10551, 1998, http://pubs.acs.org/doi/pdf/10.1021/jp973328w.

[106] E. Gopal, *Specific heats at low temperatures*. International cryogenics monograph series, Plenum Press, 1966.

[107] M. Mannini, F. Pineider, P. Sainctavit, C. Danieli, E. Otero, C. Sciancalepore, A. M. Talarico, M.-A. Arrio, A. Cornia, D. Gatteschi, and R. Sessoli, "Magnetic memory of a single-molecule quantum magnet wired to a gold surface," *Nat. Mater.*, vol. 8, p. 194, 2009.

[108] S. Kahle, Z. Deng, N. Malinowski, C. Tonnoir, A. Forment-Aliaga, N. Thontasen, G. Rinke, D. Le, V. Turkowski, T. S. Rahman, S. Rauschenbach, M. Ternes, and K. Kern, "The quantum magnetism of individual manganese-12-acetate molecular magnets anchored at surfaces," *Nano Lett.*, vol. 12, no. 1, p. 518, 2012.

[109] S. Javaid, M. Bowen, S. Boukari, L. Joly, J.-B. Beaufrand, X. Chen, Y. J. Dappe, F. Scheurer, J.-P. Kappler, J. Arabski, W. Wulfhekel, M. Alouani, and E. Beaurepaire, "Impact on interface spin polarization of molecular bonding to metallic surfaces," *Phys. Rev. Lett.*, vol. 105, p. 077201, 2010.

[110] C. Wäckerlin, D. Chylarecka, A. Kleibert, K. Müller, C. Iacovita, F. Nolting, T. A. Jung, and N. Ballav, "Controlling spins in adsorbed molecules by a chemical switch," *Nat. Commun.*, vol. 1, p. 61, 2010.

[111] A. Lodi Rizzini, C. Krull, T. Balashov, J. J. Kavich, A. Mugarza, P. S. Miedema, P. K. Thakur, V. Sessi, S. Klyatskaya, M. Ruben, S. Stepanow, and P. Gambardella, "Coupling single molecule magnets to ferromagnetic substrates," *Phys. Rev. Lett.*, vol. 107, p. 177205, 2011.

[112] J. Brede, N. Atodiresei, S. Kuck, P. Lazić, V. Caciuc, Y. Morikawa, G. Hoffmann, S. Blügel, and R. Wiesendanger, "Spin- and energy-dependent tunneling through a single molecule with intramolecular spatial resolution," *Phys. Rev. Lett.* , vol. 105, p. 047204, Jul 2010.

[113] J. Repp, G. Meyer, S. M. Stojković, A. Gourdon, and C. Joachim, "Molecules on insulating films: Scanning-tunneling microscopy imaging of individual molecular orbitals," *Phys. Rev. Lett.* , vol. 94, no. 2, p. 026803, 2005.

[114] J. Mao, H. Zhang, Y. Jiang, Y. Pan, M. Gao, W. Xiao, and H.-J. Gao, "Tunability of supramolecular kagome lattices of magnetic phthalocyanines using graphene-based moiré patterns as templates," *J. Am. Chem. Soc.*, vol. 131, no. 40, p. 14136, 2009.

[115] M. Scardamaglia, S. Lisi, S. Lizzit, A. Baraldi, R. Larciprete, C. Mariani, and M. G. Betti, "Graphene-induced substrate decoupling and ideal doping of a self-assembled iron-phthalocyanine single layer," *J. Phys. Chem. C*, vol. 117, no. 6, p. 3019, 2013.

[116] W. Dou, S. Huang, R. Q. Zhang, and C. S. Lee, "Molecule–substrate interaction channels of metal-phthalocyanines on graphene on Ni(111) surface," *J. Chem. Phys.* , vol. 134, no. 9, p. 094705, 2011.

[117] J. Uihlein, H. Peisert, M. Glaser, M. Polek, H. Adler, F. Petraki, R. Ovsyannikov, M. Bauer, and T. Chassé, "Communication: Influence of graphene interlayers on the interaction between cobalt phthalocyanine and Ni(111).," *J. Chem. Phys.* , vol. 138, no. 8, p. 081101, 2013.

[118] A. Candini, S. Klyatskaya, M. Ruben, W. Wernsdorfer, and M. Affronte, "Graphene spintronic devices with molecular nanomagnets," *Nano Lett.*, vol. 11, no. 7, p. 2634, 2011.

[119] S. M. Avdoshenko, I. N. Ioffe, G. Cuniberti, L. Dunsch, and A. A. Popov, "Organometallic complexes of graphene: Toward atomic spintronics using a graphene web," *ACS Nano*, vol. 5, no. 12, p. 9939, 2011.

[120] J. Maassen, W. Ji, and H. Guo, "Graphene spintronics: the role of ferromagnetic electrodes," *Nano Lett.*, vol. 11, no. 1, pp. 151–155, 2010.

[121] Y. Li, X. Chen, G. Zhou, W. Duan, Y. Kim, M. Kim, and J. Ihm, "Trends in charge transfer and spin alignment of metallocene on graphene," *Phys. Rev. B*, vol. 83,

p. 195443, May 2011.

[122] L. V. Dzemiantsova, M. Karolak, F. Lofink, A. Kubetzka, B. Sachs, K. von Bergmann, S. Hankemeier, T. O. Wehling, R. Frömter, H. P. Oepen, A. I. Lichtenstein, and R. Wiesendanger, "Multiscale magnetic study of Ni(111) and graphene on Ni(111)," *Phys. Rev. B*, vol. 84, p. 205431, 2011.

[123] E. N. Voloshina, Y. S. Dedkov, S. Torbrügge, A. Thissen, and M. Fonin, "Graphene on Rh(111): Scanning tunneling and atomic force microscopies studies," *Appl. Physics Lett.*, vol. 100, no. 24, p. 241606, 2012.

[124] D. Pacilé, P. Leicht, M. Papagno, P. M. Sheverdyaeva, P. Moras, C. Carbone, K. Krausert, L. Zielke, M. Fonin, Y. S. Dedkov, F. Mittendorfer, J. Doppler, A. Garhofer, and J. Redinger, "Artificially lattice-mismatched graphene/metal interface: Graphene/Ni/Ir(111)," *Phys. Rev. B*, vol. 87, p. 035420, 2013.

[125] R. Decker, J. Brede, N. Atodiresei, V. Caciuc, S. Blügel, and R. Wiesendanger, "Atomic-scale magnetism of cobalt-intercalated graphene," *Phys. Rev. B*, vol. 87, p. 041403, 2013.

[126] Weser, M. and Voloshina, E. N. and Horn, K. and Dedkov, Yu. S., "Electronic structure and magnetic properties of the graphene/Fe/Ni(111) intercalation-like system," *Phys. Chem. Chem. Phys.*, vol. 13, p. 7534, 2011.

[127] M. Vanin, J. J. Mortensen, A. K. Kelkkanen, J. M. Garcia-Lastra, K. S. Thygesen, and K. W. Jacobsen, "Graphene on metals: A van der waals density functional study," *Phys. Rev. B*, vol. 81, no. 8, p. 081408, 2010.

[128] F. Ortmann, F. Bechstedt, and W. G. Schmidt, "Semiempirical van der waals correction to the density functional description of solids and molecular structures," *Phys. Rev. B*, vol. 73, p. 205101, May 2006.

[129] G. Henkelman, A. Arnaldsson, and H. Jónsson, "A fast and robust algorithm for bader decomposition of charge density," *Comp. Mater. Science*, vol. 36, no. 3, p. 354, 2006.

[130] B. W. Heinrich, L. Limot, M. V. Rastei, C. Iacovita, J. P. Bucher, D. M. Djimbi, C. Massobrio, and M. Boero, "Dispersion and localization of electronic states at a ferrocene/Cu(111) interface," *Phys. Rev. Lett.* , vol. 107, no. 21, p. 216801, 2011.

[131] K.-F. Braun, V. Iancu, N. Pertaya, K.-H. Rieder, and S.-W. Hla, "Decompositional Incommensurate Growth of Ferrocene Molecules on a Au(111) Surface," *Phys. Rev. Lett.*, vol. 96, p. 246102, 2006.

[132] J. Choi and P. Dowben, "Cobaltocene adsorption and dissociation on Cu(111)," *Surf. Sci.* , vol. 600, no. 15, p. 2997, 2006.

[133] M. Fuentes-Cabrera, M. I. Baskes, A. V. Melechko, and M. L. Simpson, "Bridge structure for the graphene/ni(111) system: A first principles study," *Phys. Rev. B*, vol. 77, p. 035405, 2008.

[134] L. Dagum and R. Menon, "OpenMP: an industry standard API for shared-memory programming," *Comput. Sci. Eng. Mag. IEEE*, vol. 5, no. 1, pp. 46–55, 1998.

[135] P. Giannozzi, S. Baroni, N. Bonini, M. Calandra, R. Car, C. Cavazzoni, D. Ceresoli, G. L. Chiarotti, M. Cococcioni, I. Dabo, A. Dal Corso, S. de Gironcoli, S. Fabris, G. Fratesi, R. Gebauer, U. Gerstmann, C. Gougoussis, A. Kokalj, M. Lazzeri, L. Martin-Samos, N. Marzari, F. Mauri, R. Mazzarello, S. Paolini, A. Pasquarello, L. Paulatto, C. Sbraccia, S. Scandolo, G. Sclauzero, A. P. Seitsonen, A. Smogunov, P. Umari, and R. M. Wentzcovitch, "QUANTUM ESPRESSO: a modular and open-source software project for quantum simulations of materials," *J. Phys. Condens. Mat.* , vol. 21, no. 39, p. 395502 (19pp), 2009.

[136] K. Momma and F. Izumi, "*VESTA*: a three-dimensional visualization system for electronic and structural analysis," *J. Appl. Cryst.* , vol. 41, p. 653, Jun 2008.

[137] J. D. Hunter, "Matplotlib: A 2d graphics environment," *Comput. Sci. Eng.*, vol. 9, no. 3, pp. 90–95, 2007.

Acknowledgements

I would like to express my gratitude to Prof. F. Manghi for the unique chance to devote myself to something I like so much as Nanotechnology. I thank her for the interesting topics proposed and her guidance as well as the freedom left me during the project to deepen my research interests.

A very special thanks goes out to Dr. V. Bellini, whose intelligence, sensibility, and patience, enriched constantly my former experience. I appreciate his vast knowledge as well as his vision and ethics skills. His confidence in my potentials and his assistance in writing reports (i. e. grant proposal, scholarship, applications, and above all this thesis) were key to the success of this work.

My gratitude goes to Prof. S. Heinze and Dr. P. Ferriani for the work spent together in Kiel, not to mention their warm welcome and friendship. I thank all the members of the great Spintronics Theory Group and in particular Dr. N. M. Caffrey and Dr. B. Dupé (note the accent!) because they made me feel like home also if I was thousands of kilometers away.

Herewith I would like to thank Prof. M. Affronte and Dr. G. Lorusso for the fruitful discussions and their support in my research.

I would like to thank all the persons in the Department of Physics here in Modena with whom I have had the opportunity to interact in these years. In random order, Prof. G. Santoro for the expert hints on Quantum Espresso, my former room mates Dr. M. Govoni and Dr. M. Bertocchi for their friendship, Dr. G. Arnaud for the friendly dinners followed by table games sessions, my funny Hispanic comrades Dr. M. Royo and Dr. C. Cardoso.

I thank also my friends in Rome and spread all around the world, among them, A. Pacini, M. Passariello, A. Lombardi, G. Ottaviani, R. Rosati, D. D'Armiento, E. Chi-

averini, S.Valente, A. Ponzi, M. Chiricotto for all their unconditional support and fraternal friendship.

My special regards goes also to my actual flatmates B. Saad Mohammadi and E. Mafakheri for the kind and relaxing atmosphere in home during the draft of this thesis as well as for their friendship.

My very best thanks go to my parents, my brother and my relatives, which with their lovely supports constantly helped me during these years. Last but not least, I thank my mate Francesca because her love, optimism and encouragement push me to become always a better version of myself.

I apologize for people who are not mentioned even though they should be.

Simone Marocchi

Modena, 15 January 2014

List of Figures

List of Tables

Colophon

This thesis was made in LaTeX 2_ε using the "hepthesis" class. The plots were made with the VESTA software [136] and with python using the matplotlib package [137].

Declaration

I herewith declare that I have produced this paper without the prohibited assistance of third parties and without making use of aids other than those specified; notions taken over directly or indirectly from other sources have been identified as such. This paper has not previously been presented in identical or similar form to any other Italian or foreign examination board. The thesis work was conducted from 2011 to 2014 under the supervision of Dr. Valerio Bellini and Prof. Franca Manghi at the Physics Department of the University of Modena and Reggio Emilia.

Modena, 15 January 2014

Simone Marocchi